Dpto. de Física Teórica y del Cosmos & CAFPE
Universidad de Granada

Liquid Argon Detectors for Rare Event Searches

Memoria presentada por

Antonio Jesús Melgarejo Fernández.

Directores:

Dr. **Antonio Bueno Villar** y
Dr. **Sergio Navas Concha.**

- Mayo de 2008 -

D. Antonio Bueno Villar, Profesor Titular de Universidad, y D. Sergio Navas Concha, Profesor Contratado Doctor,

CERTIFICAN: que la presente memoria, LIQUID ARGON DETECTORS FOR RARE EVENT SEARCHES, ha sido realizada por D. Antonio Jesús Melgarejo Fernández bajo su dirección en el Dpto. de Física Teórica y del Cosmos, así como que éste ha disfrutado de estancias en el extranjero por un periodo superior a tres meses en el CERN (Suiza).

Granada, 2 de Mayo de 2008

Fdo: Antonio Bueno Villar Sergio Navas Concha

Agradecimientos

Juntar en tan solo unas páginas a toda la gente que, de uno u otro modo, tiene culpa de esta tesis, es sin duda una tarea imposible. Así pues, antes de nada, me gustaría pedir disculpas a todos los que no figuran aquí. Os lo agradezco mucho y que nadie piense que me olvido de ellos.

Tengo que agradecer, en primer lugar, a mis tutores, Antonio Bueno y Sergio Navas, por la gran labor que han llevado a cabo en estos años. Antonio, primero como mi profesor, fue la persona que me mostró el apasionante (para mi) campo de la Física de Partículas. Todo lo que he aprendido de él en estos años tiene un valor incalculable, y afortunadamente no todo se limita a la física. Sergio me ha enseñado lo divertido que puede ser perderse entre cables y tornillos, cosa que tiene mérito con alguien a quien su padre no dejaba usar el taladro, por si acaso. Además, con él he aprendido lo importante que es ser sistemático en la investigación. Con ambos he pasado grandes momentos y de corazón os digo que podría escribir otras 150 páginas más sólo para mostraros mi agradecimiento.

Gracias también a todos los miembros del grupo de física teórica de la Universidad de Granada, en particular a todos aquellos que han tenido que soportarme más estrechamente en estos años. Gracias a Paco del Águila, director del departamento, por haberme ofrecido la posibilidad de desarrollar mi trabajo en el mismo. Muchas gracias a Alberto, que ha sido el primero en dejarnos y con el que he vivido grandes momentos. A Mari Carmen, que me ha tenido en frente varios años, teniendo que sufrir cada tontería que se me ha ido ocurriendo. A Diego, del que he aprendido muchísimo, y que sin duda se ha convertido en un gran amigo. Y por supuesto a Luis, que ya era un gran amigo antes de ser mi compañero de penurias y lo ha seguido siendo a pesar de todo. Espero que la física sea igual de divertida sin vosotros. No quiero olvidar a Nacho, Jorge y Jose Luis, con los que también he compartido encierro. Y a Julio, que está un poco a caballo entre la figura de jefe y la de amigo, sin duda también tengo que agradecer todos los buenos ratos que me ha brindado y las múltiples risas. Gracias también a Ángel, con quien he compartido muchas horas de laboratorio y que me ha ayudado muchísimo con toda la electrónica.

Just a few words in english for the foreign thanks. I would like to thank to professors Andre Rubbia and Christian Regenfus for allowing me to work with them for the ArDM experiment, and to everybody in the experiment, specially to Vittorio Boccone for his help and support. I would also like to thank people from the CAST experiment, for helping me discover such an interesting world. And, of course, thanks to my good friend Pedja, who is somehow responsible that I'm writing this thesis today, and to the people at CERN who made staying there an incredible experience.

También quisiera dar las gracias a mi familia, sin los cuales nunca hubiera llegado hasta aquí. Gracias a mis padres, por haberme llevado todos estos años de la mano. A mi hermano, que ha estado siempre en lo mejor y en lo peor. Vosotros tres sois los que cada día cuando me acuesto y me levanto habéis estado a mi lado. A mis tíos Carmelo, Antonio, Tere, Fabi y a mi tata Ramona, quienes han estado ahí casi como unos segundos padres para mi. Y a todos mis primos, que al vivir tan cerca han tenido que soportarme como uno más. Gracias a todos mis amigos de Granada, me

habéis ayudado mucho estos años, y gracias a Cris y a la gente de Canarias, que supusieron un gran apoyo para poder acabar.

Gracias por último a ARPANET y al CERN por el invento de internet y la World Wide Web respectivamente. En cierto modo han hecho que mi tesis se retrase algunos meses, aunque sobrevivir a las interminables horas delante del ordenador ha sido mucho más fácil gracias a éstos. Mi agradecimiento especial es para www.yonkis.com, www.elmundo.es, www.cadenaser.com, www.youtube.com y foros.acb.com.

Contents

Introduction

The Standard Model of particle physics is the result of an immense experimental and inspired theoretical effort. The amount of supporting data is vast, and in particular, measurements done at LEP have confirmed this theory with precisions never reached before in our field. Notwithstanding its tremendous success, we are firmly convinced this theory is not the ultimate one. The evidence for the existence of new unexplained physics is growing. As an example let's us mention the paramount data accumulated by neutrino experiments, clearly showing that these particles cannot be considered massless. Cosmological measurements show how the majority of the Universe is composed by a new form of energy and matter not contemplated within the Standard Model. To settle those and other open questions the need for new theories and experiments is indisputable.

To unveil the mysteries of this yet unexplored physics realms, next generation experiments must make use of new technologies able to offer much better background rejection capabilities, more accurate determination of energy and momentum and improved particle identification capabilities. The liquid argon time projection chamber (LAr TPC) technology ranks among the most promising new detection techniques, most notably for the field of non-accelerator physics. Proposed in 1977 by Carlo Rubbia, they constitute a new generation of electronic bubble chambers able to provide excellent three-dimensional imaging capabilities and a fine granularity (see figure). The ICARUS collaboration has pursued over the last years a long R&D programme to address all the technological challenges associated to the operation of LAr TPCs of different sizes. The operation at surface of a 600 tonne detector has shown that this technique is now mature.

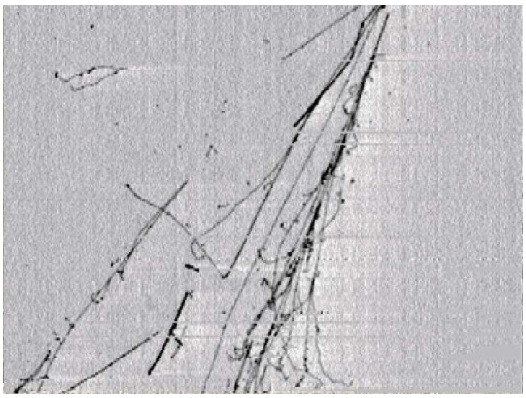

The work presented in this PhD Thesis discusses the potentialities of LAr TPCs when applied to the search for new, rare phenomena. We will try and show the versatility of these devices and their performance at very different energy scales. In particular, it is shown the relevance of the contributions LAr TPCs can make in two fields that lay nowadays at the fore-front of physics

research: the direct search for dark matter and the study of whether protons are unstable particles.

The Thesis is organized as follows: Chapter 1 reviews the most fundamental properties of liquid argon and the phenomena that take place in it when used as a detecting media. We pay particular attention to the devices that record the scintillation light produced after a particle scatters off an argon nucleus. More precisely, Chapter 2 shows a throughout and complete characterization of the performance of two types of photomultiplier tubes when operated at LAr temperatures. Reference [1] contains a detailed description of the main results obtained at our laboratory.

Chapter 3 fully concentrates on the subject of direct dark matter search from an experimental point of view. The main issue here deals with the possibility of building and operate a one tonne detector. This is the aim of the ArDM collaboration. We describe in detail the different milestones achieved during the assembly and first surface operation of the ArDM prototype.

Chapter 4 concentrates on the study of backgrounds associated to direct dark matter search experiments. It explores the physics performance of a modular detector operated in conjunction with an active veto target, made of water doped with gadolinium. Special attention is given to the identification and precise measurement of the background produced by neutrons (see reference [2] as well for details).

The last chapter of this Thesis is devoted to the study of a different kind of search: nucleon decay. This is a prediction of Grand Unified Theories that has not been observed so far. The hypothesized lifetimes, of the order of 10^{35} years, require the use of very massive instrumented volumes. We study the physics potential of a 100 kilo-tonne detector, paying special attention to the possibility of running a proton decay experiment at shallow depths. This work has given rise to the articles in references [3, 4].

Introducción

El Modelo Estándar de la Física de Partículas es el resultado de un enorme esfuerzo experimental y teórico. Hay una vasta cantidad de datos que lo respaldan y, en particular, las medidas realizadas en LEP han confirmado esta teoría con precisiones nunca antes alcanzadas en este campo. A pesar de su tremendo éxito, estamos convencidos de que esta teoría no es la definitiva. La evidencia de la existencia de nuevos fenómenos físicos que no podemos explicar crece con el tiempo. Como ejemplo podemos mencionar la cantidad de datos acumulados por los experimentos de neutrinos, que muestran claramente que no podemos seguir considerando a estas partículas como sin masa. Las medidas cosmológicas muestran que la mayoría del universo está compuesto por nuevas formas de materia y energía que no forman parte del Modelo Estándar. Para estudiar éstas y otras cuestiones abiertas, se necesitan de manera incuestionable nuevas teorías y experimentos.

Para desvelar los misterios de estos dominios de la física aún inexplorados, la próxima generación de experimentos debe hacer uso de las nuevas tecnologías, capaces de ofrecer capacidades de discriminación de fondos mucho mejores, determinación de energía y momento más precisa y capacidad para la identificación de partículas mejorada. La tecnología de la Cámara de Proyección Temporal de Argón Líquido (LAr TPC, por sus siglas en inglés) es una de las más prometedoras técnicas de detección, de forma más notable en el campo de la física sin aceleradores. Propuesta en 1977 por Carlo Rubbia, constituye una nueva generación de cámaras de burbujas electrónicas capaz de ofrecer una excelente capacidad para lograr imágenes en tres dimensiones y una fina granularidad (ver figura). La colaboración ICARUS ha llevado a cabo durante los últimos años un extenso programa de I+D para estudiar todos los desafíos tecnológicos asociados a la operación de LAr TPCs de diferentes tamaños. Mediante la puesta en funcionamiento en la superficie de un detector de 600 toneladas han demostrado que la técnica ha alcanzado ya su madurez.

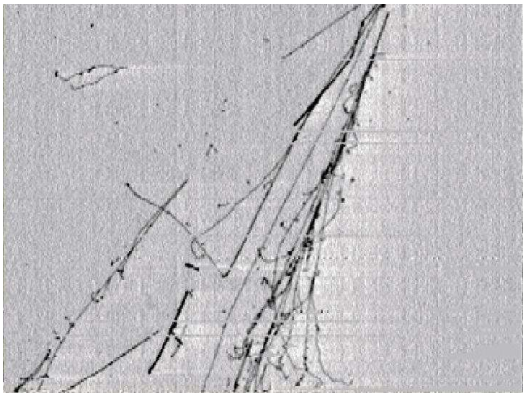

El trabajo que se presenta en esta Tesis trata las potencialidades de las LAr TPCs aplicadas a la búsqueda de nuevos fenómenos "extraños". Mostraremos la versatilidad de estos dispositivos y su rendimiento en escalas de energías muy diferentes. En particular, vamos a mostrar la relevancia de las contribuciones que las LAr TPCs pueden llevar a cabo en dos campos que hoy en día se encuentran a la vanguardia de la investigación en física: la búsqueda directa de materia oscura y el estudio de la inestabilidad de los protones.

Esta Tesis está organizada del siguiente modo: En el Capítulo 1 revisamos las propiedades más fundamentales del argón líquido y los fenómenos que tienen lugar en él cuando se usa como medio para un detector. Prestamos especial atención a los dispositivos que miden la luz de centelleo que se produce después de una colisión de una partícula con un núcleo de argón. En concreto, en el Capítulo 2 mostramos el proceso completo de una caracterización del rendimiento de dos tipos de fotomultiplicadores cuando los operamos a temperatura de argón líquido. La referencia [1] contiene una descripción detallada de los principales resultados obtenidos en nuestro laboratorio.

El Capítulo 3 se concentra completamente en la búsqueda directa de materia oscura desde un punto de vista experimental. Aquí la principal cuestión está relacionada con la posibilidad de construir y operar un detector de una tonelada. Éste es el objetivo de la colaboración ArDM. Describimos en detalle los diferentes hitos conseguidos durante el montaje y la primera operación en superficie del prototipo del detector ArDM.

El Capítulo 4 se concentra en el estudio de los fondos asociados a las búsquedas directas de materia oscura. En él se exploran las prestaciones de un detector modular que funciona al mismo tiempo que un blanco que actúa como veto activo, compuesto de agua dopada con gadolinio. Prestamos especial atención a la identificación y medida precisa del fondo generado por neutrones (ver también la referencia [2] para más detalles).

El último capítulo de esta Tesis está dedicado al estudio de un tipo de búsqueda diferente: la desintegración de nucleones. Ésta es una predicción de las Teorías de Gran Unificación que aún no ha sido observada. Las vidas medias predichas, del orden de 10^{35} años requieren volúmenes instrumentados muy masivos. Estudiaremos el potencial físico de un detector de $\sim$100 kilotoneladas de argón líquido, fijándonos especialmente en la posibilidad de llevar a cabo un experimento de este tipo a profundidades superficiales. Este trabajo ha conducido a la publicación de los artículos de las referencias [3, 4].

Chapter 1

Liquid Argon Detectors: Basic Principles

This chapter summarizes the fundamentals of the liquid argon TPC detection technology. This includes a discussion of both production and readout of charge and light (which is treated with much more detail in chapter 2). The last part of this introductory chapter is devoted to technical considerations such as argon purification and slow control devices (which include levelmeters, purity monitors and temperature sensors).

1.1 Liquid argon as target medium for a detector

The introduction of electronics in particle physics supposed a major improvement in the way data were recorded and analyzed. Gaseous ionization detectors were the first electronic devices used. Although in the beginning these were quite simple, e.g. the Geiger-Müller counter, the development in the late 1960's of multiwire proportional counters, with capability to locate particle trajectories with precision of less than 1 mm, made them widely adopted. With time, the increasing requirements in the field led to the need of using liquids instead of gases as the ionization media, which allowed for more massive detectors, due to their much bigger densities and lower diffusion. Compared to gases, liquids present a big technical issue: purity. The presence of small quantities ($\sim$1 ppm[1]) of electronegative impurities such as O_2 can drastically decrease the detected signal amplitude. This reduces the choice of media to a few hydrocarbons and noble elements.

Among all the candidates, liquid argon presents some very interesting characteristics, which made it one of the most extended target medium for ionization detectors. Table 1.1 shows a summary of the main chemical and physical properties of liquid argon. The high density and low diffusion permit to have an efficient target for weakly interacting particles in a relatively small volume and a high precision in the determination of positions, which makes liquid argon a great target for the potential discovery of rare phenomena.

Thanks to its properties, liquid argon is a good medium to detect energetic events. LAr has a radiation length of 14 cm and a nuclear interaction length of 83.6 cm, giving good electromagnetic and hadronic calorimetric capabilities. Liquid argon calorimeters are widely used in particle physics [5]. The high ionization density in the liquid gives enough electron–ion pairs per unit length to detect directly the ionization charge without any multiplication. Thus, the liquid has

[1] 1 ppm = 1 part per million

Atomic number	18
Concentration in air	0.934%
Naturally occurring isotopes	$^{36}Ar = 0.3365(30)\,\%$ stable $^{38}Ar = 0.0632(5)\,\%$ stable $^{40}Ar = 99.6006(30)\,\%$ stable
Melting point (101325 Pa)	83.8058 K(−189.3℃)
Boiling point (101325 Pa)	87.293 K(−185.8℃)
Density at boiling point (101325 Pa)	1.396 kg/ℓ liquid 5.79 g/ℓ gas
Liquid heat capacity at boiling point (101325 Pa)	1.078 kJ/kg/K liquid
Latent energy of fusion at boiling point (101325 Pa)	161.0 kJ/kg liquid
dE/dx_{min} for a mip	2.12 MeV/cm
Critical energy (electrons)	31.7 MeV
Mean excitation potential	210 eV
Energy to produce an electron-ion pair	23.6 eV
Radiation length X_0	14.0 cm
Molière radius	9.28 cm
Nuclear interaction length	84.0 cm
Maximal breakdown strength (depending on purity level)	$1.1 - 1.4\,MV$/cm
e^- Diffusion coefficient (89 K)	4.8 cm^2/s
Recombination factor for mips (μ)	0.6 at 0.5 kV/cm

Table 1.1: Physical and chemical properties of argon.

the advantage to give a high-resolution spatial tracking information and, at the same time, acting as a continuous hadronic and electromagnetic calorimeter. Even in the case of non-fully contained events, the good imaging precision obtained in liquid argon may provide calorimetric information on the particles, through the multiple scattering information [4]. The good granularity for calorimetry can also be used for particle identification through the measurement of dE/dx versus range. Proton decay searches and neutrino physics can profit from liquid argon detector performances.

Even for low energy events, liquid argon is an excellent target medium. It is possible to use charge amplifying devices, such as LEMs or GEMs [6] for charge readout. In addition, liquid argon acts as a great scintillator, with light yields comparable to those of crystals like NaI. This scintillation light provides an extra information for energetic reconstruction which, together with charge, allows for particle identification at low energies. Thus, liquid argon can be used to measure low energy events, as in dark matter searches, with good positioning, calorimetric reconstruction and excellent background rejection capabilities.

The above arguments, together with the low cost compared to xenon, for instance, makes LAr a great choice as target for the search of rare phenomena and neutrino physics.

1.2 Interactions in liquid argon

The principle of a LAr TPC is simple: a charged particle traversing a liquid argon volume will generate free electrons (e^-), argon ions (Ar^+) and excited atoms (Ar^*). If an electric field is applied the electrons will drift towards the lowest potential where they can be read by an appropriate device.

This is technically easy due to the high breakdown voltage of liquid argon (see table 1.1), which

allows to set high voltages with electric fields typically of the order of ∼kV/cm. Also one can set arrays of tight electrodes, which make electric fields uniform. In this case the electrons will drift towards the anode with a drift velocity that will depend on the electric field and in a smaller grade on the liquid argon temperature [7, 8, 9].

Electrons can, on the other hand, recombine with their parents nuclei before they can get apart due to the action of the external electric field. This will produce excited argon atoms which will add up to those produced by the parent ionizing particle. This excited atoms will, in general, decay to photons in the energetic range of the vacuum ultraviolet, with a wavelength of 128 nm.

1.2.1 Scintillation light in Liquid Argon

Scintillation light emission in LAr has been investigated in great detail by many authors since the pioneering studies of Doke *et al.* [10]. Light is of major importance because there are production mechanisms with typical times of few ns, which make photons useful to provide the interaction time and the trigger for the events. Moreover, light is also related to the energy of the interacting particles, and hence it can provide calorimetric information.

In the ionization process from charged particles [11], the average energy to produce an electron-ion pair in LAr is $W_{ion} = 23.6$ eV [12]. Ions Ar^+ and excited atoms Ar^*, in the ratio $N_*/N_+ = 0.21$ lead to Ar_2^* excited dimer formation (namely the singlet $^1\Sigma_u^+$ and the triplet $^3\Sigma_u^+$ states in the M-band).

Scintillation photons are produced basically by the following processes [13]:

- by the direct excitation of an argon atom followed by an excited molecule formation and de-excitation:
$$\mathrm{Ar}^* + \mathrm{Ar} \rightarrow \mathrm{Ar}_2^* \rightarrow 2\,\mathrm{Ar} + \gamma(128\ \mathrm{nm}) \tag{1.1}$$
- by the formation of a molecular state through recombination processes between electrons and molecular ions:
$$\mathrm{Ar}^+ + \mathrm{Ar} \rightarrow \mathrm{Ar}_2^+ + e^- \rightarrow \mathrm{Ar}_2^* \rightarrow 2\,\mathrm{Ar} + \gamma(128\ \mathrm{nm}) \tag{1.2}$$

As already mentioned, the γ emission spectrum is in the vacuum ultraviolet (VUV) region, peaking around $\lambda = 128$ nm (FWHM$\simeq$ 6 nm) (see figure 1.1), corresponding to the Ar_2^* M-band level of 9.8 eV with respect to the ground dissociative level [14].

The average energy for a scintillation photon emission is $W_{ph} = W_{ion}/(1 + N_*/N_+) = 19.5$ eV (uncertainty less than 10%) [15], corresponding to an "ideal" photon yield of 5.1×10^4 γ/MeV. This figure is confirmed by more recent investigations, measuring yields of 5.5×10^4 γ/MeV [14].

The referred to processes are affected by the presence of electric fields. Fast recombination along the ionization track plays an important role and when an electric field is applied to the LAr medium the increase of the field strength results in a reduction on scintillation, balanced by an increase of free electron charge. At high fields (e.g. > 10 kV/cm), the free electron yield saturates and the scintillation intensity reaches a flat minimum (the field-independent contribution from decay of dimers formed by Ar^* excited atoms - the "self-trapped excitons"), about 33% of the total light emitted at zero field [16].

The relative amounts of charge and light clearly depend also on the type of particle and its linear energy transfer (LET, the specific energy loss along the path). For a minimum ionizing particle (low LET value, ~ 2 MeV cm^2/g), the photon yield at zero field has been measured and its value was found to be 4.0×10^4 γ/MeV, i.e. a factor 0.78 lower than the ideal case (obtained for heavy ions). This is interpreted as due to electron enhanced escape probability from geminate recombination for low dE/dx.

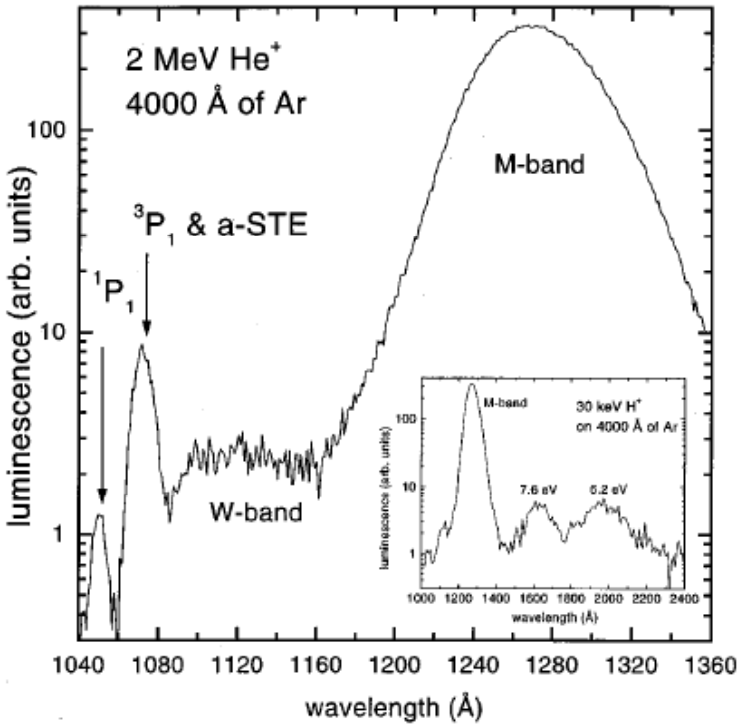

Figure 1.1: Argon emission spectrum reproduced from reference [14].

The time dependence of scintillation in LAr is also an important issue. It exhibits roughly a double exponential decay form, characterized by two different components: a fast component, with a time constant of $\tau_s = 6 \pm 2$ ns and a slow component, with a time constant of $\tau_t = 1600 \pm 100$ ns [17]. These are considered to represent the lifetimes of the singlet $^1\Sigma_u$ and of the triplet $^3\Sigma_u$ excited molecular states respectively. The time constant values do not depend appreciably on the ionizing density, i.e., the time constants measured for mips and for heavily ionizing particles agree within the experimental errors.

The LET value, however, strongly affects the intensity ratio I_s/I_t of the singlet and triplet states: at zero field the relative weights for the fast and for the slow component are $I_s = 23\%$ and $I_t = 77\%$ respectively ($I_s/I_t = 0.3$) in case of a mip, while for heavily ionizing particles the intensity ratio increases (e.g., $I_s/I_t = 1.3$ for α-particles) [17]. It is worth noting that this effect is directly contrary to the effect shown in organic scintillators, in which the relative intensity of the slow component increases with increasing specific ionization density. Regardless of this opposite behavior, the full separation between τ_s and τ_t in liquid argon, as for the organic scintillator case, makes possible to define Pulse Shape Discrimination criteria suitable for particle identification. Very high electric field values may also affect the intensity weights of the decay components, although for the typical values used in dark matter searches the intensity ratios reported above have been confirmed by the WARP collaboration [18].

Scintillation photons have energy lower than the first excited state of the Ar atom. Therefore pure LAr is transparent to its own scintillation radiation. The physical process of Rayleigh

scattering from density fluctuations [19] can be advocated to explain the observed attenuation of light signals observed in large volume detectors [13]. Absorption from photo-sensitive impurities diluted in LAr may provide an additional (unwanted) contribution of attenuation, depending on the level of purity of the liquid in use. A classical expression for the Rayleigh scattering length $l_R(\lambda; \epsilon_{Ar}, \rho_{Ar})$ is given in [20] (ϵ_{Ar} and ρ_{Ar} are the Ar dielectric constant and density). Difficulties in determining l_R in LAr arise in estimating the density dependence of the dielectric constant since appears to be no measurements of ϵ_{Ar} in liquid phase at the scintillation wavelength. Based on the measurements in gas phase, the dielectric constant in LAr has been calculated as a function of the wavelength and a Rayleigh scattering length of $l_R(128\text{ nm}) = 90\text{ cm}\pm35\%$ has been inferred [21]. The calculated attenuation length agrees with the experimentally measured value [13].

1.2.2 Calorimetry and particle identification

Charged particles traversing the LAr sensitive volume produce ionization electrons in a number proportional to the energy transferred to the LAr. The ionization electrons drift to the charge readout pushed by the electric field, inducing a signal which carries out information about the position of the event (trough the identification of the position in the readout device and the drift time) and information about the energy deposition in that position, which is proportional to the collected charge. Thus, the combined spatial and calorimetric reconstructions, exploiting the fine granularity and imaging capabilities of the detector, allows the precise measurement of the energy loss per crossed distance (dE/dx) and hence the identification of the ionizing particle.

The complete calorimetric reconstruction of the events requires to take into account the effects of the electron-ion recombination and charge attenuation by electron attachment to electronegative impurities. Both effects reduce the amount of collected charge with respect to the one produced during the ionization. The recombination of ion-electron pairs occurring immediately after the ionization due to their electrostatic attraction, forms excited atomic states that release the energy in the form of light. The magnitude of the recombination effect depends on both the electric field and the ionization density (dE/dx). Charge attenuation is due to the attachment of the drift electrons to the electronegative impurities, and depends also on the electric field and on the concentration of electronegative impurities present on the LAr volume. The precise knowledge of these two phenomena allows their off-line unfolding from the calorimetric data.

If the granularity of the read-out electrodes is high enough, a sampling of the energy loss per crossed distance (dE/dx) for several points along the ionization tracks is possible. If, on the other hand, the momentum of the particle is independently known, e.g. from its curvature in a magnetic field, or from its range (for particles stopping in the LAr sensitive volume only), or from multiple scattering, it is possible to determine the mass of the ionizing particle by means of the Bethe-Bloch formula which describes the energy loss per crossed distance (dE/dx), and hence identify the ionizing particle. The particle identification capability [22] is illustrated in Fig. 1.2, where the dE/dx vs. kinetic energy behaviour of stopping muons, kaons and protons are compared. A clear separation exists among the three particle species.

1.3 From bubble chambers to the liquid argon TPC

Bubble chamber detectors [23, 24] were of major importance during the initial years of the particle physics. Invented in 1952 by Donald Arthur Glaser, for what he was awarded with the Nobel Prize in 1960, these detectors led to the discovery of many new elementary particles from the second half of the decade of 1950 until around 1970. It was an evolution of the cloud chamber, used successfully since 1911. The working principle of a bubble chamber is bubble formation in a liquid

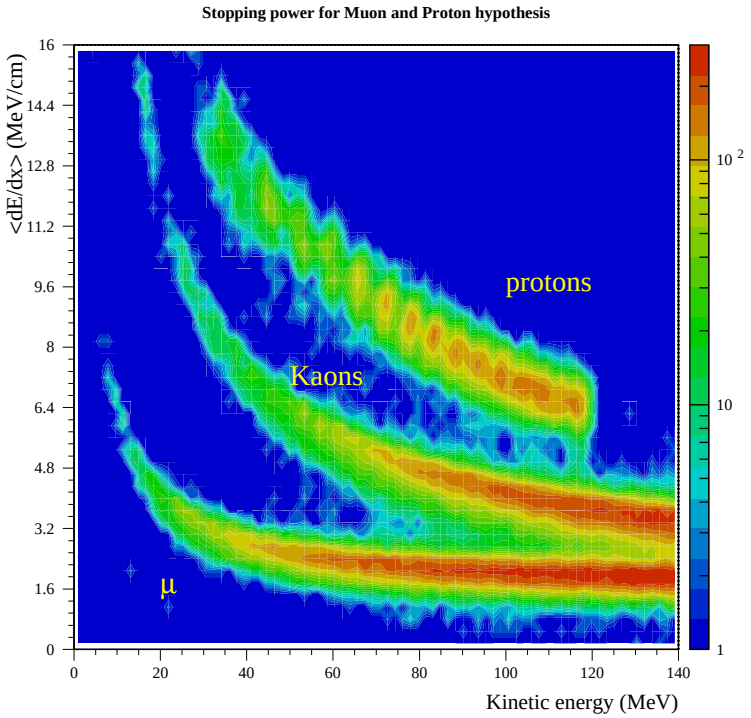

Figure 1.2: Scatter plot showing the regions populated by muons, kaons and protons on the $< dE/dx >$ vs. kinetic energy plane from fully simulated events on a liquid argon TPC.

heated above its boiling point, which is then suddenly expanded. Boiling starts wherever passing charged particles ionize the atoms of the liquid. Tracks can be then recorded by means of cameras, and the images can be analyzed in a later phase in order to obtain precise information about the recorded event. These chambers were often used together with magnetic fields that bent particles in order to obtain kinematic information about them.

1.3.1 The Time Projection Chamber

The Time Projection Chamber (TPC), invented by Dave Nygren at the Lawrence Berkeley Laboratory (LBL) in the late 1970s, is essentially a three dimensional tracking device, capable of providing imaging of an ionizing particle track and a measurement of its specific energy loss, dE/dx. It consists of a pair of parallel electrodes immersed in an ionization medium (a gas or a liquid) and connected to a high voltage power supply (see Fig. 1.3), producing an homogeneous electric field perpendicular to the electrodes.

A particle passing through the gas or the liquid will ionize the medium along the track and create ion–electron pairs . The applied electric field suppresses the immediate recombination of the pairs (important mainly in a liquid medium), pulling the electrons and ions apart. The ionization electrons produced by the particle will drift along the electric field lines to the anode, which is

composed of an array of position sensitive sensors.

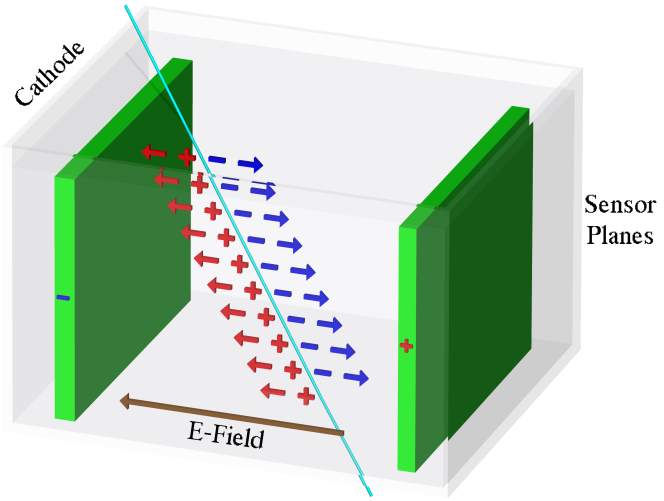

Figure 1.3: Schematic view of a TPC. A charged particle is passing through an ionization medium (e.g. LAr) and the electrons drift along the electric field lines to the sensors.

Imaging of events

The sensors located in the anode of the detector must consist of a set of charge read-out devices in which not only the value of the charge must be measured, but also the position in which the charge was produced.

One of the first solutions used was a set of planes of multiple parallel wires (hereafter called *wire planes*) (as shown in fig. 1.4) . We can obtain two-dimensional projections of the ionization point, constraining one spatial coordinate from the wire collecting the charge (or a current being induced) and the other from the drift time. In order to obtain three-dimensional coordinates, at least two wire planes with different wire orientations are necessary; therefore, the read-out system must be non-destructive.

The transparency of a wire plane or grid for electrons drifting along the electric field lines is a function of the ratio of the fields E_1 and E_2, in front and behind the grid respectively, and of the ratio $\rho = 2\pi r/p$ where r is the wire radius and p is the spacing between wires (*pitch*). Full transparency is reached when the following condition is satisfied [25]:

$$\frac{E_2}{E_1} > \frac{1+\rho}{1-\rho} \tag{1.3}$$

This condition has to be balanced against the requirement that the grid has to act as an electrostatic shielding between the space in front and behind it. If this condition is satisfied, a drifting charge will be sensed by the electrodes behind the grid only when the grid itself is crossed. Detailed calculations show that the shielding power, σ, of a grid is approximately given by the following formula [25]:

$$\sigma = \frac{p}{2\pi d} \ln\left(\frac{p}{2\pi r}\right) \tag{1.4}$$

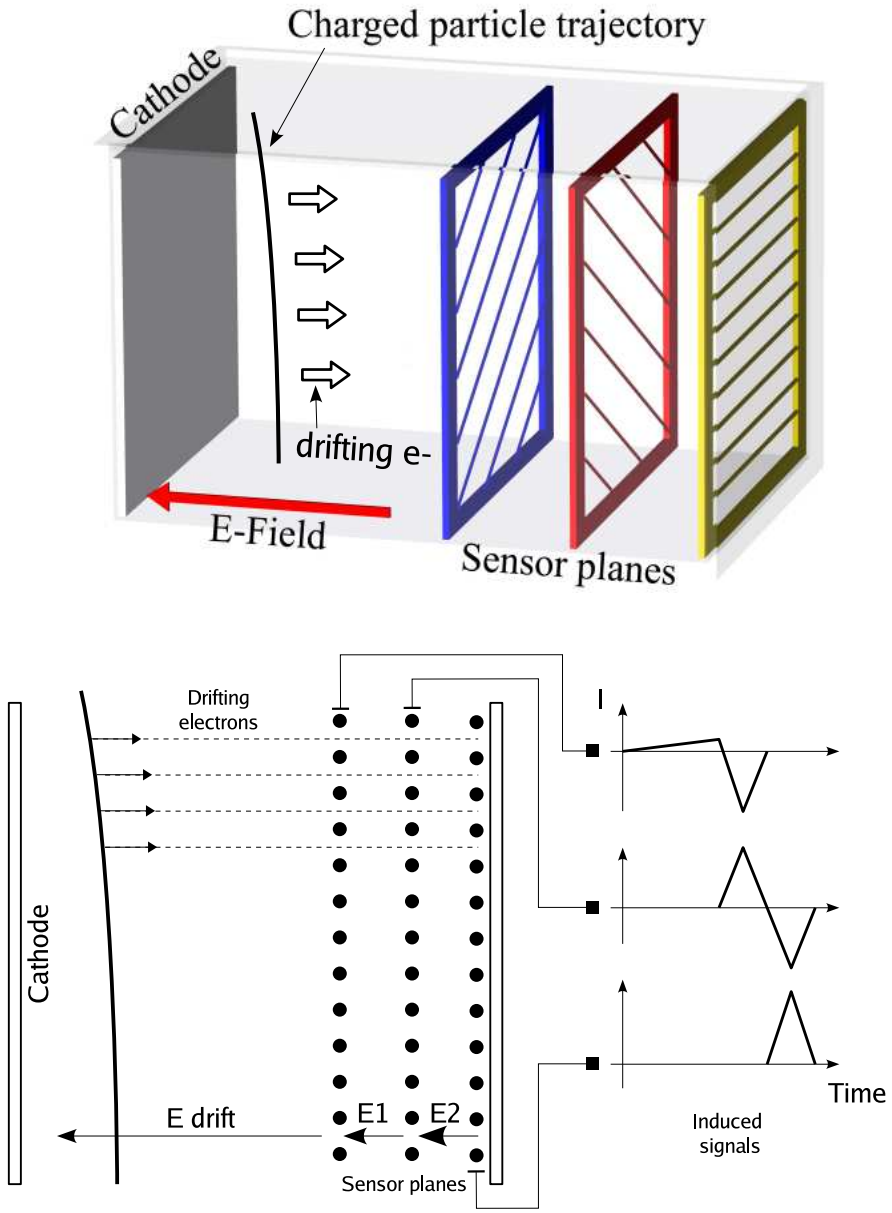

Figure 1.4: Schematic view of a LAr TPC with three sensing planes.

where d is the distance between the grid and the next electrode. Note that shielding factors deviating a few percent from one are acceptable.

While wires provide a good spatial resolution, charge is not amplified when read, which limits their application to high energy events. Recently, several devices have been proposed, and some of them have already been used in running experiments, that allow charge amplification while having

comparable spatial resolutions. Among them, we can point GEM (Gas Electron Multipliers) [6] and LEM (Large Electron Multiplier) [26] (which are similar devices that obtain charge multiplication by the application of high electric fields in the gas phase) and charge extracting meshes, in which a high electric field is applied to obtain a measurable light signal proportional to the extracted charge.

1.3.2 The liquid argon TPC

Although nowadays there are experiments that still work with bubble chambers, their use has been superseded by electronic detectors in recent times. The attempt to merge the superb imaging capabilities of traditional bubble chambers and the advantages of electronic read-out in a single detector led C. Rubbia to propose the liquid argon time projection chamber in 1977 [27]. The detector is essentially a cryostat filled with a liquefied noble gas with a high electric field. Whenever a particle traverses the detector, it ionizes atoms of the medium, which produces free electrons and light from de-excitation of recombined atoms. The electrons produced in these collisions are then drifted towards the lower electric potential side of the cryostat where they are collected. This technique provides three-dimensional imaging, as the coordinate parallel to the electric field can be known from the time that electrons take to drift, given the drift velocity is known. And, since the ionization charge is proportional to the energy deposition, also acts as a calorimeter of very fine granularity and high accuracy. Thus, this device is ideal to study particle interactions and does not present the problems of traditional bubble chambers, since the electronic read-out allows the self-triggering and automatic processing and analysis of the events.

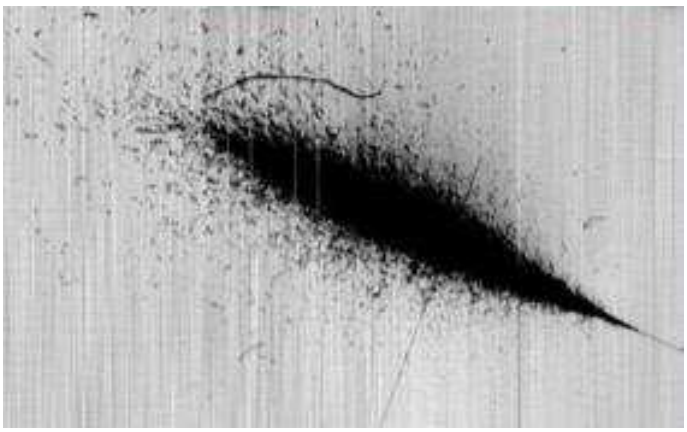

Figure 1.5: Real electromagnetic cascade recorded with the ICARUS T600 TPC.

After the original proposal, the feasibility of the technology has been demonstrated by an extensive R&D programme, which included 10 years of studies on small LAr volumes (proof of principle, LAr purification methods, read-out schemes, electronics) and 5 years of studies with several prototypes of increasing mass (purification technology, collection of physics events, pattern recognition, long duration tests, read-out technology). The largest of these devices had a mass of 3 tons of LAr [28], and has been operated continuously for more than 4 years, collecting a large sample of cosmic-ray and γ-source events. Furthermore, a smaller device (50 l of LAr [29, 30]) was exposed to the CERN neutrino beam, demonstrating the high recognition capability of the technique for neutrino interaction events.

The ICARUS T600 detector is the largest LAr TPC ever built, with a size of about 500 tons of fully imaging size [31]. Figure 1.5 shows a real electromagnetic cascade measured by this detector. The successful design, assembly and operation of the T600 detector, which relied on the industry support, represents the applications of concepts matured in the laboratory test to the kton scales, and opens the possibility for a new generation of very massive liquid argon detectors for neutrino and proton decay experiments [32]. The WARP experiment has also shown, with a 2.3 liters chamber, the possibility to use liquid argon for dark matter searches [33].

1.4 LAr TPC instrumentation

The particularities of the detection techniques described in the previous section, require special consideration of certain technical aspects, namely:

- The electronic read-out system must be capable of detecting the signal produced by a few thousand electrons.
- The level of purity of the LAr must be high enough so that the signal is not strongly degraded along the drift path.
- Photosensors must be used for triggering with prompt photons and to complete calorimetric information (this topic will be covered in the next chapter).
- The detector must be monitored with slow control sensors.

The present state of the art in the different solutions for each of these aspects are summarized below.

1.4.1 Charge Read-out system

One of the main problems which this detection technique must cope with is the relatively small amplitude of the signals. Typically, 1 mm of a minimum ionizing track delivers less than 10^4 electrons in LAr. The signal is even smaller at low electric fields due to the effects of the charge attenuation and the electron-ion recombination. The imaging of ionizing events requires, therefore, the use of low noise read-out electronics or charge amplification devices.

An example of low noise read-out is that of the ICARUS collaboration, based on previous experience on small scale prototypes [34, 35, 28, 36]. The sensitive readout device consist of several multiwire planes, as those described in previous section. The readout electronics is structured as a multichannel waveform recorder that stores the charge information collected by each sense wire during the drift of the electrons at a 2.5 MHz sampling rate. Each wire module (16 wires) is equipped with a current integrating amplifier feeding a 10 bit flash ADC that samples the (multiplexed) signal with a frequency of 40 MHz.

Among the charge amplification devices, LEM [26] seems to be one of the most appealing alternatives nowadays. A LEM consists of a printed board with metallization in both sides and equally spaced holes. If a sufficient potential difference is applied, the electrons are drawn into the holes, where the high electric field induces an avalanche multiplication. The metallizations can be read in a hole by hole mode or in a strip configuration, and hence act as position sensor of the TPC.

Another possibility which is widely used is to extract the electrons through the liquid-gas boundary by means of an electric field and then detect the proportional light produced when these are accelerated in a high electric field region [18].

1.4.2 Argon purification

In order to make long electron drift paths possible (of the order of one meter or more) LAr must be ultra-pure. An electron in the liquid undergoes about 10^{12} molecular collisions per second. Hence, impurities with large attachment probability must be kept at very low level, on the order or less than 0.1 ppb oxygen equivalent (ppb=10^{-9}), to achieve electron lifetimes in excess of a few milliseconds. The electro-negative impurities are mainly represented by oxygen, water, carbon dioxide and, in minor concentrations, some chlorine and fluorine compounds. If the impurity concentration is constant over the whole volume, the charge decreases exponentially with the drift time:

$$Q(t) = Q(t_0)e^{-\frac{t}{\tau}} \tag{1.5}$$

where τ is the mean lifetime of the electrons in argon. The lifetime is directly connected to the impurity concentration ρ by an inverse linear relationship [37]:

$$\tau[\mu s] \approx \frac{300}{\rho[ppb]} \tag{1.6}$$

where ρ is expressed in parts per billion O_2 equivalent units. Thus, the lifetime provides a direct measurement of the LAr impurity concentration.

Commercial LAr has a contamination level of the order of a few ppm of oxygen equivalent, this corresponds to a mean lifetime of only $0.3\,\mu$s, absolutely insufficient for a TPC[2]. A considerable amount of R&D has been performed in order to master the argon purification process [38, 31]. LAr can also be contaminated inside the cryostat by the degassing process of those parts (walls, electrodes, cables, etc.) covered by the (hotter) argon gas. Therefore, it is necessary not only to purify the LAr before the filling of the cryostat, but also to ensure a continuous purification inside the cryostat, forcing the LAr recirculation through a dedicated purifying unit. This unit is composed by several cartridges, each of which extracts from the liquid a given kind of particle (e.g.cartridges filled with copper eliminate the oxygen producing copper oxide). Using this system, purities up to several milliseconds have been achieved in the ICARUS experiment, corresponding to drift distances of more than 5 meters.

1.4.3 Slow control devices

Slow control devices are needed to monitor the experiment during the critical phases, such as the pumping period, the cooling down and filling with LAr, and the warming up. It is also important to monitor permanently the experiment during the data taking phase, as the interpretation of the data may depend in some parameters of the cryogenic environment. The slow control is composed of sensors that measure the temperature at different positions in one experiment; pressure gauges to measure the argon pressure, assuring that the equipment inside the cryostat is not damaged; level meters to measure the level of liquid argon in the cryostat; and purity monitors measure the amount of impurities in the medium. We will now review the main characteristics of these devices.

Level measurement

Level meters are based on the fact that liquid and gas phase have different dielectric constants. The LAr dielectric constant is $\epsilon = 1.520$, while that of the gas can be considered as 1, which means a variation of 52%. The sensors are capacitors that are partially immersed in the liquid and whose capacity increases with the liquid level.

[2] drift velocities are typically $\gtrapprox 1\text{mm}/\mu\text{s}$ so for drift distances $\sim$1 m lifetimes of $\sim$1 ms are needed

Two kind of levelmeter are commonly used in liquid argon detectors. Cylindrical capacitors present the advantage of not being sensitive to changes in temperature, which produce a mechanical dilatation. But on the other hand, they have a small capacity, which makes their precision limited. Multiplate parallel capacitors (see figure 1.6) have the advantage to have a high capacity due to the high number of plates, but they are temperature dependent (therefore they can increase their size producing different measurements for the same level at different temperatures). This makes cylindrical capacitors suitable to measure large lengths with small precision (> 1 mm), while multiplate ones are used to have a very precise control (precision ~ 300 μm) in a short range.

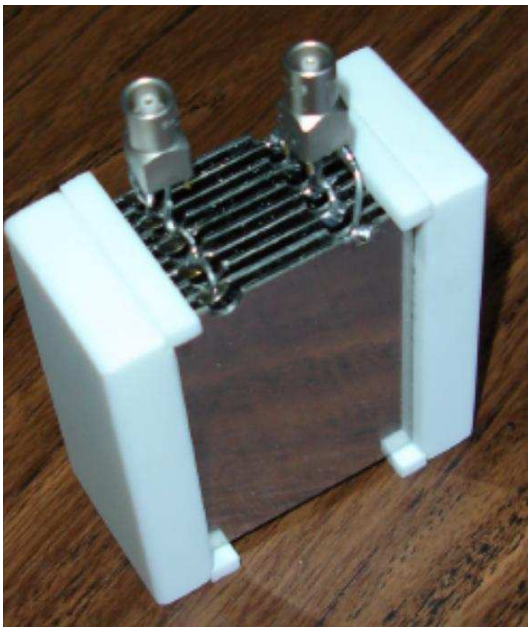

Figure 1.6: Multiplate capacitor used as level meter in liquid argon detectors. Plates are made of Invar while the supporting structure is made of Macor

Level meters are used not only during filling operation to control the liquid level. They are also useful to measure the level in the cooling tanks, external tanks commonly used to maintain the temperature in the main cryostat, to measure cooling liquid consumption, which is an indication of the heat input inside the main cryostat. During normal operation, they are used to check that liquid does not reach sensible parts of the detectors such as charge readout devices.

Temperature measurement

The measurement of the temperature is important during critical operations such as filling, but also during normal operation. The inside dewar is made of materials, usually mechanically connected, which have different heat capacities. If temperature differences are big, this may produce different expansion in some parts of the detector that may end up damaging the structures.

Temperature must be controlled during normal operation, as there are important properties like the electron drift velocity that depend on it. Moreover, for some charge readout devices such as a LEM, different temperatures produce different gains, so it is mandatory to measure and keep constant the temperature.

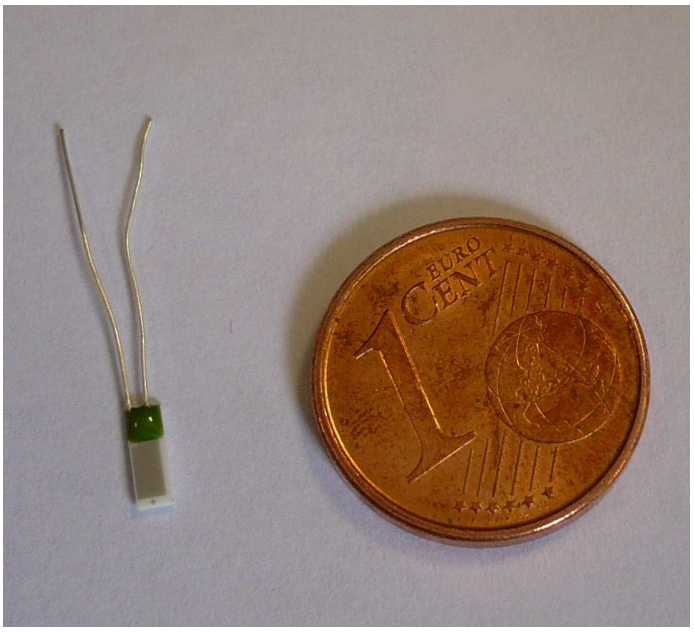

Figure 1.7: Pt10K temperature sensor.

Temperature is commonly measured using Pt10K resistors, small devices that change resistance with the temperature following a polynomial function. These resistors have typical sizes of 5 mm×2 mm×0.63 mm and their resistance changes from 10 KΩ at 0°C to a few KΩ at liquid nitrogen temperature. This make these devices easy to handle, install and operate. Figure 1.7 shows one of these resistors.

Purity measurement

Continuous control of the liquid purity is necessary in order to know the electron absorption in the liquid argon and the relationship between the measured and the originally produced charge.

Although the shape of the emitted light signals in the liquid argon can give an indication of the purity [39], usually a dedicated purity monitor is installed inside the experiment. Figure 1.8 shows a purity monitor.

The monitor itself is a small scale TPC. The idea behind it is to measure the ratio between the charge extracted from a photocathode and the charge remaining after drifting for a given distance in liquid argon. The monitor is composed by a photocathode which is illuminated by an optical fiber. The electrons produced are drifted in an electric field and an induction signal proportional to the number of electrons is generated in the cathode and the anode. By measuring these two signals and computing the ratio between them and with the the distance between anode and cathode, which is the length of the device, one can obtain the electron lifetime in the liquid, which is connected with the purity through equation 1.6. The length of purity monitors (equal to the electron drift distance) is typically between 10 and 20 cm. Since electric fields are of the order of 100 V/cm, this device is sensitive to electron lifetimes in the range from tenths to hundreds of microseconds, although this range can be adjusted by changing the drift distance and the electric field.

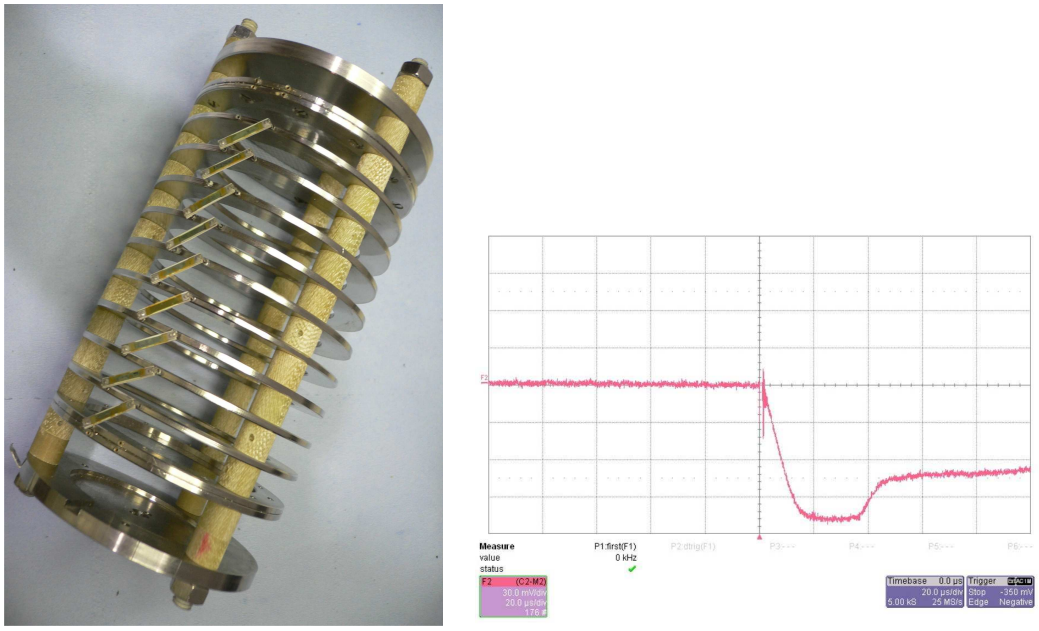

Figure 1.8: Left: Purity monitor. It is composed by a photocathode, on the bottom, from which electrons are extracted with a light pulse. An electric field to drift them is created by a voltage difference, while the rings seen on the photo improve its uniformity. Charge collection is done in the anode, in the upper part. Typical heights are between 10 and 20 cm. Right: Purity measurement. The initial fall corresponds to charge extracted from the photocathode. The later rise corresponds to the charge collected in the anode.

1.5 Conclusions

Liquid argon has some properties (density, radiation length, high ionization density, high scintillation light yield, etc.) that make it a great candidate for target material in a particle physics experiment. In combination with the TPC technique, it offers unique calorimetric and imaging capabilities. Since the first proposal of such a detector, several of them have been constructed and operated, showing that all the technical challenges (cryogenic operation, purification, etc.) can be properly solved.

In the following chapters, we discuss two instances where LAr TPCs can make decisive contributions: the understanding of what dark matter is made of and whether ordinary matter is stable.

Chapter 2

Characterization of large area photomultipliers and its application to dark matter search with noble liquid detectors

2.1 Introduction

As explained in the previous chapter, particle interactions in liquefied noble gases produce charge by means of *ionization* of the atoms of the medium and *light*, by the de-excitation of the formed dimers [40]. Charge offers information on the energy deposited by the particle, its position and in the case of long tracks, it provides a useful variable for particle identification. On the other hand, light information is related to the determination of the primary interaction time of the particle (the so called t_0), due to its almost immediate transmission speed.

However, as explained in the next chapter, reactions involved in dark matter searches produce energy deposits in the range $10 - 100$ keV, which makes charge alone insufficient for particle identification, requiring a good light detection for an optimal differentiation between signal and background.

Furthermore, charge readout devices have larger amount of radioactive components compared to the light readout systems (for which contamination is being reduced to limits well below experimental sensitivities). Because of this there are several experiments [18, 41] in which the charge is extracted from the liquid to the gas phase with an electric field producing scintillation light and as a result a second light component is read instead of charge.

Therefore, the light readout is of capital importance for dark matter experiments where, in addition to t_0 determination, the light is needed for energy measurements (by inferring the produced light and charge) and even for background discrimination through particle identification.

For light readout, the use of photomultiplier tubes (PMTs) is highly recommended as their time resolution allows to distinguish photons produced in a triplet state dimer (slow component) from those produced in a singlet state (fast component) [42]. This helps to improve background rejection capabilities. On the other hand, their high gain (up to 10^9) makes possible the detection of single photons without external amplification. One of their main advantages is that the market offers a broad catalogue of size and photocathode shape options, so they can be accommodated

to different size experiments. Also, PMTs can be used in cryogenic conditions, working immersed both in liquid argon and liquid xenon.

Therefore, PMTs are a crucial element for noble-liquid detectors. Even though the manufacturers provide data for each PMT model (gain, dark current, linearity, etc.), the values presented in the specification data sheet are usually too generic, based on averages over many PMTs, not specific to the purchased one. Non negligible deviations from the average behaviour can be expected for a particular PMT. Moreover, companies do not usually provide calibration data at cryogenic temperatures ($\sim$ 87 K for liquid argon). For these reasons PMTs must be characterized individually as precisely as possible in the laboratory.

Currently running noble liquid dark matter detectors like WARP [18] and XENON [41], employ small size phototubes ($\sim$ 2-inch window) because of the relative small active volume of such experiments (few liters). As a result of the scaling up of future detectors to improve dark matter detection capabilities, the size of the installed photomultipliers will probably be increased: the use of larger photocathode PMTs will allow coverage of bigger surfaces at lower cost, reducing at the same time the non sensitive surface (increasing the geometrical acceptance). Indeed, the design of new prototypes like ArDM [43], of about one tonne of LAr, already incorporates the use of large area photocathode tubes (8-inch window).

According to the requirements needed for a dark matter experiment (see section 2.4), we have selected two PMT models. Several units of each model have been purchased and tested at the cryogenic laboratory of the High Energy group of Granada University, employing setups specially designed for this task. Results of those tests are given in section 2.5. After the test campaign, the PMTs were sent to CERN and integrated in the setup of the ArDM experiment, as will be explained in chapter 3, which is currently under development.

2.2 Photomultipliers Overview

Photomultiplier tubes are light detection devices that produce a current proportional to the incident amount of light. Their working principle is the photoelectric effect, discovered in 1887 by Hertz and explained successfully by Einstein in 1905, for which he was awarded in 1921 with the Nobel price. When the energy of a photon is higher than the work function of a given material, the photon can transfer all of its energy to an electron (called hereafter *photoelectron*) of the material emitting it to the outside. The produced photoelectrons are amplified inside the vacuum tube by means of a dynode chain producing a macroscopic charge.

The first photoelectric tube was produced in 1913 by Elster and Geitel. Investigation on photocathodes led then to the discovery of a compound material made of Ag-O-Cs that could produce a photoelectric sensitivity about two orders of magnitude higher than previously used photocathodes. Since then, various photocathodes have been developed one after another, including bialkali photocathodes for the visible region, multialkali photocathodes with high sensitivity extending to the infrared region and alkali halide photocathodes intended for the ultraviolet region. In addition, photocathodes using compound semiconductors such as GaAs and InGaAs have been developed, which offer high sensitivity from the ultraviolet through the near infrared region.

Together with the discovery of the photocathodes, the other piece necessary for the development of the photomultiplier tubes was the discovery of secondary emission multipliers (dynodes). The first report on secondary emissive surfaces was made in 1902. In 1935 a triode photomultiplier tube was produced with a photocathode combined with a single-stage dynode. In the next year photomultiplier tubes with multiple dynode stages were already manufactured. The next steps of electrostatic-focused tubes together with bialkali photocathodes led to the beginning of photomultiplier tubes as we know them today.

Figure 2.1 shows the basic structure of a PMT and the basic processes that take place when a PMT is illuminated [44].

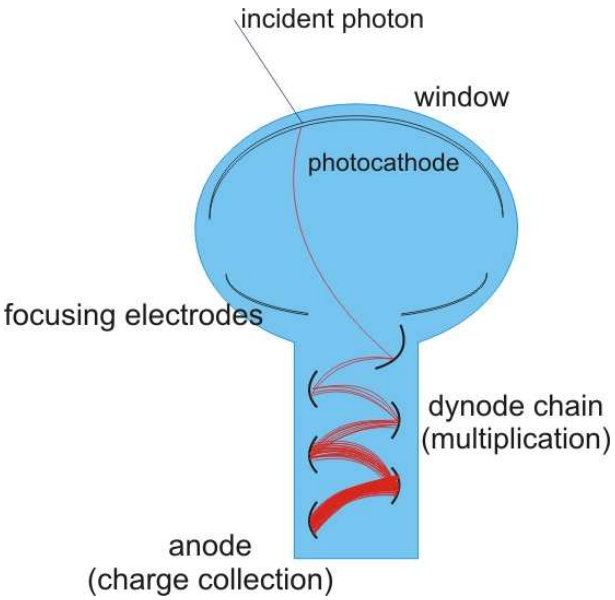

Figure 2.1: Schematic of a PMT and its working principle. An incident photon passes through the *window* of the PMT, reaches the *photocathode*, where it may produce an electron. This *photoelectron* is focused by the *focusing electrodes* towards the first dynode and then new electrons are generated in the *dynode chain*, until the *anode* is reached and the final signal is collected.

The basic constituents of a PMT are the following:

- Window. It is the most external part of the phototube. The composition is very important, as it will impose a low cutoff on the photons arriving at the photocathode, depending on its ultraviolet absorption. This cutoff can be from 115 nm for MgF_2 up to ∼300 nm for borosilicate glass.

- Photocathode. It is the sensitive part of the PMT in which the photoelectric conversion of the incoming light takes place. Its composition will determine both, the highest wavelength for which photoelectric effect takes place, and the conversion efficiency (quantum efficiency). At cryogenic temperatures the photocathode resistance will dramatically increase, being necessary to deposit it on some underlayer (usually Pt) for a correct working of the tube.

- Focusing electrodes. In order that the photoelectrons emitted by the photocathode reach the first dynode, it is important to focus them by means of electric fields, which are generated by the focusing electrodes. They must guarantee a high collection efficiency, defined as the ratio of the number of electrons landing on the effective area of the first dynode to the number of emitted photoelectrons.

- Dynode chain. Photoelectrons emitted from the photocathode are multiplied by the first dynode through the last dynode, getting an amplification factor $\lesssim 10$ per dynode, with total current amplification ranging from 10 up to 10^9 times, and then sent to the anode. The

dynode chain is constructed from several to more than 10 stages. Each dynode is composed of emissive materials, such as alkali antimonide, BeO, MgO, GaP, and GaAsP, coated on a substrate electrode. The design must optimize collection efficiency and transit time, while avoiding light and ions feedback from the latest stages.

- Anode. The anode of a photomultiplier is an electrode that collects secondary electrons multiplied in the cascade process through multistage dynodes and outputs the electron current to an external circuit. Generally they are manufactured in the form of a rod, plate or mesh electrode. An adequate potential difference has to be established in order to prevent space charge effects and obtain a large output current.

There are several characteristics that define a PMT and the amplification process that takes place inside it. The different values of these parameters will make the PMT suitable for a certain type of applications.

2.3 Photomultiplier Properties

2.3.1 Quantum Efficiency

Quantum efficiency (QE) is defined as the ratio between the number of electrons produced in the photocathode and the number of incoming photons. This value depends on the photons wavelength. Usually, quantum efficiency can only be measured convoluted with collection efficiency, a property of the dynode chain. Typical values of the quantum efficiency are between 10 and 20%. Measurements of QE are shown in section 2.5.1.

2.3.2 Gain

Gain is the factor of amplification of the dynode chain. It is defined as the number of electrons in the output of a single electron signal. The dynode multiplication can be considered as a poissonian process, and hence the gain shows a gaussian distribution. The RMS of this gaussian and the height of the peak compared to that of the region where no electrons are produced (*peak to valley* ratio) are important properties to determine the energy resolution of a PMT [45].

2.3.3 Collection efficiency

The electron multiplication mechanism of a photomultiplier is designed with consideration to the electron trajectories so that electrons are efficiently multiplied at each dynode stage. However, some electrons may deviate from their favorable trajectories, not contributing to multiplication. In general, the probability that photoelectrons will land on the effective area of the first dynode is termed the collection efficiency. This effective area is the area where photoelectrons can be multiplied effectively at the successive dynode stages without deviating from their favorable trajectories. This value increases with the voltage between cathode and first dynode, being almost 100% for a wide range of values.

2.3.4 Timing properties

PMTs are fast detectors. Their time response is primarily determined by the transit time required for the photoelectron emitted from the photocathode to reach the anode after being multiplied. Figure 2.2 shows the basic parameters that define a PMT time response:

- Transit time (TT). Time for the photoelectrons to go from the photocathode to the anode. Typical values are from 10 to 100 ns.
- Rise time and fall time. Times for the output pulse to increase from 10 to 90% and to decrease from 90 to 10% respectively. Typical values are of a few ns.
- Transit time spread (TTS). Fluctuation in transit time for photoelectron pulses.

These parameters depend on the dynode type and the supplied voltage.

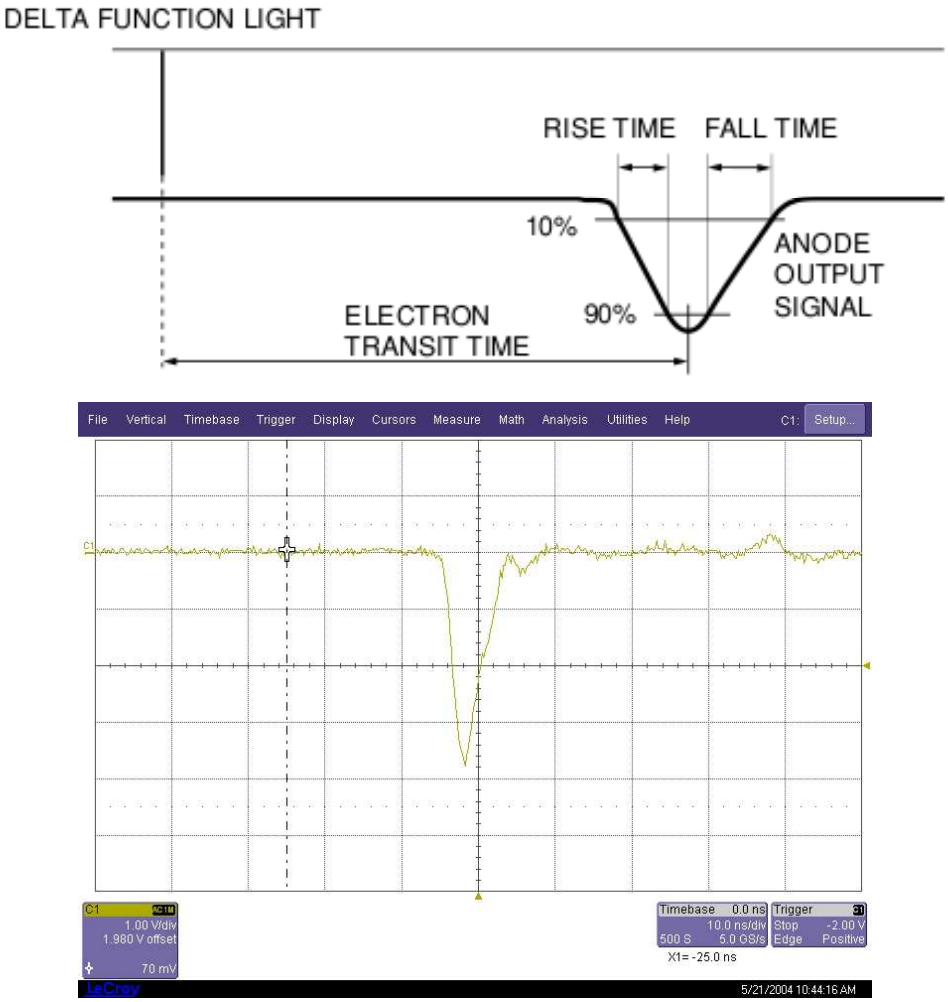

Figure 2.2: Top: Schematic of a PMT time response. Bottom: Actual shape of the PMT response as captured in the oscilloscope (2 V/division and 10 ns/division for Y and X axis respectively).

2.3.5 Dark Counts

Ideally, in the absence of light the photomultiplier output charge should be zero. However, there are certain physical effects that make that some current is always present. This is the so called

dark current and the apparent hits on the photomultiplier are the so called *dark counts*. Some of the most important processes producing dark counts are [44]:

- Thermoionic emission from the photocathode and dynodes;
- Leakage current (ohmic leakage) between the anode and other electrodes inside the tube and/or between the anode pin and other pins on the bulb stem;
- Photocurrent produced by scintillation from the glass envelope or the electrode supports;
- Field emission current due to extraction from dynodes by the applied voltage;
- Ionization current from residual gases;
- Noise current caused by cosmic rays, radiation from radioisotopes contained in the glass envelopes and environmental gamma rays;

Dark counts depend on very different parameters, such as the applied voltage, temperature or previous expositions of the PMT to intense sources of light.

2.3.6 Linearity

The response of a PMT should be proportional to the incident light. However, this only happens up to certain light illumination levels. Deviations from ideal behavior are primarily caused by anode linearity characteristics, that only depend on the current value if the voltage is constant. For pulsed sources, anode linearity is mainly limited by space charge effects, due to the magnitude of the signal current: when an intense light pulse enters a PMT a large current flows in the latter dynode stages, increasing the space charge density and causing current saturation. In general, linearity improves by increasing the supply voltage and thus the electric field between dynodes.

2.3.7 Afterpulsing

When a PMT is operated in a pulse detection mode as in scintillation counting or in laser pulse detection, spurious pulses with small amplitudes may be observed. Since these pulses appear after the signal output pulse, they are called afterpulses. There are two types of afterpulses, one with a very short delay after the output signal caused mostly by photons produced by elastic scattered electrons on the first dynodes (late pulses, $\sim$20-100 ns after the primary signal), and one with a longer delay ranging (after pulses, $>$300-1000ns up to several microseconds after the primary signal). The latter case is caused by positive ions which are generated by ionization of residual gases in the photomultiplier tube. They return to the photocathode and produce multiple electrons which cause after pulses. The time difference with the primary photon depends on the position of the PMT in which the ions are produced.

2.4 PMT requirements for photon liquid argon counting experiments

Photomultipliers can be used mainly in two ways. On one hand, as light speed makes light signals to arrive immediately, PMT can trigger an experiment in the exact moment in which an event happens. On the other hand, and as already discussed, a fraction of the energy deposited in a medium by an ionizing particle is released in the form of light. Hence detection of these photons

can improve the calorimetric reconstruction of the events. This fact becomes more important in experiments in which the deposited energy is small, as the collected charge is not enough to measure the energy with enough accuracy . Charge information must be then completed with the PMT information on the number of photons released.

In the framework of liquid argon experiments in which photon counting is required, such as dark matter experiments, the first property required for a PMT is, obviously, to work properly at cryogenic temperatures O(100 K). This strong requirement is generally not satisfied by conventional PMTs. Photocathodes are usually semiconductors, thus when temperature is reduced to such low values, the cathode resistance can increase by several orders of magnitude. This can cause a large voltage gradient in the photocathode, resulting in a poor collection efficiency at the first dynode [46, 47]. To avoid this undesirable effect the photocathode has to be deposited on a conducting substrate. Some companies are able to manufacture special coated PMTs for cryogenic applications.

Regarding the size of the PMT, in the case of large volume experiments, the size of instrumented areas makes necessary to install large area PMTs in order to reduce costs and readout channels. Spherical PMTs are build up to 8" or even more, and as they have no plastic housing, their spatial packing is better than the one offered by other a priori more compact solutions, such as square or hexagonal PMTs. We will focus on this kind of PMTs, similar to the one shown in figure 2.3.

Figure 2.3: Photo of one of 8" PMT tested in this work (ETL9357). The voltage divider can be appreciated soldered to the pins at the bottom of the PMT. The spherical photocathode, on the left, appears covered by the platinum underlayer.

Another important requirement is a good PMT response over a wide range of illumination levels. Signals ranging from the single photoelectron (pe) up to several hundreds of photoelectrons (if the particle interaction takes place close to the photocathode) can be expected in large detectors. An adequate PMT gain (G) should allow the detection of both types of events. The peak voltage

of a signal can be estimated considering that the output charge of the anode will follow a Gaussian distribution in time, with RMS equal to the transit time spread of the electrons. If we assume a 50 Ω coupling between the anode and the electronics, then the integral of the output signal will be $50 \cdot G \cdot q$, with q the electron charge. The signal amplitude can be approximated by $A \sim 50 \cdot G \cdot q / TTS$ which for a 10^7 gain and a typical transit time spread (TTS) of 5 ns (for the considered ETL and Hamamatsu PMTs tested in this work the values are 4 ns and 2.4 ns respectively [48, 49]) gives 16 mV output peak voltage. Hence, a nominal gain close to this value would fulfill the requirements in the 1–100 photoelectrons range. As explained later in the text, the gain is extracted from the single photoelectron charge spectrum, the so called Single Electron Response (SER), obtained with very low illumination levels. Besides the gain, the single photoelectron charge spectrum allows the study and characterization of other important PMT parameters (peak to valley, peak spread, etc.) which determine, for instance, the PMT energy resolution [45].

In order to estimate the number of photoelectrons produced in a single event, the response of the PMT should also be proportional to the incident light intensity. Deviations from the ideal behavior are primarily caused by anode linearity characteristics which, for pulsed sources it is mainly limited by space charge effects due to the magnitude of the signal current. An intense light pulse increases the space charge density and causes current saturation. Linearity should be at least granted up to levels of 100 pe.

PMTs may be used for triggering purposes, in which case dark counts are a source of concern. Although they can be efficiently suppressed by time coincidence among several PMTs, a low dark count rate for each individual PMT is highly desirable.

Concerning the spectral response of the PMT, as mentioned previously, the scintillation light emitted by excited argon dimers has a wavelength peak at ∼128 nm, where standard PMTs are blind. Only tubes made of MgF_2 windows extend the range of visibility down to 110 nm. Unfortunately, at the moment no large photocathode PMTs (8") are manufactured with this special type of window, so typical experiments make use of coating materials like TPB to shift the light to the 400–450 nm region where the PMT shows its best performance in terms of quantum efficiency. This is a crucial parameter for dark matter experiments where very dim signals are recorded.

The timing resolution is another property which characterizes the PMT performances but this parameter does not seem to be an issue. Large photocathode PMTs actually present in the market show TTS values in the order of few ns, fast enough for the requirements of a dark matter detector.

Finally, the phototubes must be placed inside the detector sensitive volume so they should be manufactured using special low background materials. Natural radioactivity from material compounds is a continuous source, among others, of low energy neutron and alpha particles which are the most pernicious source of background. Companies are able to manufacture a low background version of many PMT models under request.

Among the companies surveyed, only Electron Tubes Limited [48] and Hamamatsu [49] can offer large photocathode PMTs suitable to work under cryogenic conditions. Out of the available models, we have chosen those closest to the required specifications: the 9357-KFLB from Electron Tubes Limited (ETL) and the R-5912-MOD from Hamamatsu.

Two units of each model have been tested. Their main properties are summarized in table 2.1. In particular, they have nominal gains around 10^7 and peak quantum efficiencies close to 20%. Both models can be manufactured in low background glass.

Hereafter, the tested ETL and Hamamatsu phototubes will be referred to as ETL1, ETL2 and HAM1, HAM2 respectively.

The voltage dividers have been made using a custom PCB double-sided printed circuit board following the design provided by each manufacturer. In order to avoid changes in the values of the different components of the voltage divider at cryogenic temperatures, specially manufactured

Manufacturer	Model	Size	Gain	TTS	Dark Currents	QE (@ 420nm)
ETL	9357 KFLB	8"	1.1×10^7	4 ns	10 nA	18%
Hamamatsu	R-5912-MOD	8"	10^7	2.4 ns	50 nA	22%

Table 2.1: PMT models tested in this study (values from manufacturer generic data sheet).

electronic resistors and capacitances with guaranteed stability up to LAr temperatures [50] have been used (shown in figure 2.4).

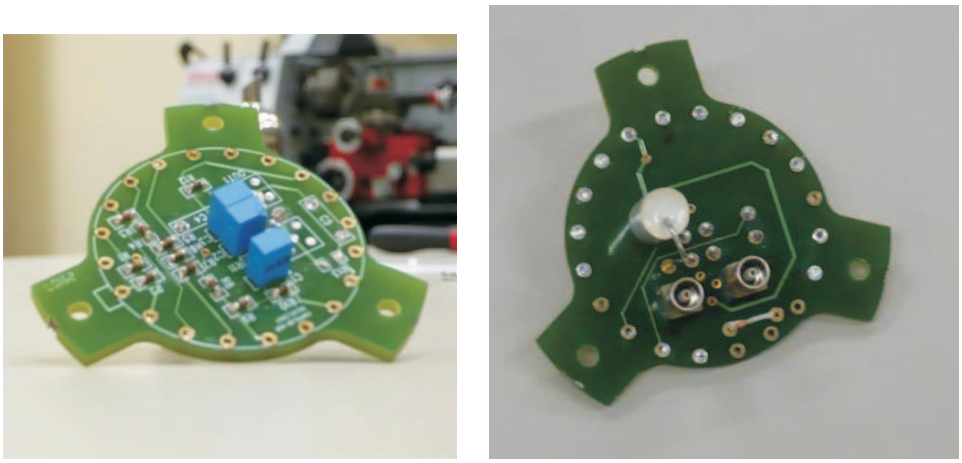

Figure 2.4: Cryogenic voltage divider used during liquid argon operation. Left: top side, where most of the electronic components are soldered. Right: bottom side, where dynode pins are soldered. The two LEMO connectors for HV and signal readout are clearly visible.

2.5 Measurements

In this section we will describe the measurements carried out to characterize the selected PMTs. We carefully assess whether they match the requirements exposed in the previous section.

These measurements have been performed in the Laboratorio de Altas Energías of the High Energy group of University of Granada (shown in Figure 2.5). The laboratory (∼120 m^2 surface, 6 m height) holds a 3000 l LAr reservoir, which is periodically filled by Air Liquide. Electronic equipment and the black box light blind needed for PMT tests in air and cryogenic environment are shown on the photo.

We have first measured the QE of the PMTs (section 2.5.1) both at room temperature and in liquid argon. In a second step other PMT characteristics like gain, dark count rate, etc., are measured in cryogenic environment using light pulses.

2.5.1 Quantum Efficiency

A precise knowledge of the PMT quantum efficiency as function of the incident photon wavelength (λ) will be of major importance for a dark matter detector which aims to exploit the full capabilities

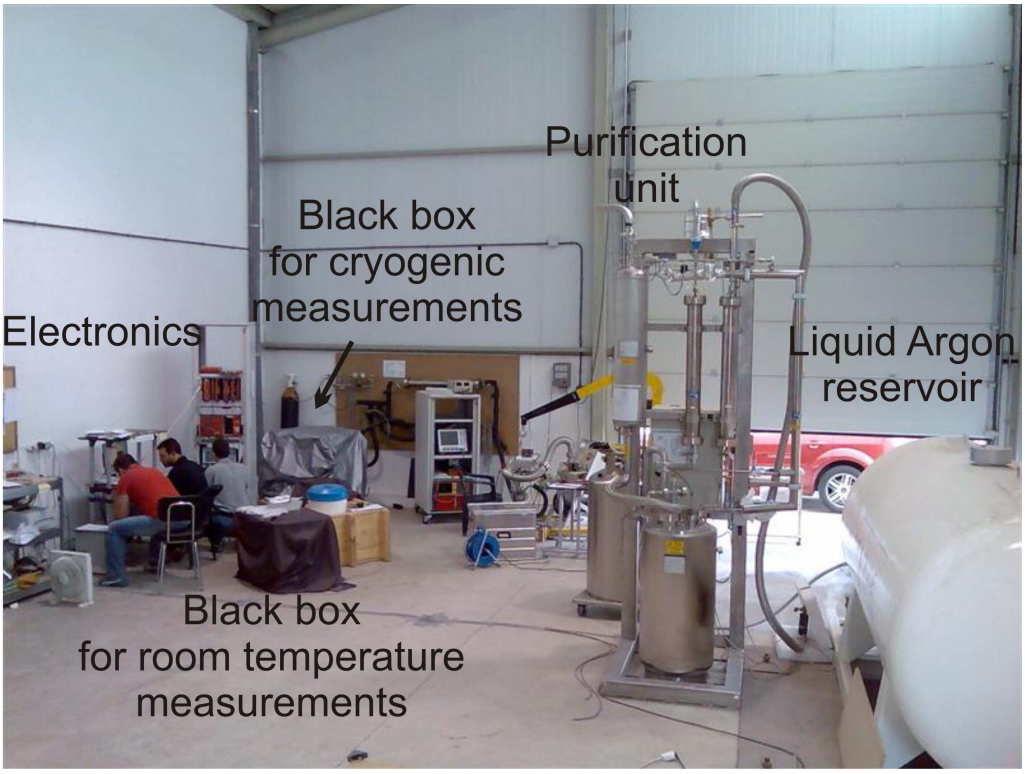

Figure 2.5: Laboratorio de Altas Energías at Granada University.

of a PMT, not only the trigger potential as a fast light detector but also the calorimetric one. Among other variables, the parameterization of QE as a function of λ is needed to infer the total amount of scintillation light released inside the active detector volume, following a particle interaction.

The method used for measuring the spectral response of the PMT is based on the comparison of its output signal with the response of a calibrated detector, in our case a photodiode. This measurement can be done by interchanging the calibrated and the unknown photosensor after each measurement at a fixed value of λ, or by splitting the light beam in two, taking both measurements simultaneously. In order to minimize the errors induced by the light source instabilities and misalignment of the devices, the second method was followed.

The measurement is done, first, at room temperature (*hot* spectral response) and then combined with the data obtained in liquid argon to compute the final value *in cold*. As expected, it is found that the quantum efficiency properties of the tested PMTs change substantially with temperature, so a careful measurement of QE(λ) in cryogenic conditions is mandatory.

The following subsections describe the measurement techniques and the obtained results on the quantum efficiency measurements at room and LAr temperatures.

Quantum Efficiency at room temperature

Figure 2.6 shows the experimental setup used to measure the quantum efficiency at room temperature. It is composed of a light source, a monochromator and a light-tight box where the photosensors are placed.

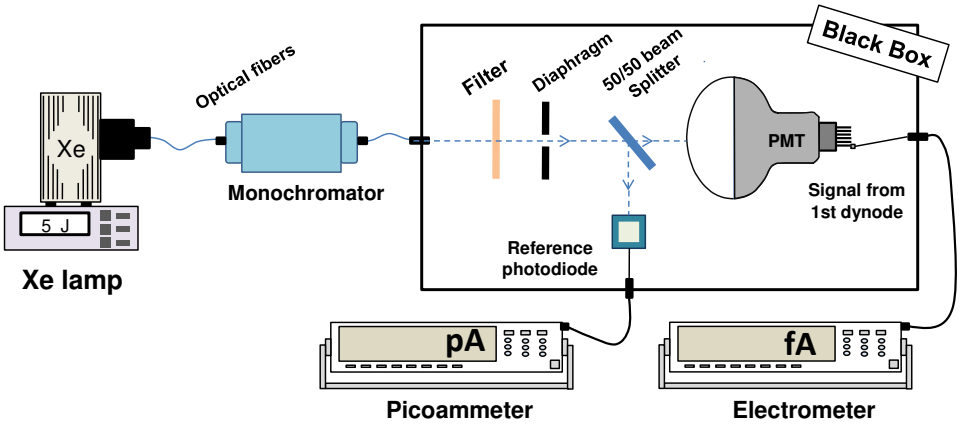

Figure 2.6: Schematic drawing of the setup used for quantum efficiency measurements at room temperature.

The light source should provide an spectral distribution covering the range of interest (300 nm - 600 nm) with a high light intensity. The ORIEL Newport 6427 Xenon lamp [51] matches those requirements. It can be used in pulsed mode (maximum energy of 5 J) and the output can be easily coupled to the monochromator by means of an optical fiber. The stability of the lamp has been tested by measuring its output flux during several hours and it has shown deviations below 1 % in time slots of 5 minutes (duration of a single QE measurement). The lamp is also equipped with a shutter.

The monochromator (Spectral Products Digikrom CM110 CVI [52]), controlled with a computer via the RS-232 port, is equipped with a 2400 g/mm grating which allows the selection of a particular wavelength between 180 and 680 nm (peak at 240 nm) with an accuracy of ± 0.6 nm.

A second optical fiber is used to send the monochromatic light into the aluminum box which provides a completely dark environment and acts as a Faraday cage. The box houses a filter (to block any shorter *harmonic* wavelength from the monochromator), a diaphragm (to reduce the size of the light spot, such that it completely fits inside the photodiode sensitive area), a 50/50 Polka-dot beam splitter (by Edmund Optics [53]) and the two photosensors. The reference detector is a Hamamatsu S1337-1010BQ photodiode, with 10×10 mm^2 active area. It has been calibrated by the manufacturer. The setup is completed with two devices to measure independently the current produced by the reference photodiode and the photocathode of the tested PMTs: a Picoammeter (mod. 6485) and an Electrometer (mod. 6514) both from Keithley [54].

All the optical components inside the aluminum box and the photodiode are fixed in an optical bench (see figure 2.7), together with the last portion of the optical fiber. These components are aligned in a dark room prior to installation in the aluminium box, and the diaphragm is adjusted in such a way that the light beam fits inside the photocathode. After this, the system is installed

inside the aluminium box, and then the PMT is placed in such a way that the free light spot hits on its center.

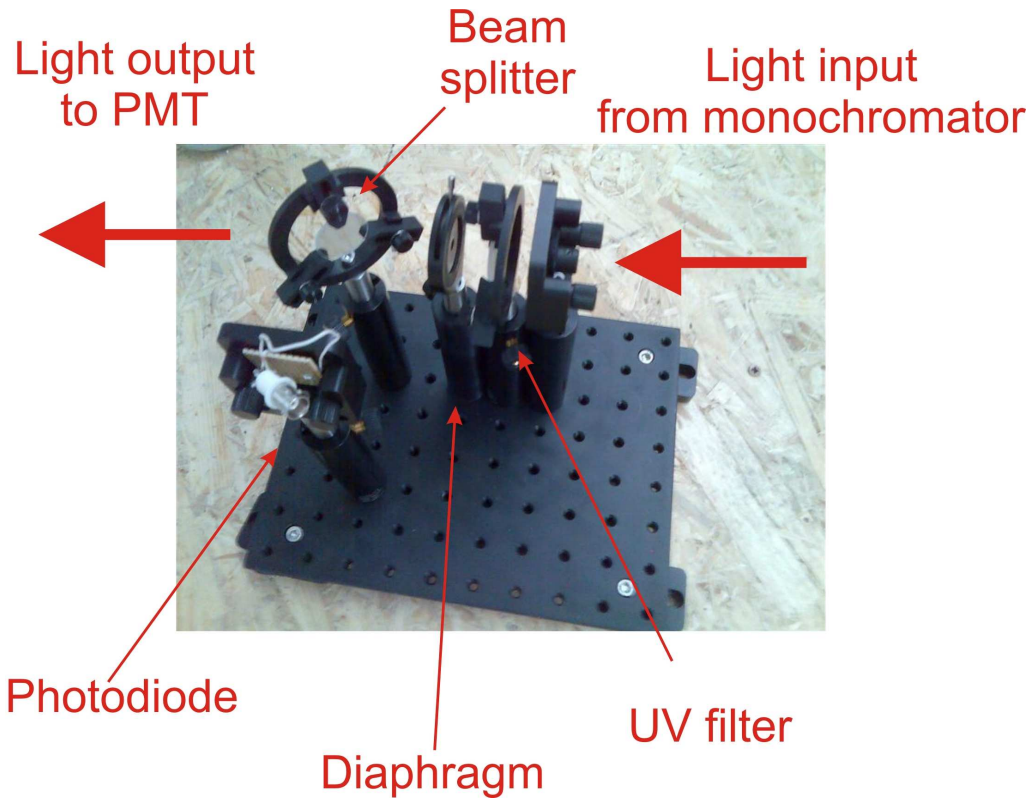

Figure 2.7: Optical bench used to split the light inside the dark box.

The quantum efficiency measurement comes from the comparison of the currents produced in the photodiode and in the first dynode of the unknown PMT. In order to ensure an optimal collection efficiency between the photocathode (K) and the first dynode (D_1), a gradient of ΔV_{K-D_1}= 300 V is kept between these two points. According to the manufacturer, the collection efficiency is maximum for any voltage between 100 and 500 Volts, but we select this value as it is close to the one that the PMT will have during its normal operation. Even in absence of light, this gradient generates a small leakage current (∼10 pA) which must be subtracted from the measurements in presence of light (shutter lamp open).

In order to get rid of systematic effects coming from the beam splitter inaccuracy (5% according to the manufacturer) two measurements were carried out exchanging the positions of PMT and photodiode. In order to properly combine these two measurements, one can write an equation for the amount of photons arriving at each element in both cases. Indeed, in the configuration shown in figure 2.6, the photodiode receives a fraction α of the incident light measuring an intensity I^r (reflected in the splitter) whereas the PMT receives the transmitted one (1-α) and measures I^t. We can write:

$$\frac{I^t_{PMT}}{QE_{PMT}\cdot(1-\alpha)} = \frac{I^r_{PD}}{QE_{PD}\cdot\alpha} \tag{2.1}$$

When the two photodetectors are exchanged:

$$\frac{I^r_{PMT}}{QE_{PMT}\cdot\alpha} = \frac{I^t_{PD}}{QE_{PD}\cdot(1-\alpha)} \tag{2.2}$$

Combining equations 2.2 and 2.1 it follows:

$$QE_{PMT} = QE_{PD}\cdot\sqrt{\frac{I^r_{PMT}}{I^t_{PD}}\frac{I^t_{PMT}}{I^r_{PD}}} \tag{2.3}$$

which is independent of the beam splitter accuracy. Hence, the geometric average of both measurements is taken as the final value.

The measurement procedure is as follows: once the optical setup is properly aligned and placed in the aluminium box together with the PMT, the box is closed and covered with a cloth, so no light will go inside it. High voltage is supplied to the PMT. The lamp is turned on, the monochromator is set to the desired wavelength and the current in the PMT and the photodiode is measured by an electrometer and a picoammeter during ∼1 minute. Afterwards, the monochromator is set at a wavelength of 200 nm. For this wavelength the filter inside the box allows no light to come in, and also the PMT is blind, so it acts as a shutter (actually, if one compares the measured current with that measured when the lamp shutter is closed, differences are below 1%). Current is measured again for ∼1 minute for both the PMT and the photodiode (for the photodiode this measurement is actually 0), and then, the intensity due to the light is simply the difference between both measurements. A LabView [55] interface was developed to automatize the measurement procedure for as many wavelengths as desired. Once finished, the places of the PMT and the photodiode are changed and the second measurement is performed.

Figure 2.8 shows the results obtained for the measurements of quantum efficiency at room temperature.

The points, in steps of 10 nm, follow a smooth curve. The quantum efficiency shows maximum values in the range 15–20% for a wavelength of about 400 nm. In the vicinity of the peak, the Hamamatsu models show an almost flat region between 350–450 nm, whereas the ETL PMTs present a steeper behaviour.

Quantum efficiency at LAr temperature

To perform the measurements *in cold*, the previous experimental setup has to be modified (see figure 2.9). This measurement requires the tested PMT to be fully immersed in liquid argon for long periods of time (several hours). A special light-tight cryostat is used for that purpose, ensuring stable temperature conditions. It is equipped with two feedthroughs to feed the 1^{st} dynode and read-out the current with the Electrometer, and to pass the optical fiber which illuminates the PMT. Inside the cryostat, the fiber is positioned very close to the PMT surface such that dispersion effects due to a change of the medium conditions are negligible. A specially designed supporting structure made of stainless steel and polyethylene disks houses the PMT and fixes the fiber inside the cryostat. Figure 2.10 shows this structure immediately after removal from LAr bath.

On the other hand, the Hamamatsu S1337-1010BQ reference photodiode remains at room temperature in order to keep valid the manufacturer calibration. It is placed inside an aluminum light-tight box. Contrary to the measurement at room temperature, now the photodiode is only used to monitor the lamp. The reference used to measure the quantum efficiency of the PMT in liquid argon is the quantum efficiency of the same PMT at room temperature. As these two measurements can not be done simultaneously on time, we use the photodiode to check that the xenon lamp conditions are the same during both measurements.

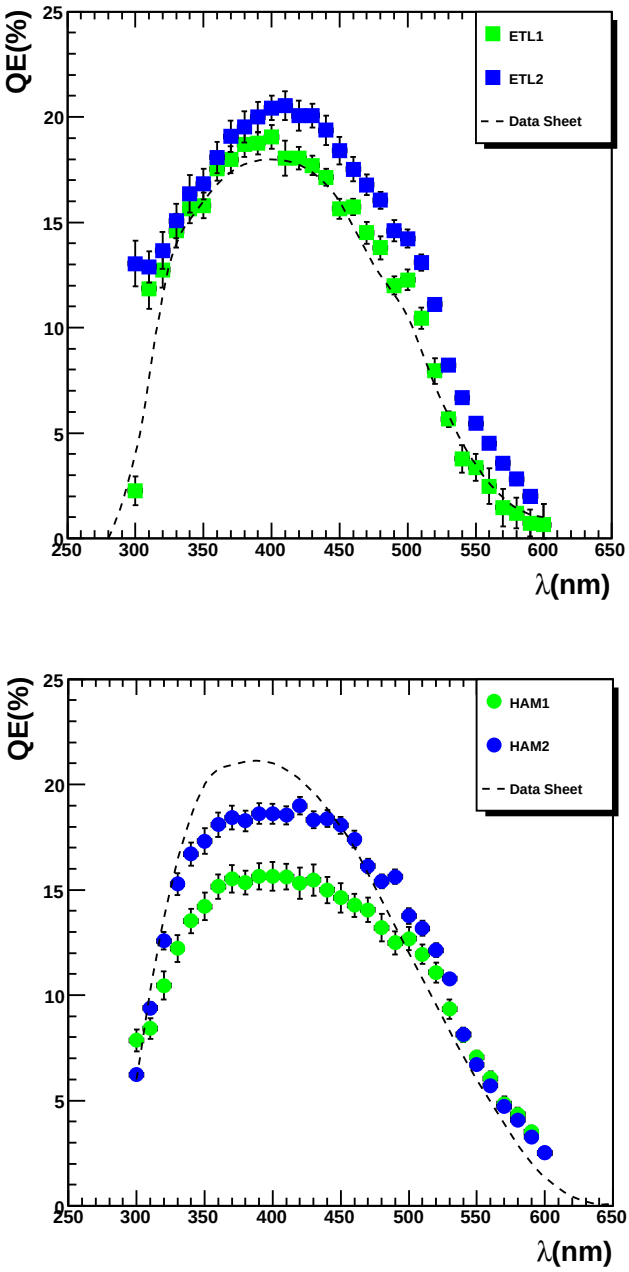

Figure 2.8: Quantum efficiency of the ETL (top) and Hamamatsu (bottom) PMTs as measured at room temperature. Curves from manufacturers are included. Hamamatsu data are for a PMT without Pt underlayer, which accounts for the observed differences.

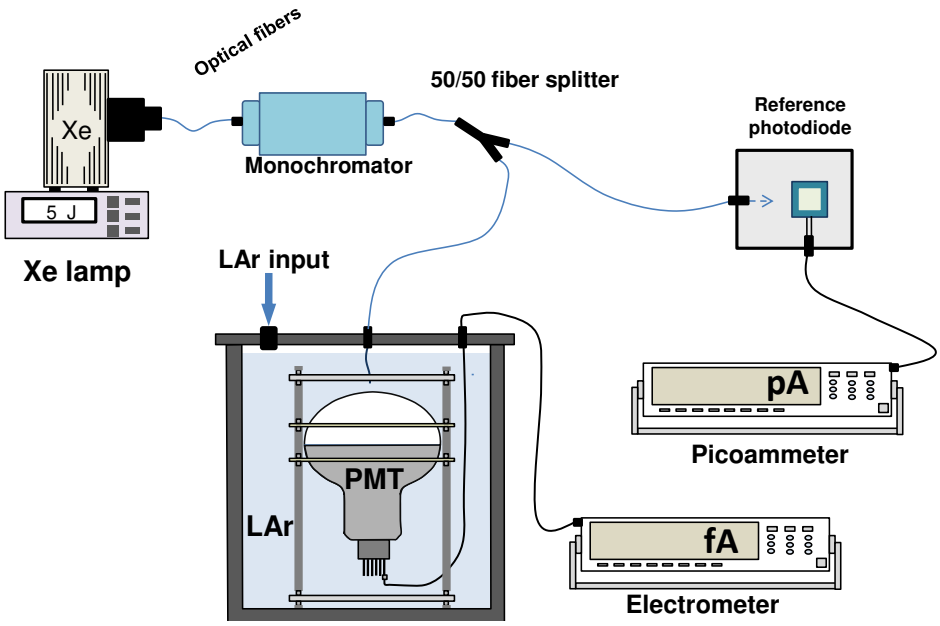

Figure 2.9: Schematic drawing of the setup used for quantum efficiency measurements at LAr temperature.

The Xe lamp, the monochromator and the charge readout devices are the same as in the previous measurement. The Polka-dot beam splitter is replaced by a 50/50 optical fiber splitter (Ocean Optics [56]) allowing a stable light flux between the monochromator and the two photosensors. As previously stated, the reference will be the PMT itself, so deviations from the perfect split are not important as far as the fraction arriving at the PMT is always the same, which must happen if the fiber is not moved.

The measurement of the quantum efficiency at liquid argon temperature is done in two steps. First, we measure the quantum efficiency at room temperature, by keeping empty the dewar. Then, we make a second measurement filling the dewar with liquid argon but with no other change in the setup. Both measurements can be trivially related as follows.

At room temperature, as a function of the fraction of light on each branch of the optical fiber, the intensity generated in the photodiode I_{PD}^{hot} can be written as:

$$I_{PD}^{hot} = N_r \cdot \alpha \cdot QE_{PD} \tag{2.4}$$

N_r being the number of photons per unit of time before entering the fiber splitter, and α the fraction of photons split to the photodiode. Note that although it is kept at room temperature during the whole procedure, we use the labels *hot* and *cold* in the photodiode just to distinguish the two measurements.

An important difference with respect to the previous measurement is that in this case only one measurement of the cold quantum efficiency is done, being the other one a reference measurement of the hot quantum efficiency. Hence, no average will appear in the final expression for the QE.

Figure 2.10: PMT inside the supporting structure after extraction from liquid argon bath.

The intensity in the PMT, I_{PMT}, will be given by:

$$I^{hot}_{PMT} = N_r \cdot (1-\alpha) \cdot QE^{hot}_{PMT} \tag{2.5}$$

Combining both equations:

$$\frac{I^{hot}_{PMT}}{(1-\alpha) \cdot QE^{hot}_{PMT}} = \frac{I^{hot}_{PD}}{\alpha \cdot QE_{PD}} \tag{2.6}$$

Once the spectral response is measured at room temperature, the cryostat is filled with LAr. The time needed for the PMT and the sustaining structure to cool down and stop boiling is about 1 hour. After that, the set of measurements is repeated and an analogous expression can be written:

$$\frac{I^{cold}_{PMT}}{(1-\alpha) \cdot QE^{cold}_{PMT}} = \frac{I^{cold}_{PD}}{\alpha \cdot QE_{PD}} \tag{2.7}$$

Assuming the fraction α and the photodiode quantum efficiency constant during the whole procedure, the combination of equations 2.6 and 2.7 provides the following expression for the QE at LAr temperature:

$$QE^{cold}_{PMT} = QE^{hot}_{PMT} \cdot \frac{I^{hot}_{PD} \cdot I^{cold}_{PMT}}{I^{cold}_{PD} \cdot I^{hot}_{PMT}} \tag{2.8}$$

Since measurements of QE^{cold} are correlated to those at room temperature, errors have to be properly propagated, which will make errors in cold to be larger than those for room temperature measurement.

In this case, the measurement sequence is as follows: We place the photodiode in a light-tight box with one of the ends of the optical fiber pointing on it, and the PMT on the empty dewar, with the other end of the optical fiber on it. High voltage is applied to the PMT and the lamp is turned on, and a first measurement is performed (following the procedure for the room temperature measurement). When the measurements for all the wavelengths are finished, the lamps and the high voltage are turned off and the cryostat is filled with liquid argon. Special care must be put on not moving the optical fiber during this operation. The PMT must be left for some time in the liquid argon bath until all the components reach liquid argon temperature and the argon stops boiling. Then high voltage is supplied again and the lamp is switched on and a new set of measurements is performed. With these two sets of measurements and using equation 2.8 it is possible to compute the quantum efficiency at liquid argon temperature.

Figure 2.11 shows the QE results obtained for the tested PMTs. For what concerns dark matter searches with a 1 tonne detector, quantum efficiencies around 20% guarantee for typical yields in photon counting experiments, about 1 photoelectron per keV of deposited energy. This is enough to identify signals down to true recoil energies of 20 to 30 keV.

As compared to room temperature, a shift of the peak towards shorter wavelengths and an increase of the absolute QE at the maximum is observed in all cases. This effect is clearly visible in figure 2.12, where the relative change from room to cryogenic temperature $\left[100 \cdot \left(1 - \frac{QE_{cold}}{QE_{hot}}\right)\right]$ is shown.

This behaviour [47, 57, 58] is related to the photoemission process [46] that takes place whenever a photon hits the photocathode of a PMT, usually a semiconductor (*bialkali* in the two tested models). When this happens, an electron is excited to the conduction band. The emission process is not a surface effect, but a bulk one. Hence, the electron must go through the semiconductor crystal until it reaches the vacuum, losing energy in each collision. If the electron reaches the crystal surface with sufficient energy to escape over the potential barrier, it will be emitted from the photocathode. When temperature decreases, the yield from the photocathode increases in the region far from the cutoff wavelength, due to a decrease of the energy loss of the electron in the lattice. In the region close to the cutoff wavelength, above which the photoelectric process is not anymore feasible, the yield decreases because of a decrease in occupied defect levels above the valence band, an increase in band gap, and probably an unfavorable change in band bending.

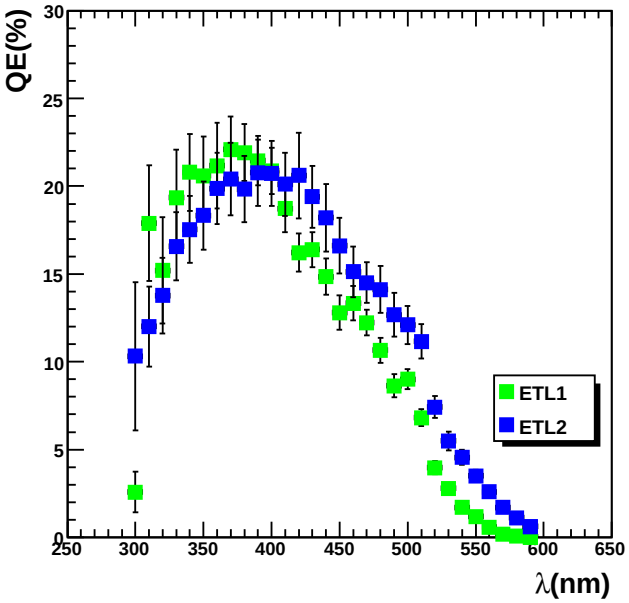

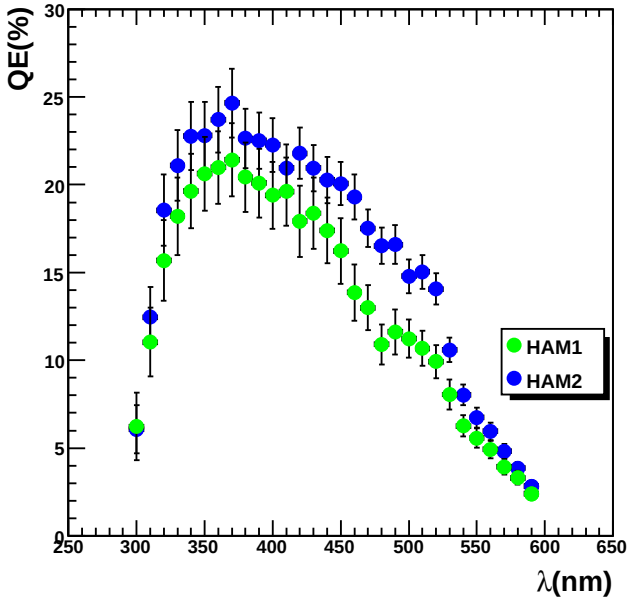

Figure 2.11: Quantum efficiency of the ETL (left) and Hamamatsu (right) PMTs as measured at cryogenic temperature.

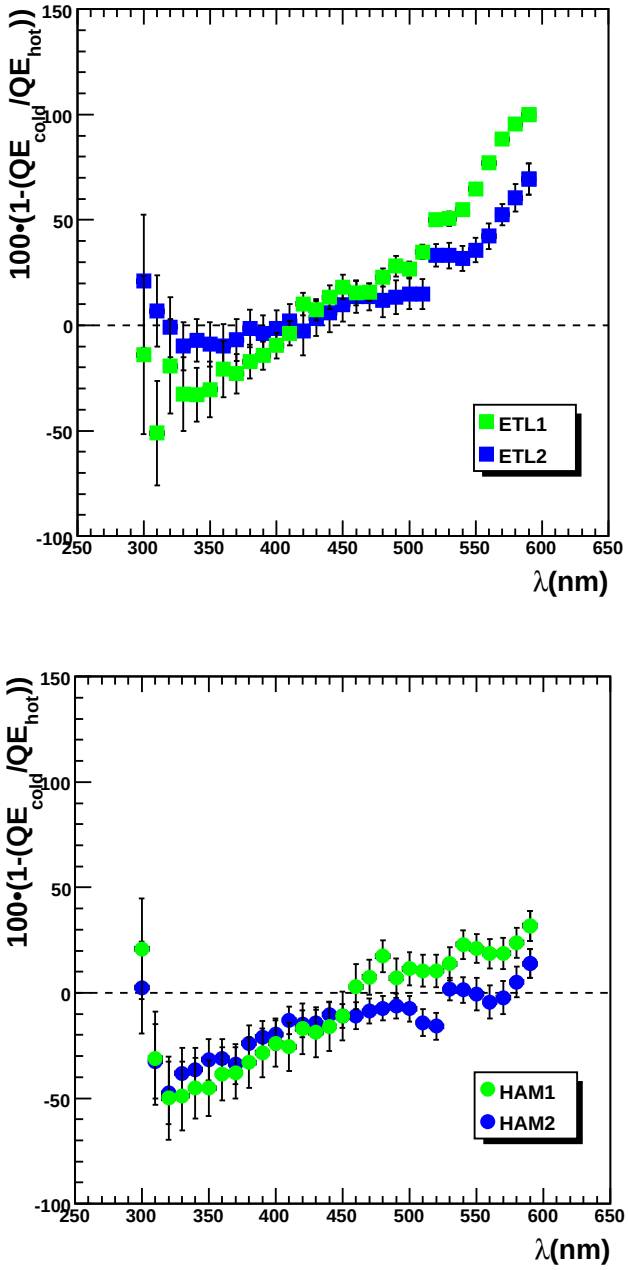

Figure 2.12: Change in quantum efficiency between room and cryogenic temperature for ETL (left) and Hamamatsu (right) models.

2.5.2 Response to single photoelectrons (SER)

In the previous section we have established one of the most important properties of the photocathode of our PMTs. In this section we will explore those properties of the PMT related to the multiplication process. The first difference with the measurements previously done is that before no multiplication was produced, and the high voltage was set only in the first dynode. Now we will apply high voltage to the whole dynode chain through a custom designed voltage divider. The second difference is the used illumination, which will now be by fast pulses composed from 1 to few hundreds of photons. With these levels of light, similar to those obtained in real experiments, we will study the response to single photons, the dark counts and the linearity of the PMT.

Experimental setup

The setup used for single electron response, dark counts and linearity measurements is shown in figure 2.13. The PMT is housed inside a light-tight cryostat which can be filled with liquid argon. The measurements were sequentially done first at room temperature and then in a LAr bath. The plots shown in this section only refer to results at cryogenic temperature, although some comments on comparisons with room temperature measurements are also included.

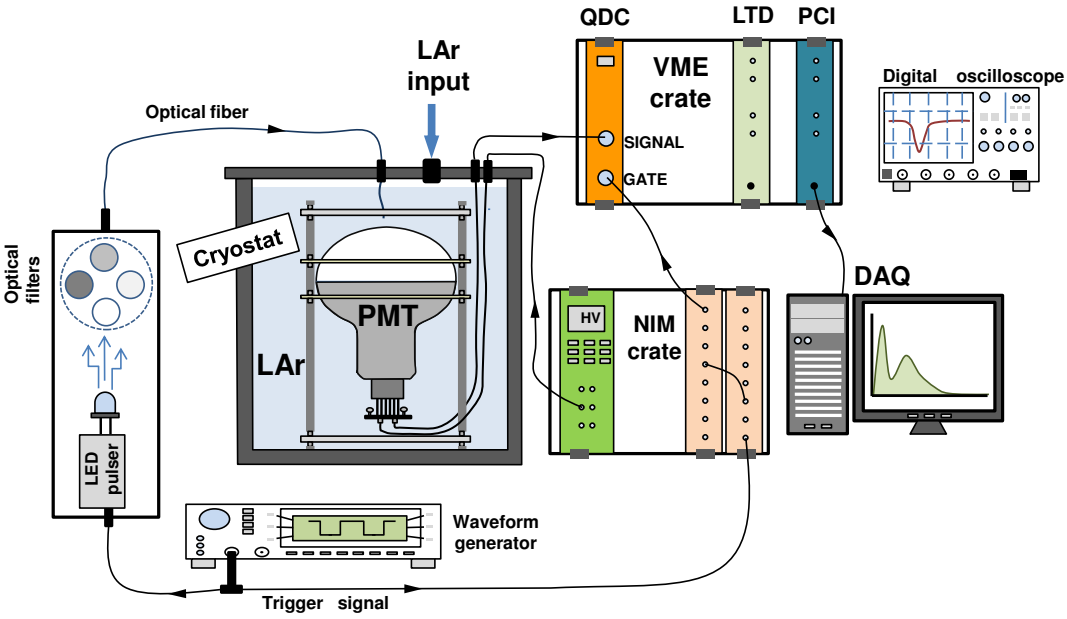

Figure 2.13: Setup for gain, dark counts and linearity measurements.

We use a standard LED with peak emission at 420 nm as light source and connect it to a pulser which provides 1 kHz frequency, few nanoseconds width light shots. If required, the light intensity can be attenuated by a set of neutral density filters. The light is sent to the PMT photocathode inside the cryostat thanks to an optical fiber. The PMT is biased with a NIM power supply (CAEN N470 [59]) and the signal transmitted through a standard LEMO cable. Depending on

the measurement to be done, the signal is analyzed with a Charge-to-Digital Converter (QDC CAEN V965A), an oscilloscope (LeCroy Waverunner 6100) or a Low Threshold Discriminator (LTD CAEN V814B) plus a Scaler (CAEN V560AE).

Gain

To measure the PMT gain, the amount of light reaching the photocathode must be reduced to the level of few photons. Ideally, our goal is to illuminate the PMT window with 1-photon pulses and measure the number of electrons produced, which is by definition the gain of the PMT. The number of photoelectrons that are produced in the photocathode follows a Poisson distribution and the probability of having r photoelectrons is expressed as:

$$P(r) = \mu^r \cdot \frac{e^{-\mu}}{r!} \tag{2.9}$$

The single photoelectron illumination level can be achieved by imposing that most of the signals come from single electron events i.e., by requiring the number of signals with two photoelectrons being below, for instance, 10% of that of single photoelectron. Using equation 2.9, the previous condition translates into $\mu = 0.2$ and $P(0) = 81.9\%$. Hence, if the light intensity is adjusted such that the number of empty triggers is 81.9% then the number of 2 photoelectrons signals will be one-tenth of that for 1 photoelectron. Under this condition, for any other number of photoelectrons the probability will be negligible. In practice, we will consider the contribution of 1 and 2 photoelectrons.

This illumination level can be set by selecting a noise level above which are most of the signals and below which is most of the noise. Then, a LED is pulsed and signals are observed in coincidence with the pulse trigger. One establishes a light level in which most triggers do not produce signals, and then counts, by means of an oscilloscope or any other device, the fraction of empty triggers. The LED voltage is then modified until the required illumination level is reached. Once this is achieved, the charge produced in every event is collected with a QDC and a distribution is obtained, from which we will compute the value of the gain.

Figure 2.14 shows an example of the collected charge spectrum under these conditions (SER) as obtained for ETL1 at 1350 V. The SER distribution has been fitted to a function which contains the following terms [47, 60]:

- An exponential distribution that fits the *pedestal steep fall* and which is caused by several factors: the continuous component of the dark current, the intrinsic shift of the QDC, the electronic noise affecting the measurement, etc. This exponential is parametrized as $e^{p_0+p_1\cdot x}$.
- A gaussian distribution which takes into account the response of the PMT to a single photoelectron (parameters A_1, μ_1 and σ_1).
- An extra gaussian with parameters $A_2, \mu_2 = 2 \cdot \mu_1$ and $\sigma_2 = \sqrt{2} \cdot \sigma_1$ to account for events with 2 photoelectrons. In general, a sum of n Gaussians can be included to reproduce n-photoelectron contributions.

Note that the left peak in figure 2.14, the pedestal, is not completely fit by this function. Only the final steep fall is reproduced by the considered function.

The gain is obtained from the position of the single photoelectron peak in the charge spectrum. Figure 2.15 shows the gain dependence on High Voltage (HV) for the four tested PMTs in cold. A clean exponential behaviour is observed in all cases (note the logarithmic scale). The Hamamatsu tubes achieve the nominal 10^7 gain at about 1100 V whereas the ETL tubes need higher voltages.

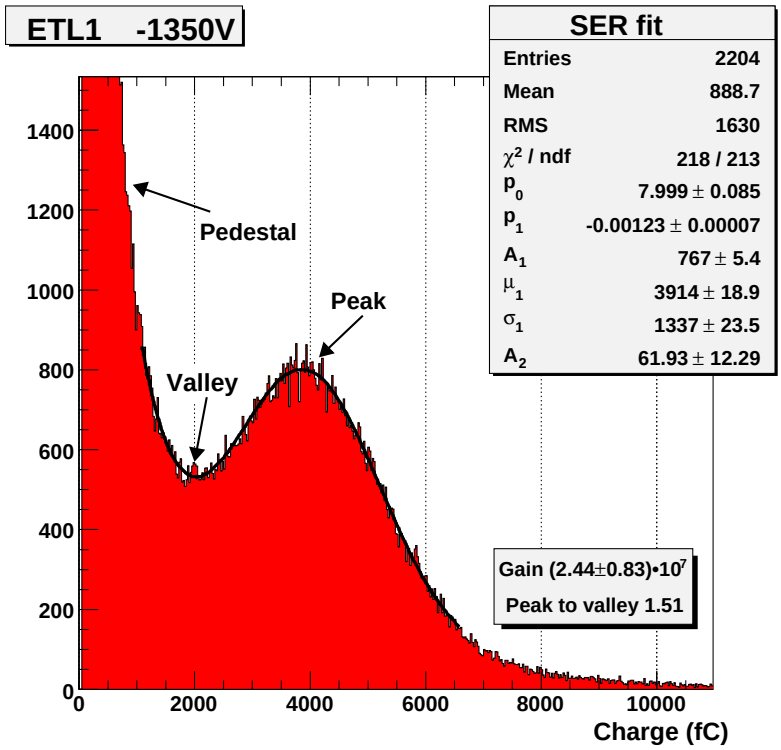

Figure 2.14: Example of a SER spectrum as obtained for the ETL1 at 1350 V. The meaning of the output fit parameters is given in the text.

On the other hand, the slope for ETL PMTs is steeper. It is interesting to notice that similar values and slopes were measured at room temperature. This uniformity on the results can be attributed to the stability of the cryogenic electronic components mounted on the PMT base.

Peak to Valley ratio and SER resolution

The ratio between the height of the single photoelectron peak and the valley (P/V), obtained from the charge spectrum (see figure 2.14) is another important characteristic to be measured. Figure 2.16 shows the results obtained on this quantity as a function of the gain.

The peak to valley ratio increases with gain in all cases. For a gain of 10^7 the measured value is around 2.5 for all PMTs but the ETL1, which shows a lower value. Beyond this point, the ETL tubes show an almost flat P/V while the Hamamatsu ones increase with voltage.

Figure 2.17 shows the resolution in the SER peak, defined as the ratio $\frac{\sigma_1}{\mu_1}$ in percentage. While the ETL tubes exhibit an almost flat dependence on the considered range, the resolution decreases smoothly on the Hamamatsu PMTs as gain is increased. At the nominal value of 10^7 the four tubes show resolution values in the range 35–40%.

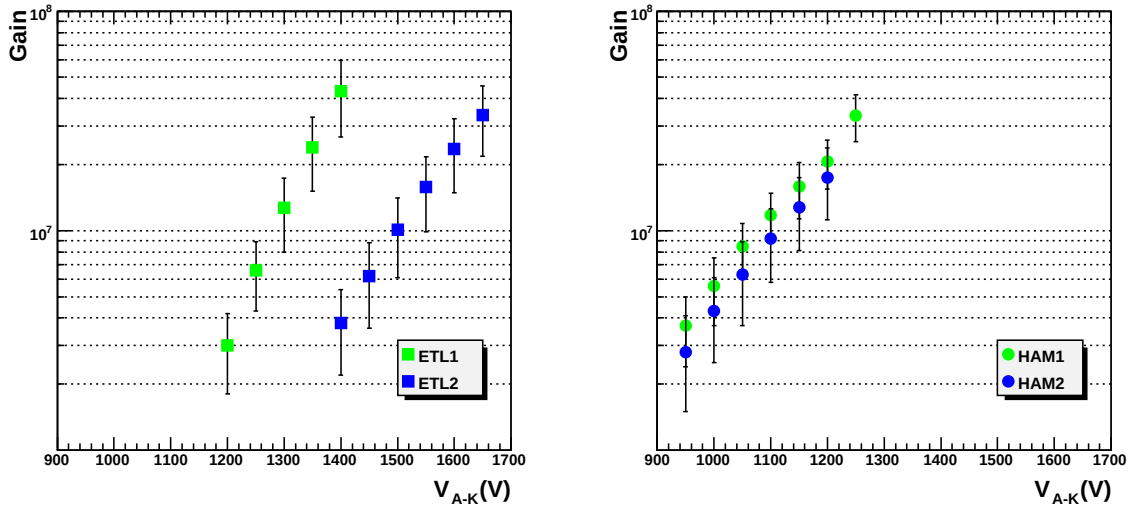

Figure 2.15: Gain dependence on HV for the four photomultipliers as measured in LAr.

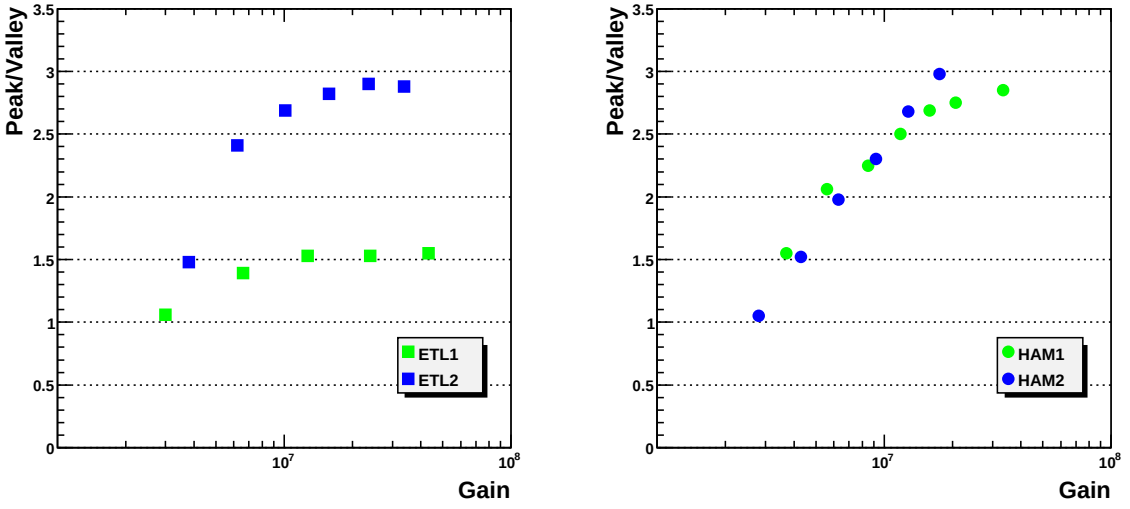

Figure 2.16: Peak to valley ratio dependence with gain at LAr temperature.

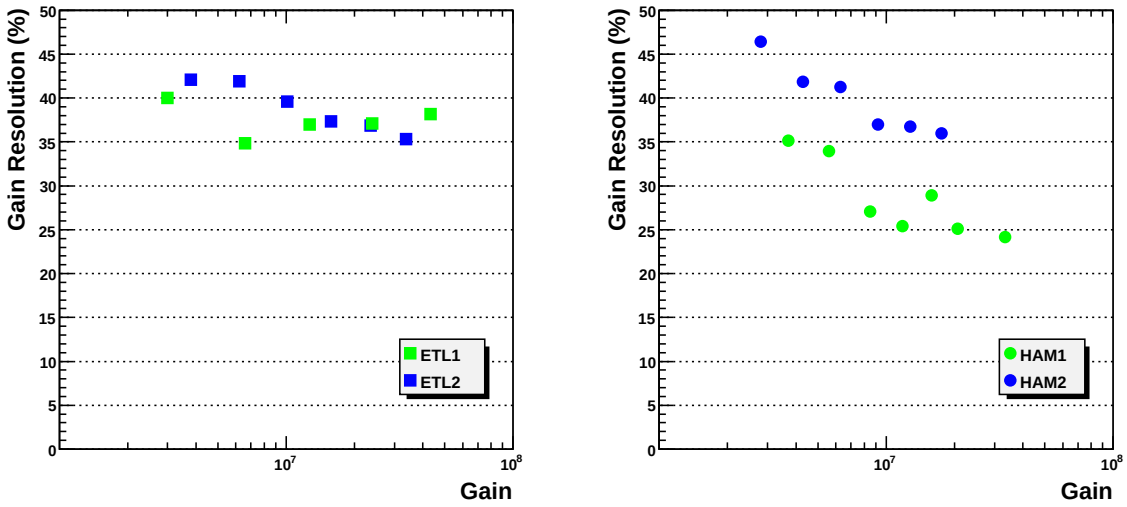

Figure 2.17: Gain resolution from SER spectrum for the tested PMTs at LAr temperature.

2.5.3 Dark Counts

Before measuring the dark count frequency, the phototubes are placed in darkness, inside the container filled with LAr and connected to the HV for several hours. This must be done because when the PMT is illuminated by environment light, electrons on the photocathode are excited to energies higher than the thermal one, and one must wait for de-excitation before the normal operation. This can be seen in figure 2.18. When the current in the photocathode is shown as a function of time for a PMT just put in a dark environment. We see a fast decrease at the beginning, that then stabilizes to a fixed value, that is not related to this process and is due to a leak current between the pins in the photocathode.

The PMT output is then connected to the discriminator and the output signal is feed to a scaler (CAEN V560AE), where the number of pulses above a given threshold is counted. As an example, figure 2.19 shows the result for HAM1 biased at 1050 V.

To compare different PMTs at different voltages, thresholds in the discriminator (mV) have to be expressed in terms of number of photoelectrons in amplitude. The SER peak voltage is obtained from recorded oscilloscope signals taken at very low intensity illumination conditions, just as explained in the gain measurement section. Looking at figure 2.19, the abrupt fall (factor 100) at low thresholds, corresponding to the level of single photoelectron, is clear. Beyond this point, the decrease in rate when increasing the threshold is smooth.

Figure 2.20 shows the number of dark counts for different values of gain above 4 photoelectrons for every PMT. This threshold has been selected as it is far from the abrupt fall region but it is still low enough to be used as a trigger.

As expected, the dark count rates increase with gain (higher voltages). Frequencies in the range 50–100 Hz are obtained for gain values around 10^7.

Compared to the results at room temperature, a clear decrease in the rates is measured *in cold*: a factor close to 5 and 2 for the ETL and Hamamatsu tubes, respectively. This effect is explained by the decrease of the thermal energy of the electrons in the photocathode.

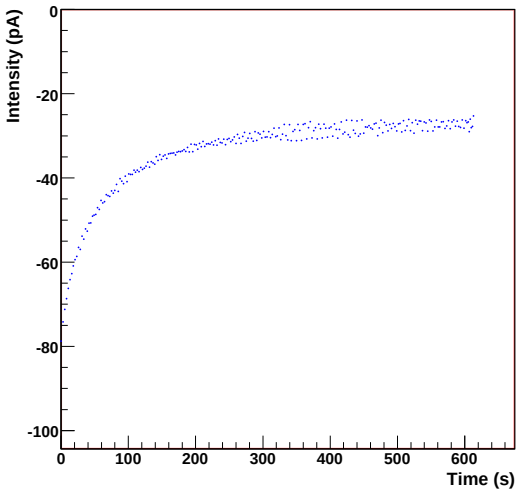

Figure 2.18: Dark current decrease with time after placement of the PMT in darkness.

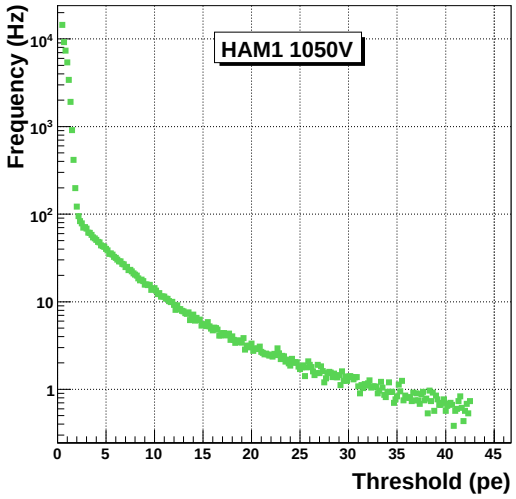

Figure 2.19: Dark counts rate dependence on discriminator threshold for HAM1 at 1050 V.

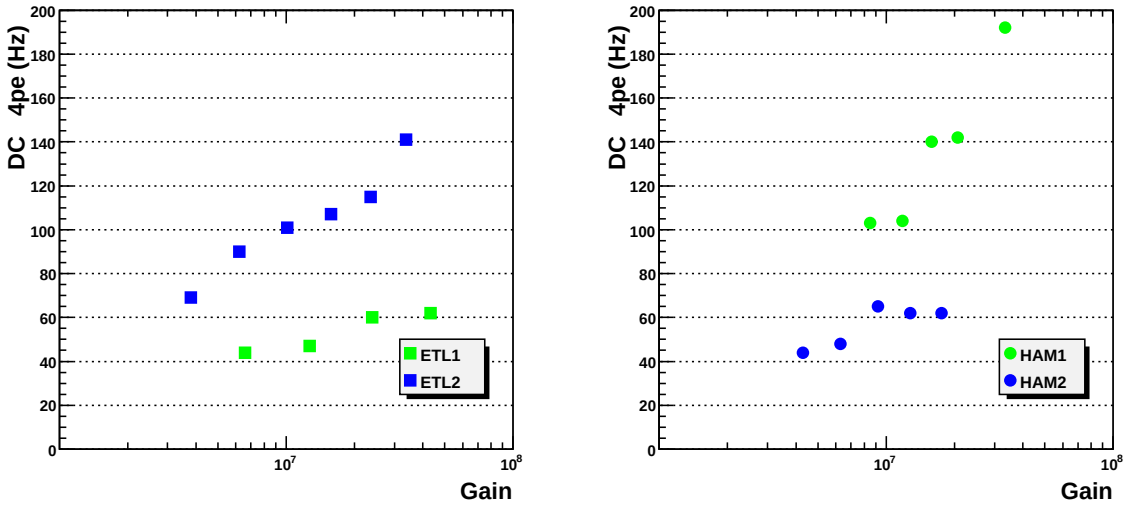

Figure 2.20: Dark counts rates as measured in LAr (4 pe threshold).

2.5.4 Linearity

The study of the PMT response to different illumination levels above the single photoelectron was carried out using neutral density filters [60]. They were placed in a rotating support, just between the light source (pulsed blue LED) and the optical fibre light guide (see figure 2.13). Five filters were used (optical density values d = 3.0, 2.0, 1.5, 0.5 and 0.3) which allowed variations of the light intensity brought to the photocathode by three orders of magnitude (attenuation factor = 10^d).

The measurement proceeds as follows: the PMT voltage is adjusted to a gain of 10^7 and maintained unchanged. The higher optical density filter is selected. The LED intensity will be fixed during the whole measurement, and it has to be set to a value such that our electronics will not saturate for the 0.3 filter. As there is a factor 500 of difference and our electronics saturates at 800 pC, we should set an illumination level of the order of 1 photoelectron. Hence, the average number of photoelectrons in the PMT is fixed between one and two. Then, a PMT charge spectrum is recorded with each filter and analyzed.

Figure 2.21 shows the kind of spectrum obtained by this method. If the parameters of the Gaussian for one photoelectron are μ_1 and σ_1, the parameters of the distribution for the coincidence of n photoelectrons are given by the sum of the corresponding Gaussians, i.e. $\mu_n = n \cdot \mu_1$ and $\sigma_n = \sqrt{n} \cdot \sigma_1$. The average number of photons can be then computed as $\frac{\Sigma i \cdot N(i)}{\mu_1 \cdot \Sigma N(i)}$, where $N(i)$ is the content of the i-th bin of the charge distribution. For the measurement shown in figure 2.21, a value close to 2.3 is obtained. Dotted lines correspond to the first five Gaussians whereas the convolution (solid line) nicely follows the global data. The leftmost peak corresponds to the pedestal (empty trigger events).

In order to complete the linearity measurements, charge spectra with all neutral density filters are acquired. For high photocathode illumination levels it is not possible to resolve peaks for different number of photoelectrons anymore and there are no empty trigger events. This requires a prior measurement of the pedestal, which is achieved by measuring without voltage supply on

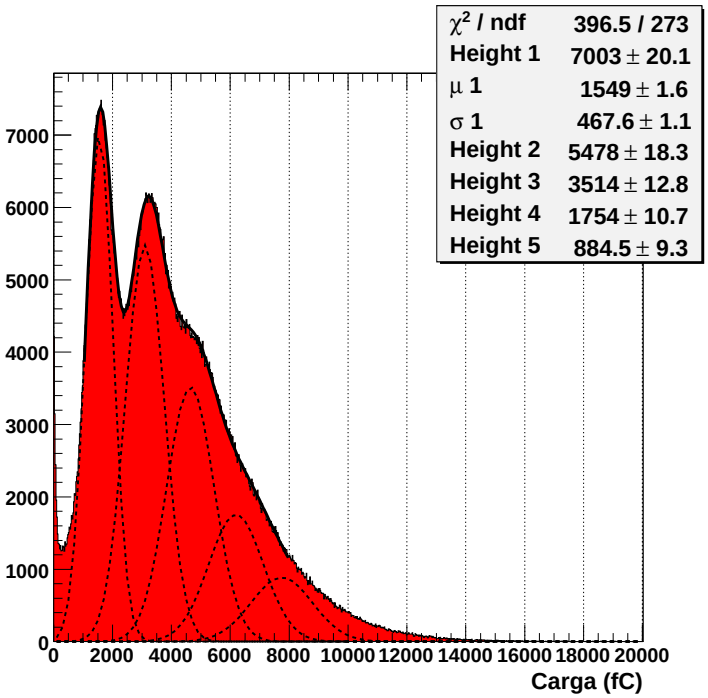

Figure 2.21: Example of charge spectrum (ETL2) obtained, along the linearity measurements, with the 3.0 optical density filter. Dotted lines (solid line) correspond to individual Gaussian fits (global fit).

the LED. In practice, in our setup it is only possible to resolve single peaks with the biggest density filter. Figure 2.22 shows the result obtained for one of the PMTs with a 2.0 optical density filter. The ratio between the average charge in the distribution after pedestal subtraction and the charge of a single photoelectron (from the d=3.0 filter measurement) gives the mean number of photoelectrons.

For every measurement we can give a value of the ideal number of photoelectrons as the measured with the 3.0 optical density filter times the factor corresponding to the difference in optical densities, i.e.:

$$N = N_3 \times \frac{10^{-d}}{10^{-3}} \tag{2.10}$$

A comparison between the ideal number of photoelectrons and the measured one is shown in figure 2.23.

The four PMTs show a nice linear behaviour up to 100 pe. Above this value a slight departure from linearity is clearly seen. The luminosities in which the PMTs show linear behaviour are of the same magnitude than those that typically appear in low energy events where the photon counting technique is used.

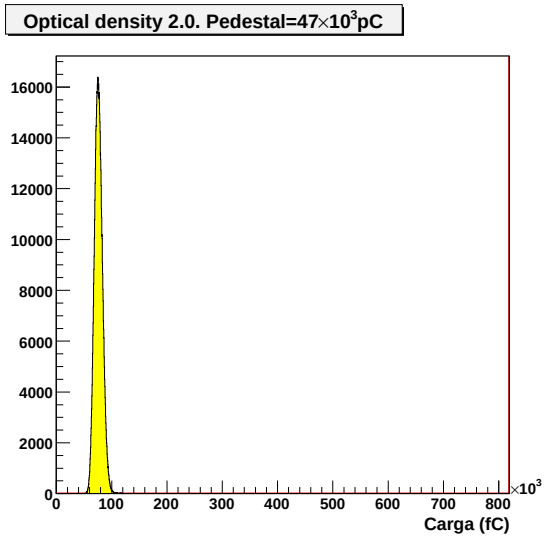

Figure 2.22: Example of charge spectrum (HAM1) obtained, during the linearity measurements, with the 2.0 optical density filter. No individual gaussians can be resolved

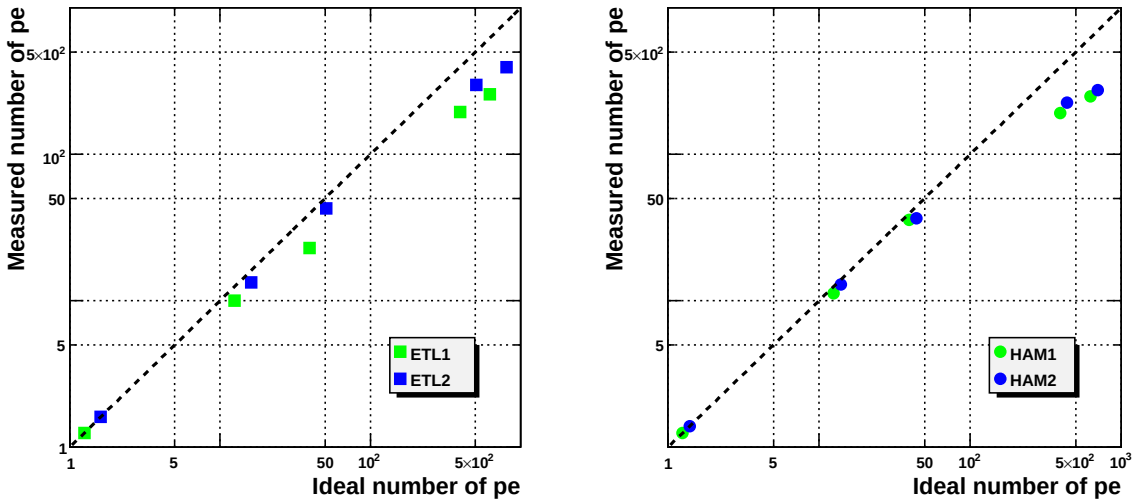

Figure 2.23: Linearity measurements: PMT signal in units of number of photoelectrons as function of the ideal one as measured in liquid argon. The dotted line shows an ideal 1:1 linearity behaviour.

2.6 Conclusions

In this chapter we have analyzed whether large-area phototubes are suitable for operation at cryogenic temperatures and fulfil the stringent physics requirements imposed by future dark matter experiments. Only two companies are able, nowadays, to provide PMTs capable of operating at temperatures in the vicinity of hundred kelvins or lower. We have extensively tested 8" phototubes from ETL (9357 KFLB) and Hamamatsu (R-5912-MOD) both at room and liquid argon temperatures. Our conclusion is that both models are adequate for installation in an liquid argon dark matter experiment, since they have QE above 20% for 400 nm,thus guaranteeing light yields of around 1 pe/keV, enough to detect signals depositing around 20 to 30 keV. They show a linear behaviour throughout the energy window where we expect to have better chances to detect dark matter. In addition, their timing accuracy is such that they will allow to distinguish fast from slow scintillation light components, thus providing a powerful rejection tool against background.

Finally, we summarize the most relevant phototube features found at cryogenic temperatures:

- An increase of the maximum values of the quantum efficiencies up to 25% together with a global shift of the distributions towards shorter wavelengths is observed as compared with results at room temperature. ETL models appear to have higher peak values
- A gain of 10^7 is reached for both models, with polarization voltages between 1100 and 1500V, being the lowest values for the Hamamatsu PMTs.
- The dark count rate at 4 photoelectron threshold has a frequency of about 100 Hz, similar for both models.
- A good linear behaviour is achieved even at very high illumination levels, up to $\sim$100 photoelectrons.

Chapter 3

Dark Matter Searches and the ArDM experiment

In the last years, advances in astrophysical and cosmological measurements have unambiguously shown the existence of an unknown form of matter that has been called *dark matter* (DM). At the same time, advances in particle physics have led to predictions of new physics beyond the standard model, and most of the proposed extensions of this model predict a particle that could be a candidate to explain the dark matter content of the universe. Hence, a great effort is now being devoted to find some evidence of these new particles.

Direct dark matter search experiments look for an excess of signals in an underground, low background environment. Very different detectors have been built for this purpose, having in common the capability to measure small energy depositions ($\sim$1-100 keV). From all of the proposed media, liquefied noble gases are a very promising alternative, as the possibility to measure charge and light simultaneously allows an enhanced signal to background discrimination. Moreover, they have some other advantages, as the relative high temperature at which they work compared to that of bolometers, or the cost, which make feasible to go to much higher masses than for other kind of detectors.

In this chapter we will present the most important aspects of dark matter and we will describe the ArDM experiment. After this we will explain the surface tests that are being carried out to assess the most relevant working principles of the detector prior to underground installation.

3.1 Dark Matter

The hypothesis of the existence of dark matter was first proposed by Zwicky in 1933. He realized that by applying the virial theorem, which relates the average kinetic energy of a system to its average total potential energy, to the Coma Cluster of galaxies, the predicted mass was bigger than the observed one. When comparing the cluster mass estimated from the motion of the galaxies in its edges with that based on the number of galaxies and its luminosity, he found a difference of a factor ~ 400. Since the gravity of the visible galaxies was too small for the observed orbits, he concluded that there was some kind of non-visible matter which would hold the cluster together.

Since then, a lot of astrophysical and cosmological evidences have been accumulated showing that the observed masses do not match with those inferred from dynamical arguments. Among the most relevant ones we can point out the following [61]:

- Rotational curves of galaxies. 40 years after Zwicky's discovery, these were the first observations to show an anomalous mass distribution. Measuring the velocity curve of edge-on spiral galaxies, it was shown that most of the stars orbit at the same speed, which implies a uniform mass distribution beyond the galactic bulge. This result implies the existence of a galactic halo that contains most of the galaxy mass. Other observations suggest that this halo extends up to ten times the visible size of a galaxy [62].

- Gravitational lensing. General gravity predicts that whenever the light passes nearby a massive object, its trajectory will be bent. Hence, if a massive body is between an observer and the object he is observing, it will bend the light producing multiple images of the observed body. Through the geometrical distortion it is possible to obtain the mass distribution of the massive object. The importance of this measurement relies on the fact that it is independent of the dynamics and predicts similar mass distributions. There is another technique based on the same effect, known as weak lensing, that instead of single observations considers vast galactic surveys to look for small distortions through statistical analyses.

- WMAP Data. Measurements of the microwave background radiation performed by the WMAP satellite together with the Sloan Digital Sky Survey [63, 64] large-scale structure data show that only a small fraction of the matter content of the universe is of baryonic origin ($\Omega_B = 0.042 \pm 0.002$), while the rest is made of a totally unknown new form of matter ($\Omega_{DM} = 0.20 \pm 0.02$). The rest of the energy content of the universe is accounted for advocating a very smooth form of energy called dark energy ($\Omega_\Lambda = 0.76 \pm 0.02$)[1].

- Bullet Cluster. Optical and X-ray images of the bullet cluster (1E0657-558) [65, 66], obtained by the Chandra telescope. In this cluster the collision of two galaxies, that happened 150 million years ago, can be observed. By means of gravitational lensing, a map of the matter in the collision region can be obtained, and it is possible to see clearly that while the hot gases that interacted during the collision, remained close to the center, there is a massive component that did not interact and is further from the center.

There are two obvious possible explanations to all these facts: either the measured amount of mass is much bigger than the observable one, or the dynamics used to compute masses is wrong. Since the decade of 1980 a new kind of theories called MOND (Modified Newtonian Dynamics) have attempted to explain all the observed phenomena through a modification of Newton's second law of dynamics for small accelerations [67]. However, up to this moment none of these theories have succeeded to explain the whole set of phenomena. The only possible solution then is to accept that $\sim 95\%$ of the composition of the universe is unknown.

So far dark matter has only been observed through its gravitational effects. Hence we know nothing about its nature and fundamental properties. A convincing case seems to exist for non-baryonic dark matter. Elementary particles, often arising for yet undiscovered but well motivated physics, dominate the field [68]. The dark matter density in the neighborhood of our solar system is expected to be $\rho_{DM} \sim 0.3$ GeV·cm^{-3}, although this varies in some halo models. We will discuss now some of the candidate particles.

Standard model neutrinos are known to be massive. A lower limit on their mass square difference stems from the observation of neutrino oscillations in atmospheric neutrino data:

$$\Delta m^2_{23} \sim 3 \times 10^{-3}\, eV^2 \tag{3.1}$$

[1] $\Omega_x = \rho_x/\rho_c$, where ρ_x is the density of x and ρ_c is the critical density for a flat universe.

which when combined with solar neutrino oscillation data implies that the most massive neutrino must have a mass $\geq$ 0.05 eV. The contribution of neutrinos to the universe follows the relation:

$$\Omega_\nu h^2 = \sum_{i=1}^{3} \frac{g_i m_i}{90\, eV} \tag{3.2}$$

where $g_i = 1$ for Majorana neutrinos and $g_i = 2$ for Dirac neutrinos, which suggests a minimum contribution to the universe composition (for a Majorana neutrino) of $\Omega^2_{\nu h} \geq 0.0006$. So standard model neutrinos are DM. However, they are hot. An excess of relativistic particles during the epoch of galaxy formation would wash out small scale structure, preventing agreement with the matter density distribution observed today. A combination of galaxy clustering measurements, CMB and observations of Lyman-α forest gives an upper limit on light neutrino combination of [69]:

$$\Omega_\nu h^2 < 0.0076 \,(\text{at } 95\%\text{C.L.}) \tag{3.3}$$

This limit applies to all forms of hot dark matter. Our main concern therefore focuses on cold dark matter candidates only, since they must form the dominant matter component.

Clearly candidates for cold dark matter must satisfy several conditions:

- Interact very weakly, or not at all, with electromagnetic radiation.
- Have a cosmologically interesting (preferably dominant) relic density.
- Be stable on time scales comparable with the age of the universe (otherwise they would have decayed).

A strongly favored candidate for cold dark matter is the WIMP (Weak Interacting Massive Particle), with a mass $\sim 10\,\text{GeV}-$few TeV, with interaction cross section of the order of the weak scale. Their relic density can be calculated reliably if the WIMPs were in thermal equilibrium with the other standard model particles in the early stages ($< 1\,\text{ns}$) following the Big Bang. As the temperature, T, of the universe cools, the density of the more massive particles with masses $m_\chi > T$ will become exponentially (Boltzmann) suppressed. When the expansion rate of the universe, H, exceeds the particle annihilation/creation rate, the WIMPs drop out of thermal equilibrium, and the number density (for a comoving volume) becomes frozen. The present relic density is then approximately given by [61]:

$$\Omega_\chi h^2 \simeq \frac{T_0^3}{M_{Pl}\langle\sigma_a v\rangle} \simeq \frac{0.1 pb \cdot c}{\langle\sigma_a v\rangle} \tag{3.4}$$

Here σ_a is the total annihilation cross section of the WIMPs, v is the relative velocity between WIMPs, and $\langle ...\rangle$ represents an average over the thermal distribution of WIMP velocities; T_0 is the equilibrium temperature, M_{Pl} is the Planck mass and c is the speed of light. The freeze out occurs at a temperature $T \simeq m_\chi/20$, where m_χ is the WIMP mass, almost independent of the properties of the WIMP, so they are already non relativistic when they decouple. A cosmologically interesting density arises from an annihilation cross section of the order of the electroweak scale interaction. This last coincidence, which is not tuned, but comes directly from reliable calculations, represents one of the main motivations for believing that WIMPs could provide the dominant contribution to the matter in the universe. It is also important to note that smaller annihilation cross sections correspond to larger relic densities. WIMPs with stronger interactions remain in equilibrium for longer and hence decouple when the universe is colder, and so they are suppressed by a smaller Boltzmann factor.

3.2 WIMP Interactions

All the dark matter experiments are based on the detection of nuclear recoils arising from collisions between WIMPs and target nuclei (argon in thew case of the ArDM experiment). The differential spectrum of such recoils is expected to be featureless and smoothly decreasing, with the typical form:

$$\frac{dR}{dE_R} = \frac{R_0}{E_0 r} e^{-E_R/E_0 r} \tag{3.5}$$

where E_R is the recoil energy, E_0 is the most probable incident kinetic energy of a dark matter particle of mass M_D, r is a kinematic factor, $r = 4M_D M_T/(M_D + M_T)^2$, for a target nuclei of mass M_T, R is the event rate per unit of mass and R_0 is the total event rate. Since galactic velocities are of the order 10^{-3}c, values of M_D in the 10−1000 GeV range would give typical recoil energies in the range 1−100 keV.

If we write the generic low energy elastic cross-section as [70]:

$$\sigma_0 \propto \left(\frac{g_D^2 g_N^2}{M_E^4} \right) \mu^2 \tag{3.6}$$

where g_D, g_N are the dimensionless coupling strengths to WIMP and nucleus, respectively, of a heavy exchanged particle of mass M_E, and as $\mu^2 = M_D M_T r/4$, one can write:

$$\frac{R_0}{r} \equiv 126 \left(\frac{\sigma_0}{1pb} \right) \left(\frac{1GeV\ c^{-2}}{\mu} \right)^2 \left(\frac{\rho_D}{0.4GeV\ c^{-2}\ cm^{-3}} \right) \left(\frac{v_0}{230\ km\ s^{-1}} \right) events/kg/day \propto \left(\frac{g_D^2 g_N^2}{M_E^4} \right) \mu^2 \tag{3.7}$$

which allows to relate the observed rate with the WIMP mass and the interaction cross-section.

The aim for all the experiments is to progressively reduce or reject background events to allow a spectrum of rare nuclear recoil events to be observed. Hence, underground operation is required to eliminate nuclear recoils from neutrons produced by cosmic ray muons.

When an experiment has set an upper limit to the differential rate at any particular value of E_R, the right hand of equation (3.5) allows a corresponding limit on R_0, the dark matter signal, to be calculated for each assumed value of particle mass. Since the galactic dark matter density and flux are approximately known, the limit on R_0 can be converted to a limit on the particle interaction cross section.

In practice, equation 3.5 is considerably more complicated owing to the following corrections:

1. The detector is located on the Earth in orbit around the Sun, with the solar system moving through the galaxy.

2. The detection efficiency for nuclear recoils will in general be different from that for the background electron recoils. Thus the “true recoil energy” will differ from the observed one by that relative factor.

3. The target may consist of more than one element, with separate limits resulting from each.

4. There are instrumental resolution and threshold effects, for example when photomultipliers are used to observe events yielding small numbers of photoelectrons.

5. The limits set will, in general, be different for spin-dependent and spin-independent interactions, the latter being, in addition, coherently enhanced in amplitude at low energies by the number of interaction target nuclei.

6. There is a form factor correction < 1 which is due to the finite size of the nucleus and dependent principally on nuclear radius and recoil energy. This also differs for spin-dependent and spin-independent interactions.

To take into account all these effects, equation 3.5 can be rewritten as:

$$\frac{dR}{dE_R}|_{observed} = R_0 S(E) F^2(E) I \tag{3.8}$$

where S is the modified spectral function taking in account the above factors, F is the form factor correction and I is an interaction function involving spin-independent and/or spin-dependent factors. Lets analyze all these three terms:

- S(E) is the so called spectral function and depends on the properties of the halo model considered for the dark matter. For practical purposes, it can be written as [70]:

$$S(E_R) = \frac{k_0}{k_1}\frac{1}{E_0 r}\left(c_1 e^{-c_2 E_R/E_0 r} - e^{-v_{esc}^2/V_0^2}\right)$$

  There is, however, one important fact not included in this equation. The Earth velocity changes as $v_E \approx 244 + 15 sin(2\pi y)$ km s^{-1}, where y is the elapsed time from (approximately) March 2nd in years. This modulation of $\sim 6\%$ in velocity gives rise to a modulation of $\sim 3\%$ in rate. So an experiment measuring at different seasons should measure different rates. Based on this effect the experiment DAMA claimed the observation of dark matter in their setup [71], although other direct-search experiments, probing similar regions of the parameter space, have found negative results [72, 73, 74, 33, 41]. Another related effect is the change in the nuclear recoil angle distribution along the year. However, due to the small energies, only gaseous experiments are sensitive to these parameters, and mass reached in such experiments are currently not enough for a positive detection.

- When the momentum transfer q $= \sqrt{2 M_T E_R}$ is such that the wavelength h/q is no longer comparable to the nuclear radius, the effective cross section begins to fall with increasing q, even for the spin dependent case, which effectively involves only a single nucleon. This is usually represented by a form factor F, which is a function of q and the "nuclear radius" $r_n = a_n A^{1/3} + b_n$. For most of the cases, it is sufficient to use the approximation $F^2 = e^{-\alpha (q r_n)^2}$, with $\alpha = 1/3$. We note that this quantity is 1 for the zero momentum transfer case.

- The I term depends on whether the interaction is spin dependent or spin independent. For interactions independent on spin and the same for neutrons than for protons, there will be A scattering amplitudes, that for low momentum transfer would add coherently. The rate would be given by that of 1 nucleon times the coherent interaction factor $I_C = A^2$. For the case of spin-dependent interactions, the amplitude changes sign with spin direction, so only unpaired nucleons contribute. Thus only nucleons with an odd number of protons and/or neutrons can feel this kind of interaction. In this case the interaction factor is given by $I_s = C^2 \lambda^2 J(J+1)$, where C is a factor related to the quark spin content of the nucleon and λ is related with the spin and angular momentum of the unpaired nucleon. More complicated forms of these factors can be found in different reports [75]. It is important to note that in order to be comparable, results from different experiments must be expressed in terms of nucleon cross section.

Type	Discrimination technique	Target Material	Experiments
Solid Scintillator	pulse shape discrimination	NaI, CaF_2	LIBRA/DAMA, NAIAD
Cryogenic	phonon/charge/light	Ge, Al_2O_3	CDMS, CRESST, EDELWEISS
Liquid noble gas	light, charge, pulse shape discrimination	LAr, LXe, LNe	ArDM, WARP, XENON, ZEPLIN, CLEAN
Bubble Chamber	super heated bubbles, droplets	C_3FI, C_4F_{10}	COUPP, PICASSO
Gas detector	ionization track resolved	CS_2	DRIFT

Table 3.1: Most common experimental techniques used for dark matter searches [76].

3.3 Liquid noble gases as detector media for dark matter searches

As already mentioned, dark matter searches have been one of the fields in experimental particle physics in which more effort has been put in the last years. Very different kinds of detectors have been proposed, having in common the possibility to detect events in a range of energy from ∼100 keV down to less than 1 keV. Table 3.1 shows some of the different techniques and target materials used, together with some of the experiments that have used them.

Among all these experimental techniques, liquid noble gases seem to be one of the most promising ones. Table 3.2 shows the most important properties of liquid noble gases. Between their relevant advantages, we can point out:

- These liquids are dense and homogeneous. This allows to construct large detector masses. This is crucial to explore lower cross section values. For example, we note that $\sigma \sim 10^{-46}\mathrm{cm}^2$ produces event rates of the order of 1 event/100kg/year.
- Ionization produces very good resolution in the position of events when the detector is operated as a TPC, which allows the possibility of fiducial volume cuts.
- Liquefied noble gases do not attach electrons, and electron mobilities are high for the heavier noble gases, which allows long drift distances (>1m), due to, as well, their easy purification.
- Noble gases are inert, not flammable, and very good dielectrics.
- They are bright scintillators, with light yields comparable to that of NaI (∼40 photons/keV).
- Discrimination between nuclear and electron recoils are readily achieved thanks to pulse shape discrimination (not for xenon) and differences in the ionization to scintillation ratio.

The choice of natural argon for a ton-scale target instead of other noble gases, as xenon, which is the target for several running experiments, can be motivated by the following arguments:

- The detection energy threshold depends on the achievable performance of the light and ionization detection systems. The event rate in argon is less sensitive to the threshold on the recoil energy than for xenon because of the form factors. For a threshold of $\simeq 30\,\mathrm{keVr}^2$,

[2]keVr means keV of true recoil energy of the nucleus

	Z(A)	Boiling Point at 1 atm (K)	Liquid density at $T_b(g/cc)$	Ionization (e^-/keV)	Scintillation (photons/keV)	Scintillation wavelength(nm)	Triplet Molecule lifetime (μs)
He	2(4)	4.2	0.13	39	22	80	13×10^6
Ne	10(20)	27.1	1.21	46	30	78	15
Ar	18(40)	87.3	1.40	42	40	128	1.6
Kr	36(84)	119.8	2.41	49	25	150	0.09
Xe	54(131)	165.0	3.06	64	46	175	0.03

Table 3.2: Liquid noble gases properties [77].

the rates per mass on xenon and argon are similar. With such a threshold, a WIMP-nucleon cross-section of 10^{-44} cm^2 yields about one event per day per tonne.

- The decay time of the slow component of the scintillation light is 1.6 μs in clean liquid argon, which is much longer that that of the prompt emission (∼few ns), allowing the use of pulse shape discrimination, while in liquid xenon both times are similar (of the order of few to tens of ns) and this technique does not provide a good rejection power.

- Argon is much cheaper than other noble gases, and there is a sizable experience in the handling of massive liquid argon detectors (see for example the ICARUS program [31]). A ton-scale argon detector is really conceivable, safe and economically affordable.

- The scientific relevance of obtaining data on argon and xenon is given by the fact that recoil spectra in xenon and argon are different due to kinematics, providing an important cross check in the case of a positive signal.

Hence, liquefied noble gases and explicitly liquid argon, can meet the requirements of a dark matter search experiment providing both scalability and an efficient background rejection power.

3.4 The ArDM Detector

The ArDM (Argon Dark Matter) experiment is a direct dark matter search experiment using liquid argon as target medium [78]. The detector is contained in a cylindrical vessel where the liquid and the vapour of the argon are in equilibrium. The active volume is embedded in a high strength electric field ($1-5$ kV/cm). The high electric field helps reducing the recombination of the ionization electrons, even in the case of highly quenched slow nuclear recoils. A schematic of the detector is shown in figure 3.1. The main properties are summarized in table 3.3.

At the bottom of the drift region a light transparent cathode is set at a high voltage ($100-500$ kV). A series of electrodes are installed and biased along the full drift path to keep the field uniform at a level of few %. Such high voltage in the detector is provided by a cascade of rectifier cells (Greinacher/Cockroft-Walton circuit) which takes as input an alternate voltage of amplitude V_0 and gives an output continuous and with value $2 \cdot V_0 \cdot N$, where N is the number of stages. This whole circuit is immersed in the liquid argon, exploiting its great insulation capability.

The ionization electrons are drifted to the liquid-vapour interface and are extracted into the gas phase. In the vapour a large electron multiplier (LEM) is installed to provide electron amplification by means of a high field generated in small (cylindrical shaped) holes (see figure 3.2). The LEM is composed by a 1.5 mm thick plate of isolating material, usually vetronite, which is covered by a

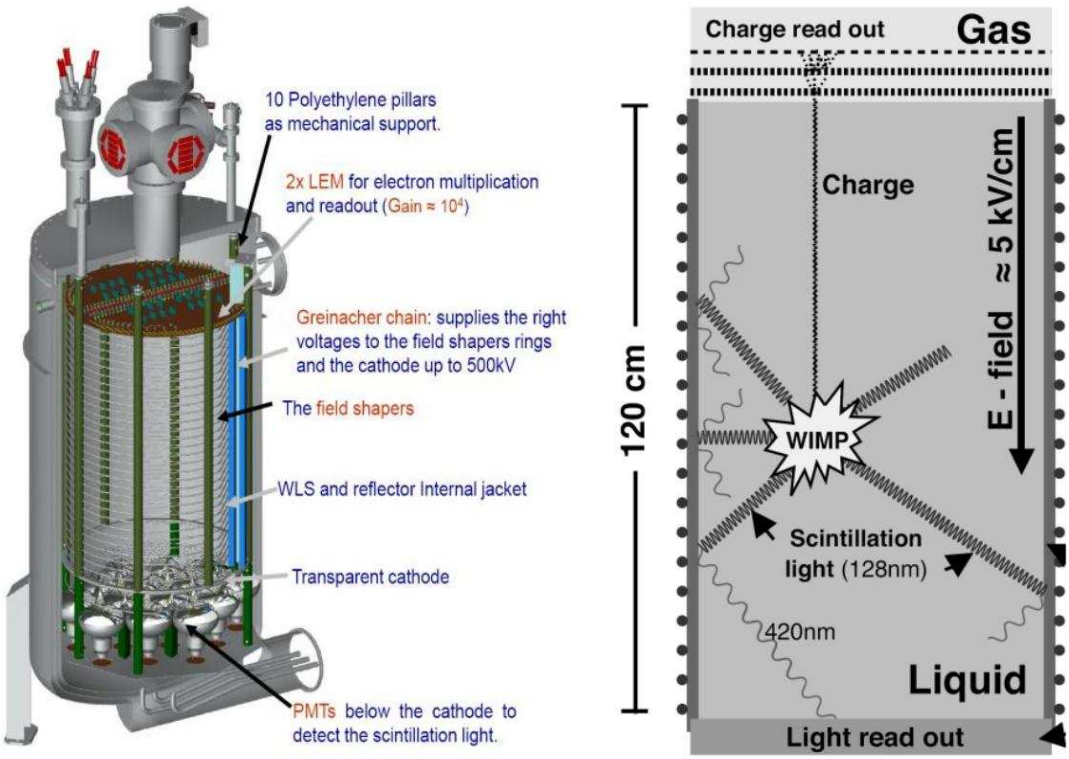

Figure 3.1: Schematic of the ArDM detector. Charge and light produced in interactions are readout with a LEM and 14 PMTs. An electric field, uniformized by field shaping rings is used to drift the charge up to the LEM.

Argon mass	850 kg
Maximum drift Length	120 cm
Drift Field	from 1 to 5 KV/cm
Charge Readout System	Large Electron Multiplier
Single Electron Gain	$10^3 - 10^4$
Light readout system	14 hemispherical 8" PMTs
Light collection efficiency	2-5% of total generated γs converted in photoelectrons

Table 3.3: Main parameters of the ArDM detector.

copper layer on top and bottom. Holes of about 500 μm in diameter are homogeneously distributed on the LEM, at a distance of 800 μm among them. By placing an electric field between both sides of the plate of $\sim$2KV/mm it is possible to generate an avalanche of electrons and to obtain charge amplification factors $\sim 10^3 - 10^4$.

Lastly, 14 PMTs of 8 inch diameter are installed outside of the drift region below the cathode. The inside of the field shaping rings is covered with 3M reflecting foils coated with TPB to shift to visible and reflect the scintillation light of liquid argon. Figure 3.3 show pictures of the vessel

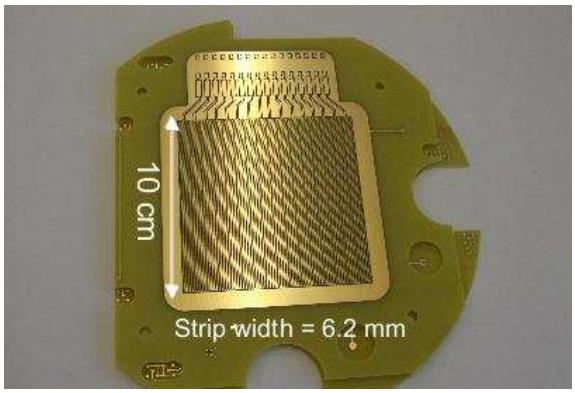

Figure 3.2: 10 cm prototype of the LEM for ArDM. Readout is performed by means of stripes with 6 mm pitch.

and the actual detector with the light collection system already mounted.

Figure 3.3: Left: Inner ArDM detector. In the image the installed PMTs, field shaping rings and the external part of the wavelength shifter sheets can be seen. Right: ArDM vessel. The empty flange on top connects the vessel with the purification and recirculation systems.

One non negligible drawback of natural argon liquefied from the atmosphere is the existence of the radioactive isotope ^{39}Ar which is a beta-emitter with a lifetime of 269 years and a value $Q = 565$ keV. Its concentration in atmospheric argon is well known and will induce a background decay rate of $\simeq 1$ kHz in a 1 ton detector [79]. In principle, the intrinsic electron/nuclear recoil rejection provided by the ratio of the scintillation to the ionization yields, which is extremely high for nuclear recoils (i.e., WIMP events) together with pulse shape discrimination, should be sufficient to suppress this background, provided the involved ratios can be measured precisely. This is intended to be fully addressed with the ArDM 1 ton prototype, which is a detector of the relevant size. It is possible as well to obtain argon from well gases. It has been recently measured that in this case the contamination of ^{39}Ar is $< 5\%$ that of the atmospheric argon [80]. However, the cost for this case is to be estimated. On the other hand, the ^{39}Ar decays, evenly distributed on the target, provide a precise calibration and monitoring of the detector response as a function of time and position.

This main feature of the detector, the possibility to independently detect the ionization charge and scintillation light, allows background discrimination by the measurement of the charge to light ratio. Moreover, the charge imaging together with the correlation with light provide a precise three dimensional localization of the event vertex in space, hence a good fiducial volume definition, important for γ-ray and slow neutrons background rejection from surrounding elements.

3.5 Light readout system

The ArDM light readout system is composed of a set of 14 8" PMTs placed in the bottom of the detector. For the first surface tests of the detector only the central 8 PMTs have been installed, and three different kind of PMTs have been used, among them those referred to in chapter 2. One of the tests goals is to decide which of them best suites the experimental requirements. Table 3.4 summarizes their main properties:

Manufacturer	Model	Gain	QE (@ 420nm)
ETL	9357 KFLB	1.1×10^7	18%
Hamamatsu	R-5912-MOD	10^7	22%
Hamamatsu	R-5912-02-MOD	10^9	22%

Table 3.4: PMT models used in the ArDM test run. Data for Hamamatsu are for a PMT without Pt underlayer.

These PMTs are placed as shown in figure 3.4. Their position have been chosen to be the closest to the center of the detector and to have the smallest surface of the PMT outside the region delimited by field shaping rings.

VUV light produced in the events is shifted to visible light by means of TPB coated sheets placed in the inner side of the field shaping rings. However, some photons can reach PMTs without hitting the walls (direct photons). To study the possibility to collect as well this photons, some of the PMTs have been coated with TPB to convert the 128 nm direct light to visible light that can be detected by the PMTs. Those uncoated are referred to as "unctd" in figure 3.4. Two different procedures have been used in order to establish which one produces more stable and efficient coating:

1. The PMT is placed in a chamber in which vacuum is done. A TPB sample is placed in front of the PMT and slowly heated by means of a resistor. When the TPB evaporates, it produces

Figure 3.4: Positions of the PMTs during the first surface test in the ArDM experiment. The position of the field shaping rings is marked with a white line. The first line on every PMT refers to the coating procedure (see text) and if the window has been shotblasted. The second line is the PMT model and the third one the serial number.

an homogeneous coating of the PMT. PMTs coated using this method are referred as "evap" in figure 3.4.

2. The PMT is dipped in a solution of chloroform, TPB and PRL, a polymer to make more stable the deposition. When it comes out, the chloroform evaporates very fast, and only TPB and PRL remain. This produces a coating almost transparent for visible light that could help a more efficient collection of shifted light. PMTs coated using this method are referred as "TPB/PRL" in figure 3.4.

The light acquisition setup is shown in figure 3.5. The signal of each PMT is connected to a fan in fan out which splits each signal in four identical copies, with a bandwidth of 200 MHz.

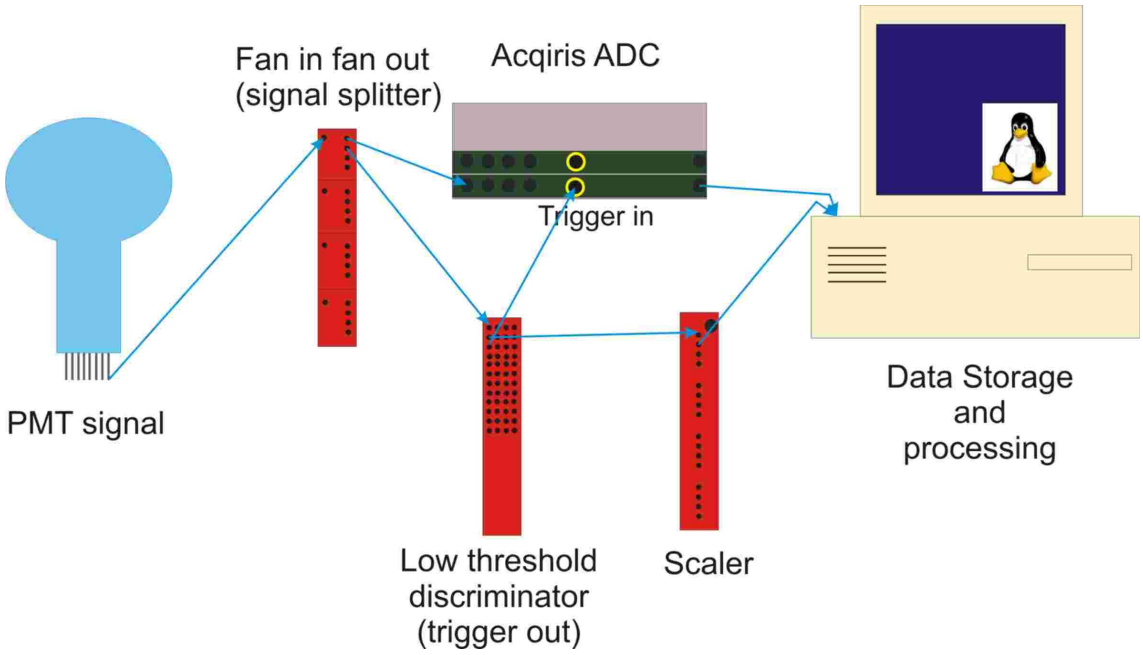

Figure 3.5: Schematic of the light acquisition system of ArDM.

For the readout of the PMTs, a set of Acqiris ADCs is used which samples every channel at 1 GHz rate. The output voltage value for each PMT is stored in a 10 bit variable, and the maximum value of this variable can be changed prior to the acquisition between 0.05 and 5 volts.

The trigger is provided by means of a low threshold discriminator (LTD) in which each channel threshold is set to the measured value of $\sim 1/2$ pe for each PMT. The trigger is provided by a majority of 4 channels. This trigger choice, that will be justified in the next sections, is set to reduce triggering on dark counts as much as possible.

A scaler is also present to make measurements of rates of signals for each PMT and for the majority of them. Figure 3.6 shows an image of the light acquisition setup.

3.6 Light measurements

From September to November 2007, a part of the light system of the ArDM detector was assembled, taken inside the experiment dewar and put to test to understand its performance. This included all the wavelength shifter foils together with a half of the final experiment PMTs (see figure 3.4). A series of tests were developed in order to demonstrate the operation of the light acquisition system prior to full assembly. To do so, it was installed on the top flange a metallic rod that could be moved inside the dewar without breaking the vacuum thanks to a magnet placed in the outside. On the end of this metallic rod, A LED was installed, providing illumination of the PMTs, together with an alpha source[3], composed of ^{241}Am. Moreover, another LED fixed on the top of the dewar

[3] 40 KBq activity, α-energy 4 MeV.

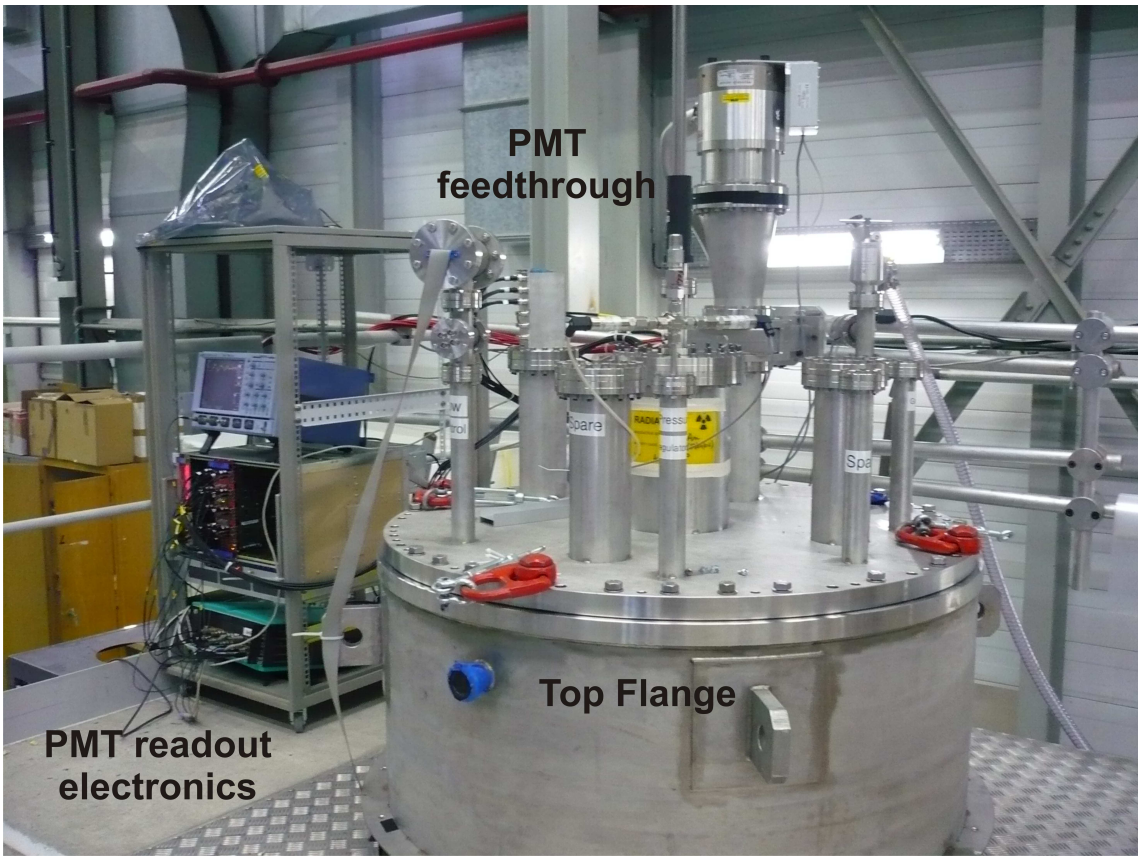

Figure 3.6: Light acquisition experimental setup of ArDM.

was installed in order to provide almost homogeneous illumination of the PMTs. Figure 3.7 shows a schematic of the actual setup.

The test period was divided in two phases. In the first period, vacuum was done inside the cryostat, and by means of the LEDs (alpha source does not produce light in vacuum) the characteristics of each PMT signal were individually studied, under realistic experimental conditions. In the second phase, the detector was filled with gaseous argon to study the light acquisition system (PMTs + reflectors) performance under the alpha particles interactions. A third phase will be carried out in liquid argon. It is important to remark that during these tests only the light system and the slow control were working in the experiment, while all the electric field system, charge readout, and argon recirculation systems were switched off.

3.6.1 Vacuum Calibration

Once all the PMTs were mounted in the detector and a good vacuum was achieved, the first test carried out was a simultaneous calibration of all of the PMTs by means of a LED installed inside the cryostat. This LED was pulsed at an intensity such that most of the non-empty events were single photoelectron events, as explained in chapter 2. The signal from each PMT was then measured by

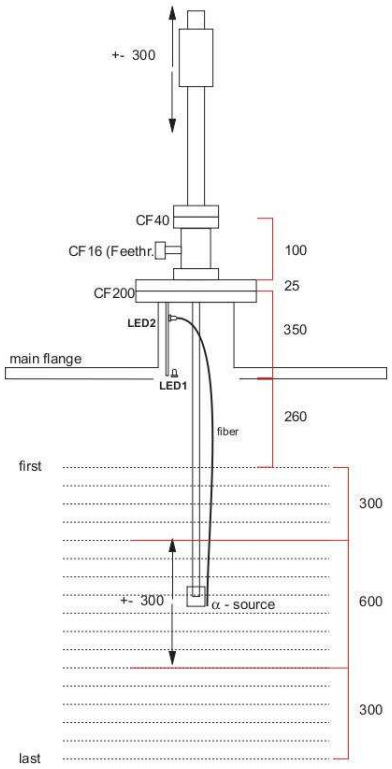

Figure 3.7: Schematic of the setup used for surface tests. A movable α-source and a LED are attached to the end of a rod which can be moved through a magnetically connected external piece. Another LED is fixed in the top of the detector.

means of an Acqiris ADC, and afterwards it was integrated to get the charge deposited per event. Figure 3.8 shows a screen capture of the acquisition computer for one of the first recorded events.

With the measured values and following the procedure explained in the previous chapter, the gain for different values of the voltage for each PMT was computed. The results are shown in figure 3.9.

There are three clearly separated regions corresponding to the three kind of PMTs. The ETL PMT needs higher voltage to work due to a special configuration of the base. According to the manufacturer, the best functioning is achieved by setting a fixed voltage between the photocathode and the first dynode of $\sim 500\,\mathrm{V}$. This is done by feeding the PMT with 2 different voltages, one for the photocathode and one for the dynode chain. For the other PMTs this voltage is set by a resistance whose value is typically one half the one from the rest of the chain. Hence, the voltage difference between photocathode and first dynode is approximately one third of the supplied voltage.

As expected the highest gains can be obtained with the R-5912-02 PMTs (14 dynodes), which show a large increase of gain with voltage, as well. The ETL-9257 PMT (12 dynodes) can reach high gain values too, although at highest voltages. However it should nominally work at $\sim 10^7$ gain. The Hamamatsu R-5912 PMTs (10 dynodes) are those with the lowest gain, having the lowest gain increase with voltage. However, all of the PMTs can achieve a gain of 10^7 which is

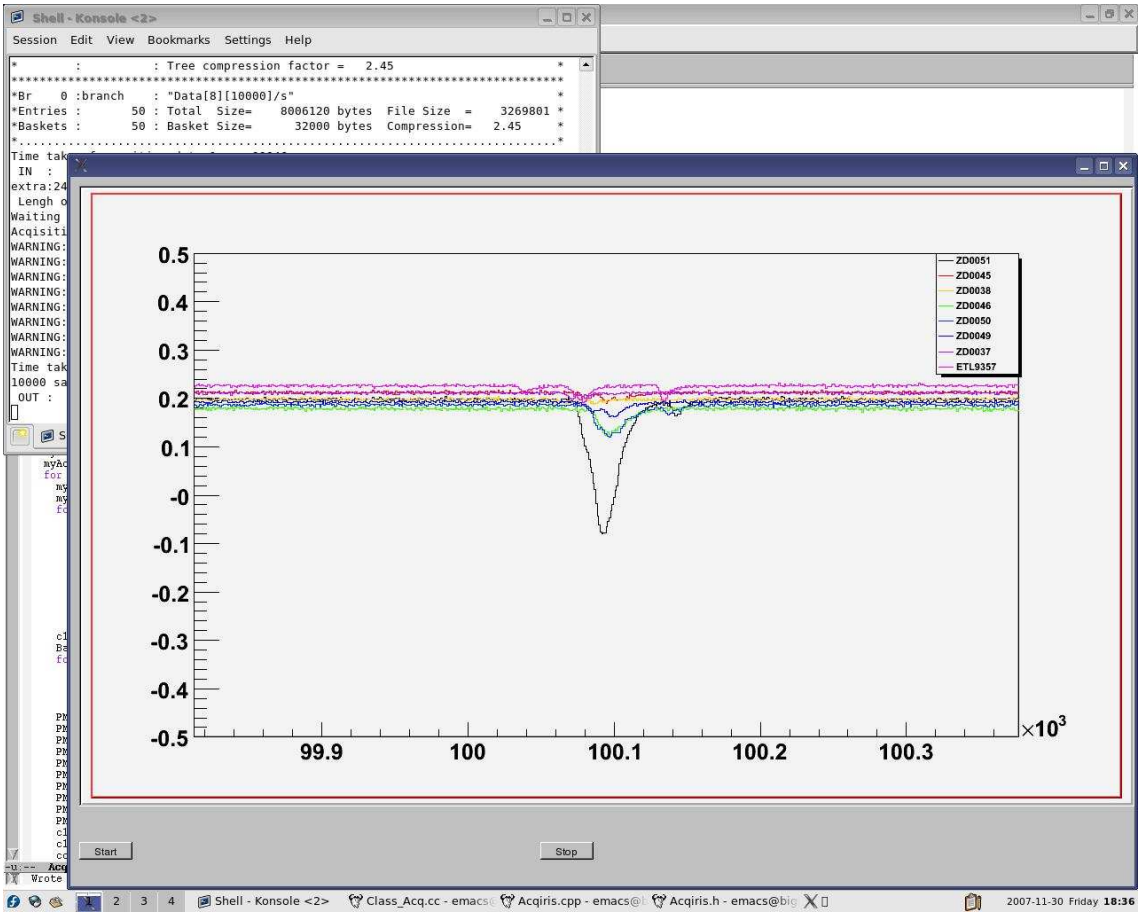

Figure 3.8: Screen capture of a typical event simultaneously seen by all of the installed PMTs. Signal voltage is shown in Y axis and time in X axis. Main differences in intensity are due to different gains.

enough to detect single photoelectrons without any external amplification. Also the noise levels observed are $\leq 1\,\mathrm{mV}$, which allows to clearly measure single photoelectrons even for the lowest gains.

3.6.2 Alpha source measurements

Since the argon recirculation system was not available during these tests, a method different from the final one for the argon filling was adopted. The dewar was pumped for more than 24 hours until a good vacuum inside was reached. Then it was filled with gaseous argon to take away the impurities left and vacuum was done again. Finally the dewar was filled from very pure gaseous "Argon 60" bottles, and the measurements with the alpha source could be done. After one to two days, the purity inside the experiment degraded and was not good enough to work and the process had to be repeated.

As already mentioned, during the test period, the detector was equipped with a movable ac-

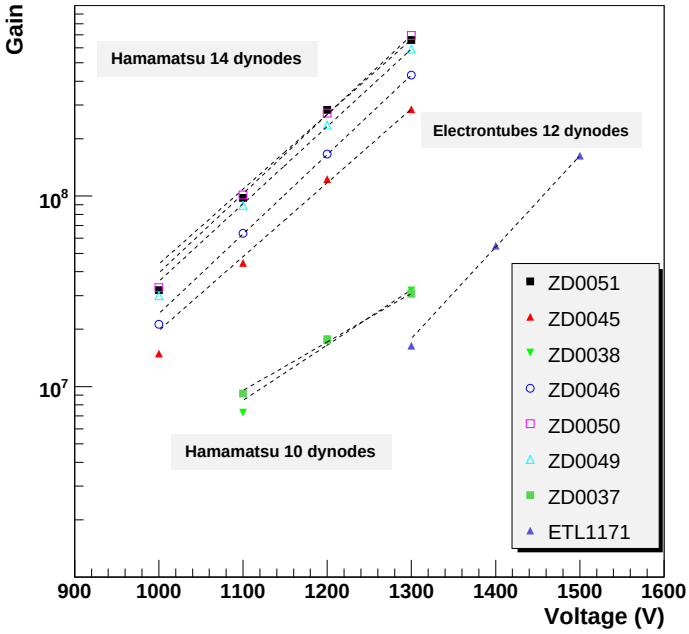

Figure 3.9: Simultaneous calibration of all the PMTs installed in the ArDM experiment.

tuator on top of which there was an alpha ^{241}Am source with an activity of 40 kBq. The alpha source was placed inside a capsule for safety purposes, which made the alpha energy to decrease in ~ 1 MeV.

During these tests, all the work was made in gas argon. Due to the low rupture voltage in this medium, some of the PMTs could not operate at their rated voltage due to spark production, and data could only be collected from 6 of the PMTs (five R-5912-02 and one R5912). This, however, will not be a problem when working in liquid argon, where every PMT has been individually tested and with a much higher rupture voltage.

The first measurements carried out were coincidence measurements in order to set an appropriate trigger for the source. We measured the number of coincidences between PMTs as a function of the threshold level, i.e., as a function of the event energy. This was done by splitting the signal of the PMTs by means of a 120 MHz bandwidth linear fan-in fan-out. One of the outgoing signals was then sent to an ADC, which was not used for this task (it is used to collect signal shapes), while the other signal was sent to a 16-channel low threshold discriminator. The threshold value in the discriminator was remotely controlled, and the output of each PMT plus a majority output was sent to a VME scaler which was remotely read from the computer. We repeated this measurement for different number of PMTs in coincidence (i.e., different majority threshold). Results for 2 and 4 PMTs simultaneous signals are shown in figure 3.10.

It can be seen clearly that the trend for 4 PMTs is similar to the expected behaviour of the source, with the number of events decreasing constantly with energy and a maximum threshold over which no events can be seen, in opposition to what happens for only two PMTs, where random

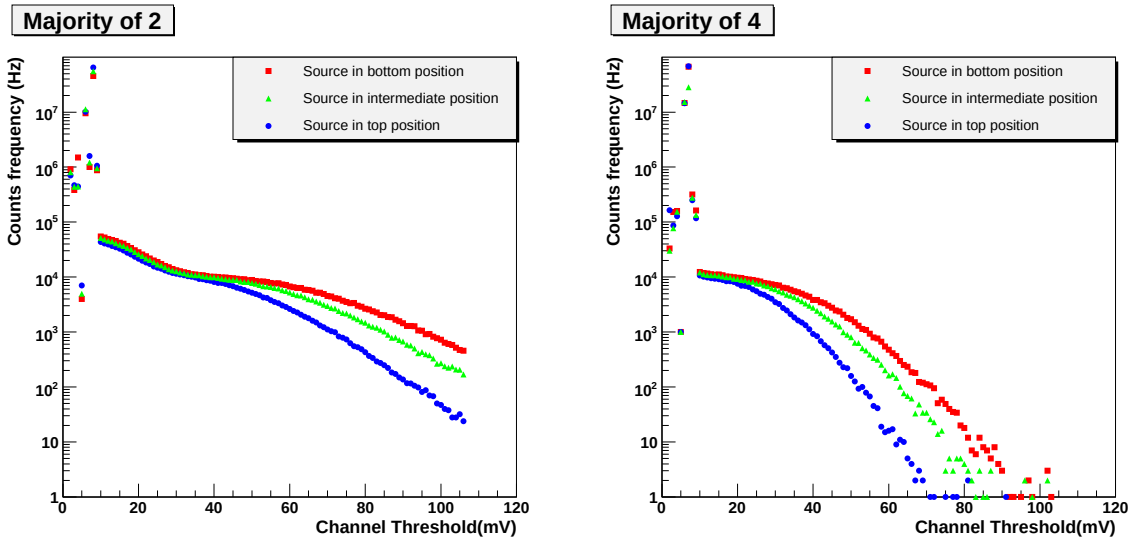

Figure 3.10: Number of counts with a coincidence of several PMTs with the ^{241}Am alpha source in gaseous argon. Left: Coincidence of at least 2 PMTs. Right: Coincidence of at least 4 PMTs.

coincidences from dark counts play a much more important role.

As can be seen in figure 3.10, these measurements were repeated for different positions of the alpha source, obtaining in all cases similar trends, and with a larger number of events the closer the source was to the PMTs, as expected.

From this measurement, it was decided to consider as trigger for the rest of the measurements, an event in which four of the PMTs have a signal above the valley simultaneously. The signal of four PMTs on a triggered event can be seen in top of figure 3.11. Simultaneous peaks can be seen in all of them for time ∼1000 ns corresponding to the triggering of the event. In a later time several single photoelectrons can be seen in each of the PMTs.

Measurements with the alpha source at different positions were carried out for all of the 6 PMTs. An individual measurement consists of one single peak at the trigger position plus a few single photoelectron peaks away from the trigger. When several of these events are averaged, the initial peak is clearly distinguishable while the single photoelectrons add up together to give rise to a continuous exponentially decay spectrum. Figure 3.11 shows the average signal for one PMT during a whole run. Overimposed to the signal there is a line corresponding to a fit to a double exponential function. Parameters p3 and p4 correspond to the fast and slow decay times of the signal respectively, which come from the singlet and triplet molecular states.

The decreasing part of the function separated from the peak correspond to the slow component of the signals, i.e., photons coming from the triplet state of the excited molecule. These states are affected by the purity of the gas, and the measurement of the decay constant gives a measurement of the gas purity. Figure 3.12 shows the decrease of gas purity with time, due to the lack of the recirculation system. A perfectly clean gas correspond to a decay time of 3.2 μs.

By the integration of the signal shown at the bottom of figure 3.11 the average number of photoelectrons seen by the PMT can be obtained. However, this number depends on the purity of the gas during the data taking, which makes difficult to compare data measured at different times. To do so, the signal has to be fitted in order to get the fast and slow component time constants

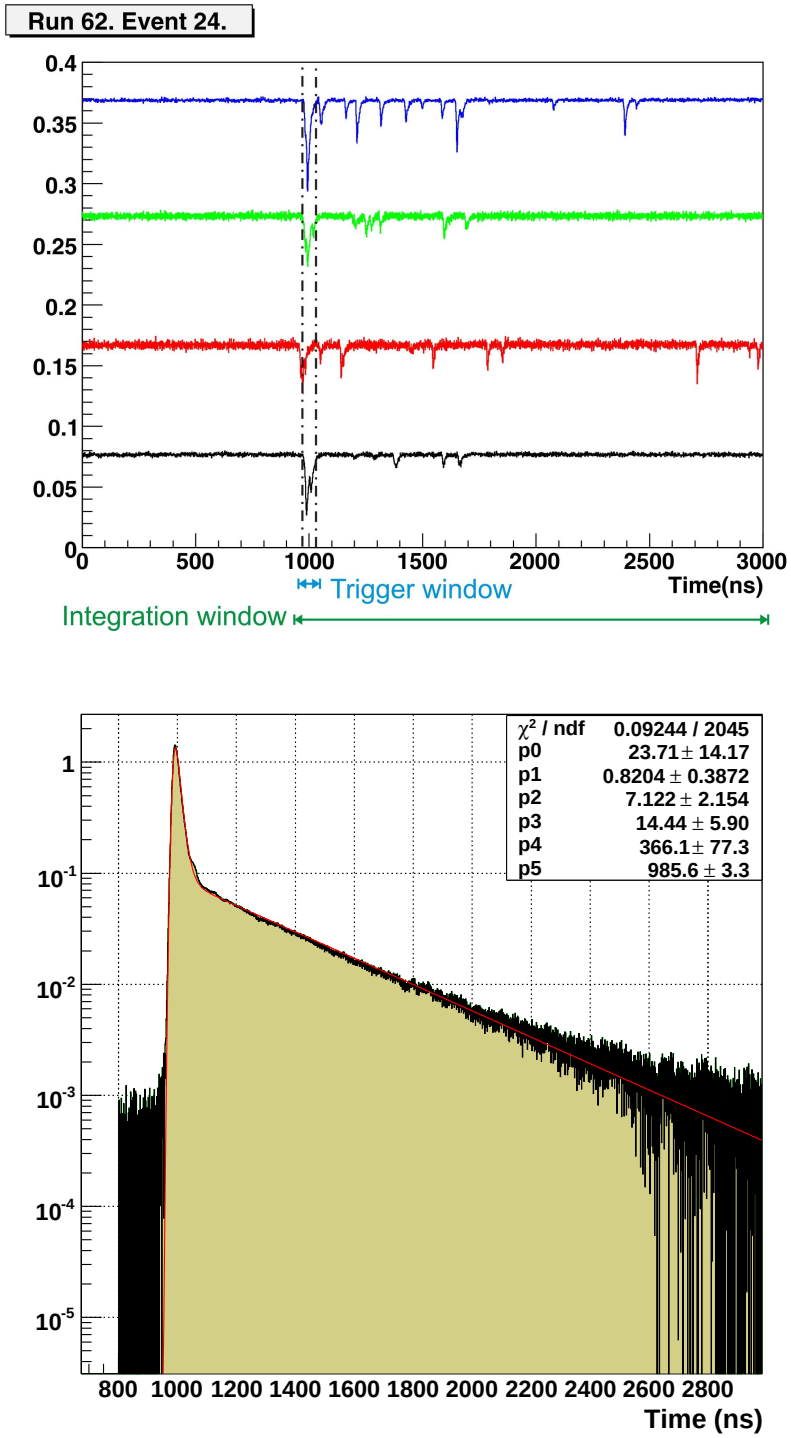

Figure 3.11: Top: Signal of four PMTs for a triggered event. All the channels show a peak in the trigger window, followed by several single photoelectron events corresponding to slow emission. Bottom: Average spectrum seen by one of the PMTs during a run. X-axis show time in ns while Y-axis shows the voltage in arbitrary units.

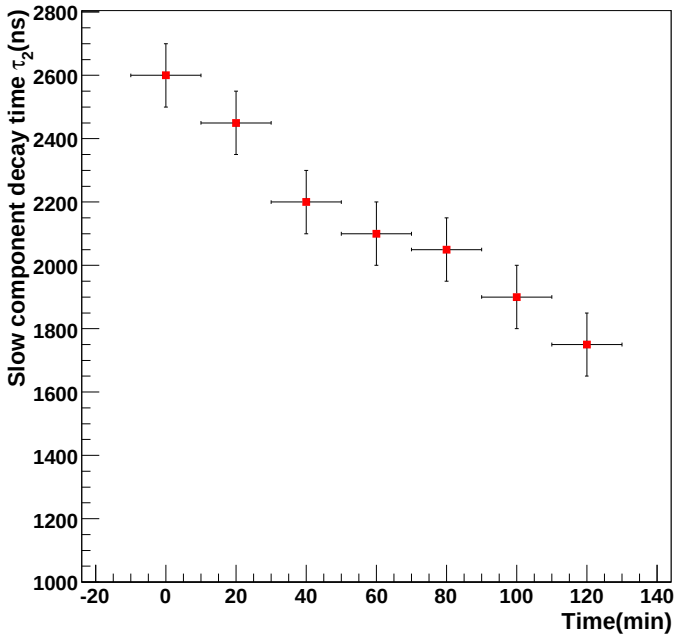

Figure 3.12: Purity (slow component decay time) degradation with time.

together with the peak position, and a new integral is performed over the fitted function using 3.2 μs as the slow decay time constant, so all of the results are referred to a clean gas.

Figure 3.13 top shows the average number of photoelectrons seen at different distances from the center of the detector by each of the PMTs, as computed for clean gas. Negative distances refer to positions close to the top, while positive ones correspond to those close to the bottom

As expected, the closer the source to the PMTs, the higher number of detected photoelectrons. There are two clear regions differentiated in the plot: the upper one, corresponding to those PMTs in the center of the detector; and the lower one, to those which are in the side and whose collection window is not completely inside the detection area. A second effect visible in this plot is that there are two PMTs for which the number of seen photoelectrons does not increase with distance uniformly. These two PMTs (ZD0038 and ZD0049) are those which are not coated with TPB and hence they are only sensitive to shifted light. The observed behaviour can be explained by considering that once the source is close enough, there is no decrease in the amount of indirect light and only the direct one increases.

One may try to map the number of photoelectrons as a function of the position of the PMT. This is done at the bottom of figure 3.13. Squares represent the position of each PMT, and the color scale shown on the right together with the overimposed numerical value for each PMT. It can be seen the actual detector positioning as well.

Those PMTs closer to the center of the detector see a higher amount of light, while those which are close to the borders and for which a part of the PMT is not inside the area corresponding to the active volume see less. In the next section we will compare all these data with the MonteCarlo

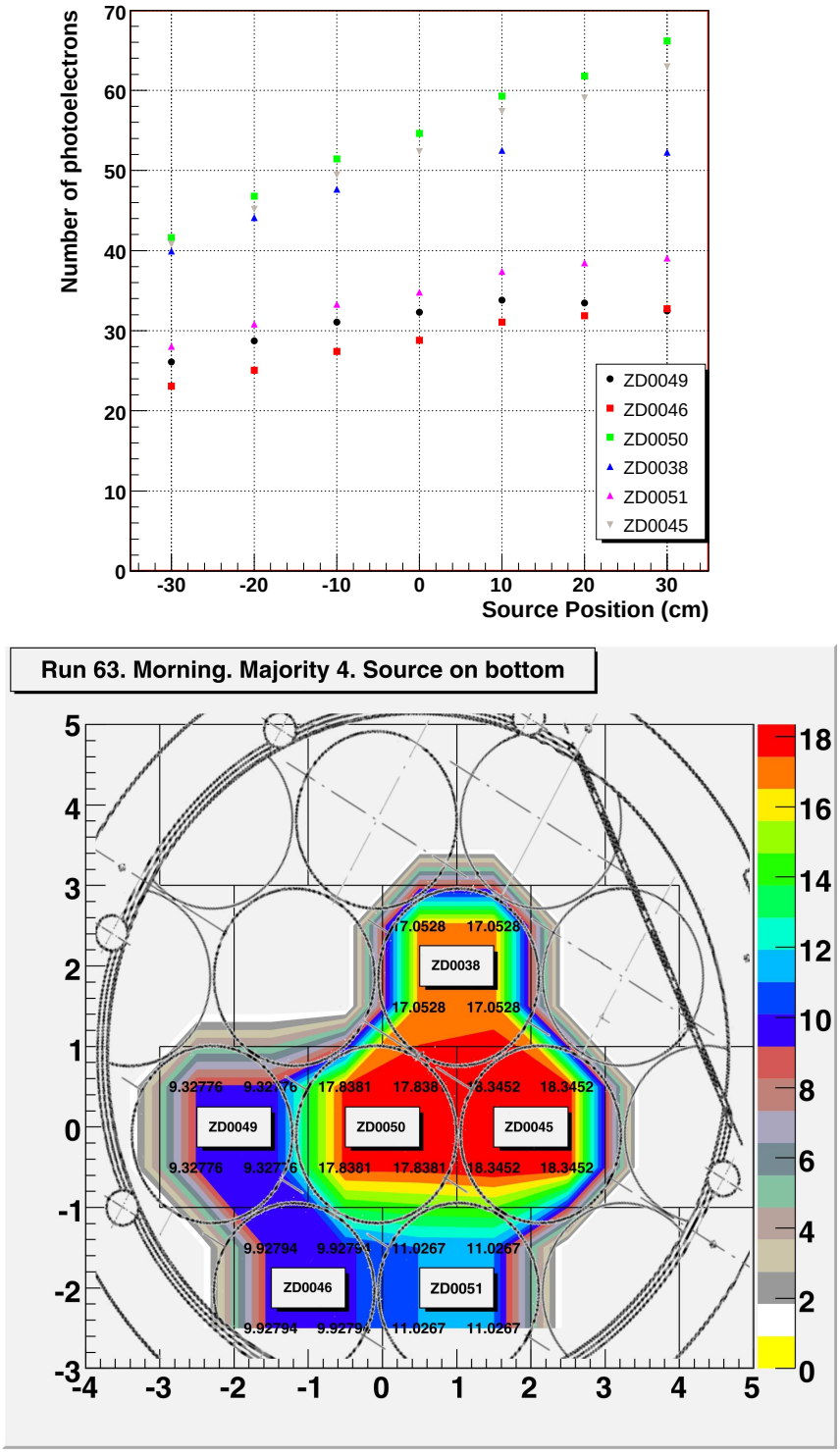

Figure 3.13: Top: Number of photoelectrons seen by each PMT as a function of distance to the center of the detector (negative top, positive bottom). Bottom: Spatial distribution of photoelectrons on the PMTs.

simulation of the detector.

Comparison with MonteCarlo simulation

A dedicated Geant4 simulation has been developed by members of the ArDM collaboration. Figure 3.14 shows a side view of the simulated geometry. PMTs, reflecting sheets, LEM, pillars, field shaping rings and other parts of the detector have been included in the simulation. It is possible to shoot from any position inside or outside the detector particles to see their interaction and light production. It is also possible to generate recoiling nuclei, simulating a WIMP interaction, or even photons, if just light properties are to be studied.

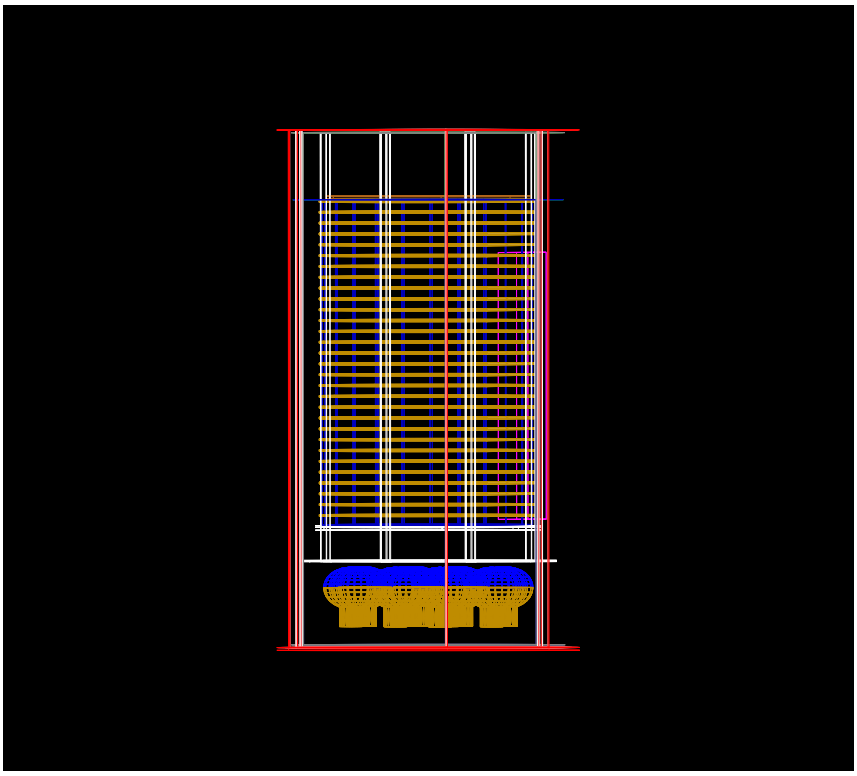

Figure 3.14: MonteCarlo simulation of the ArDM detector geometry. It is possible to see the dewar, the pillars, the field shaping rings, cathode and the PMTs.

This MonteCarlo simulation has been used to study the data taken in the alpha source tests with argon gas. To do so, we simulated photon production at different heights in the center of the experiment dewar and studied the percentage of photoelectrons seen by each PMT. In our study, the properties of all of the PMTs are taken to be the same. Different quantum efficiencies are computed depending on the point of the PMT in which the photon hits, according to the curve from [81]. Reflectivity in the wavelength shifter is set to 95% which is a value similar to our expectations and to that measured in other experiments.

In first place we observe that the 6 working PMTs see approximately 50% of the total light. If we add now the number of photoelectrons that our 6 PMTs have measured and extrapolate this

number to the whole 14 PMTs, we can compute the light yield for our 4 MeV alpha source. We obtain that, in gaseous argon, the light yield is ~ 0.17 pe/keV. This result is not related with the one that will be obtained in liquid argon, as there are several parameters that influence the light yield like pair creation energies or ionization density that are different between the gas and liquid phase. If one accounts for these parameters, the obtained light yield is $\sim$0.8 pe/keV, result that has been confirmed by other simulations [82].

It is possible to compute for each PMT and for all of the positions of the source what is the predicted number of photons emitted by the alphas. This can be done by shooting photons at different heights and then with the MonteCarlo simulation computing the percentage of the total photons seen by each individual PMT. Considering the impact angles on each PMT and if these are or not sensitive to non-shifted photons, it is possible to know how many photoelectrons one expects from each 100 emitted photons. Knowing this value and the measured number of photoelectrons at each PMT, it is possible to predict for each of them and for every position the number of photons emitted by the source. This is shown in figure 3.15.

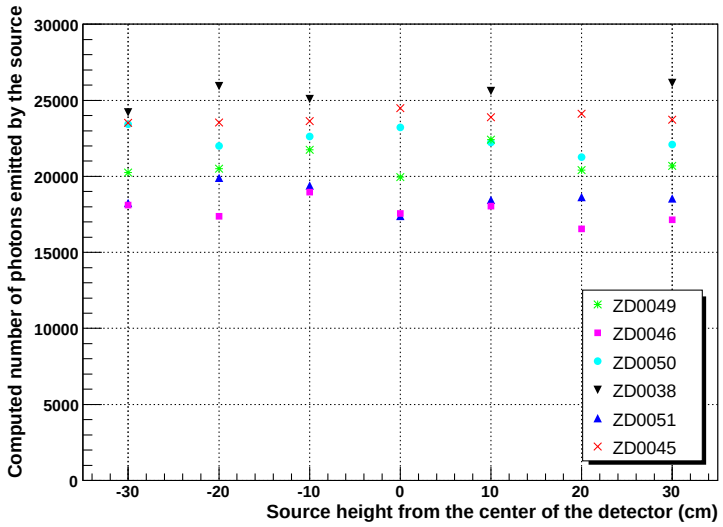

Figure 3.15: Prediction of the number of photons produced in the source from the data of each PMT according with the MonteCarlo simulation.

Regarding the predicted absolute number of photons, we can only say that the order of magnitude is the expected one. There are several factors affecting this number, as gas purity, the influence of the source encapsulation, and so on, that make difficult an accurate prediction at this stage. More work is on progress, but is out of the scope of the present thesis.

If only one PMT is considered, it follows a quite constant trend, with variations of less than 10%. This shows that the predicted result does not depend on the distance between the source and the PMTs, or in a different way, the prediction for the light behaviour as a function of height in the detector matches the experimental results.

On the other hand, it is possible to compare different PMTs among them. In this case we see discrepancies of the order of 15% and bigger. However, one has to keep in mind that the same quantum efficiency has been considered for them all, and even for pieces of the same model

differences in properties of the order of 15% are quite common. Hence, we find that all of them yield similar values for the total number of photons, between 20000 and 25000. This means that the spatial distribution of the light provided by the simulation matches again with the observed ones.

3.7 Conclusions

In this chapter we have presented the experimental observations that support the existence of dark matter. Among all the possible candidates, WIMPs seem to be one of the most favored discussions. We have explained the interactions that WIMPs have with ordinary matter, and in this context we have discussed the possibility of using a liquid argon detector for direct dark matter searches.

The ArDM detector is a 1 ton scale liquid argon detector for dark matter searches. The first prototype, similar in size to the final detector, is already being assembled at CERN. It is intended to go through a series of surface test in order to prove all the adopted solutions for electric field, charge readout and light readout. Through this chapter, we have presented the details of the assembly as well as the first results of the light readout system in the tests carried out in vacuum and with gaseous argon. The operation of the PMTs inside the dewar has been satisfactory, showing performances similar to those already measured in the laboratory and proving the good working of the acquisition electronics. Moreover, thanks to the alpha source, the whole light collection system has been tested and the global performance of the detector has been measured, matching the expectations from MonteCarlo simulations. During the next months, new tests in liquid argon will be carried out to prove also the proper operation of the system under cryogenic conditions.

Chapter 4

Backgrounds in a direct dark matter experiment: identification with a hybrid detection technique

The physical magnitude measured by a dark matter experiment, in the case no signal is observed, is a limit to the rate of dark matter interactions inside the detector, which is later transformed in a combination of masses and cross sections to produce an exclusion plot. The limit that can be set to this rate depends on the exposition time and mass, and on the expected amount of background events. Up to date, no direct [72, 73, 74, 33, 41] or indirect detection methods [83, 84] have found a signal that can be attributed to a WIMP, let alone the claim done by the DAMA collaboration [71]. The limits on masses and cross sections correspond with signals that in the best case are of $\sim$1000 events per tonne$\times$year, which makes the background shielding an important and challenging question.

This chapter is devoted to the study of the backgrounds in a dark matter experiment using noble liquids as sensitive medium. To enhance direct WIMP search sensitivities, we study the performance of a hybrid detection technique: cylinders filled with liquefied noble gasses, acting as targets, are immersed inside a tank of Gd-doped ultra-pure water that provides an active and efficient veto against neutrons.

4.1 The hybrid detector

Liquid noble elements, used as sensitive medium for direct dark matter searches, are a promising alternative to ionization, solid scintillation and milli-Kelvin cryogenic detectors. As previously discussed, when a WIMP particle scatters off a noble element, scintillation photons and ionization electrons are produced due to the interactions of the recoiling nucleus with the neighbouring atoms. The simultaneous detection of primary scintillation photons and ionization charge (or the secondary photons produced when this charge is extracted from the liquid to the gas phase) is a powerful discriminator against backgrounds. Pulse shape provides an additional tool to identify true signals: depending on the nature of the interacting particle, the scintillation light shows a different time dependence [17]. In addition, thanks to the high level of purity achieved, these detectors can drift ionization charges for several meters, hence it is conceivable to reach masses of the order of several tonnes. Nowadays XENON, ZEPLIN, XMASS-DM, WARP and ArDM collaborations use

liquid argon or xenon targets to look for WIMPs. Similar detectors can be used to detect the yet unobserved coherent neutrino-nucleus elastic scattering [85].

Assuming a one ton detector, we expect an event rate of O(1000) events per day for a WIMP-nucleus cross section of 10^{-6} pb, before cuts. For 10^{-10} pb, O(10) events per year of operation will occur. To explore such small cross sections, backgrounds should be reduced to very challenging levels (about 1 event per ton per year). In case the detector is filled with argon, the ^{39}Ar isotope, which is a beta emitter, is a serious source of concern (its activity is approximately 1 Bq per kg of natural argon). However, the most important source of background is due to neutrons produced in detector components or in the rock of the underground cavern. A large fraction of these external neutrons can be rejected using external hydrocarbon shields, active vetoes or a combination of the two [86]. High-energy neutrons induced by muon interactions in the rock are a more serious concern. Recently, an innovative neutron multiplicity meter, very similar in concept to the detector discussed in this chapter, has been proposed to monitor this neutron flux [87]. The flux of internal neutrons can be highly reduced using low activity materials for the inner parts of the detector. However, it is unavoidable that some of them interact with target nuclei mimicking a WIMP signal.

Detectors with a large fiducial volume (like the one discussed on chapter 3) offer the advantage of an increased probability for neutrons to interact several times, before they exit the target. For WIMPs this is highly unlikely given the small cross sections involved. This fact can be used to further reduce neutron backgrounds. Here, we explore the opposite approach: to reduce the neutron contamination, we use targets of reduced dimensions in order to avoid as much as possible neutron capture inside the target. In what follows, we study the physics performance of a hybrid detector: it consists, on one hand, of an external active veto of ultra-pure water doped with gadolinium, in order to enhance neutron capture and its posterior identification [88]. Immersed on this veto, there are cells filled with a noble element, acting as target, and whose dimensions have been reduced in order to decrease as much as possible the chance that a neutron scatters twice or gets absorbed within it. If energy deposits occur, within a certain time window, both in the cell and water, the event is tagged as neutron-like provided the external veto records the typical 8 MeV gamma cascade from neutron capture on gadolinium.

4.1.1 Noble liquid target

We have carried out a full simulation of the proposed detector using GEANT4 [89] (see figure 4.1). The active target is made of 100 low-background metal cylinders (each 34 cm high and 18 cm in diameter, hence 8.7 l in volume) that can be filled with a noble liquid. The total mass amounts up to 2.5 tonnes in case the detector is filled with liquid xenon (LXe) and 1.2 tonnes in case liquid argon (LAr) is used. Our device can detect simultaneously the ionization charge and the scintillation light resulting from the scattering of incoming particles off xenon or argon nuclei. Light is read by means of PMTs placed at the detector bottom. Ionization electrons are drifted to the liquid surface where they are converted into secondary scintillation light that is read by PMTs on top of the detector. Charge amplification devices (i.e., GEM, LEM, Micromegas [90, 91, 92]) are a possible alternative for direct charge readout.

This configuration of independent cylinders, apart from the fact of being easily scalable, offers a clear experimental advantage: data taking can proceed with two different targets simultaneously. Cylinders can be filled with argon and xenon, for example. In case a WIMP signal is observed with enough statistical relevance, we can confirm in a single experiment that the event rate and the recoil spectral shape follow the expected dependence on A^2.

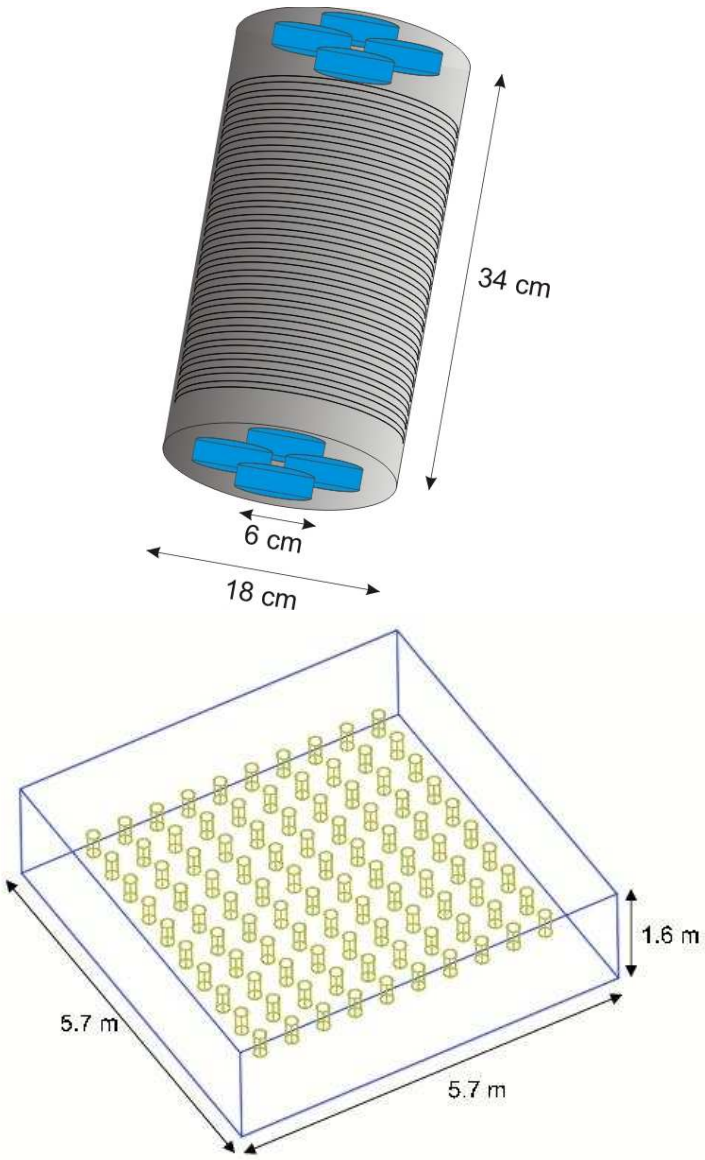

Figure 4.1: (Top) Artist's view of one of the target cells. Each of them is instrumented with eight 6cm-diameter photomultipliers. (Bottom) GEANT4 simulation of the whole detector.

4.1.2 Active neutron shield

The active target is immersed in a water tank (1.6 m height, 5.7 m width and 5.7 m long), made of copper or other low background material. The distance between cylinders is 30 cm. The distance to the veto walls is 60 cm. This distance has been optimized to allow an efficient neutron capture by gadolinium. The veto contains 51 tonnes of ultra-pure water. 1500 8" PMTs (close to 50% photo-coverage), located at the water-tank walls, are used to detect the photons produced by neutron capture on Gd. They will detect the light produced by penetrating cosmic muons, as well, thus providing an efficient veto against this kind of events.

Following the approach discussed in [88], we have doped in our simulation the water-filled parallelepiped with highly-soluble gadolinium trichloride. To avoid the absorption of photons by the cylindrical targets, we propose a solution similar to the one used in the Pierre Auger Observatory [93], namely to cover their external walls with Tyvek (a material that shows a reflectivity higher than 90% to Čerenkov light [94]). A particular source of concern is the radio-purity of the additive. According to the estimations given in [88] and [95], the potential background caused by it, specially the alpha decays of ^{152}Gd, is much smaller than what is expected from the sources considered in section 4.2. The proposed amount of gadolinium has been chosen in order to minimize the number of neutrons captured by hydrogen nuclei. A dedicated GEANT4 simulation has been carried out to study this topic. A 1 meter radius sphere filled with Gd-doped water has been simulated and neutrons with energies between 0 and 10 MeV have been shot from the center. Figure 4.2 shows the obtained results. We observe that while the total number of absorbed particles does not change with Gd concentration, the proportion of Gd-absorbed particles increases with Gd concentration, saturating at a value $\sim 2\%$. Hence, we will use this value as a reference in what follows.

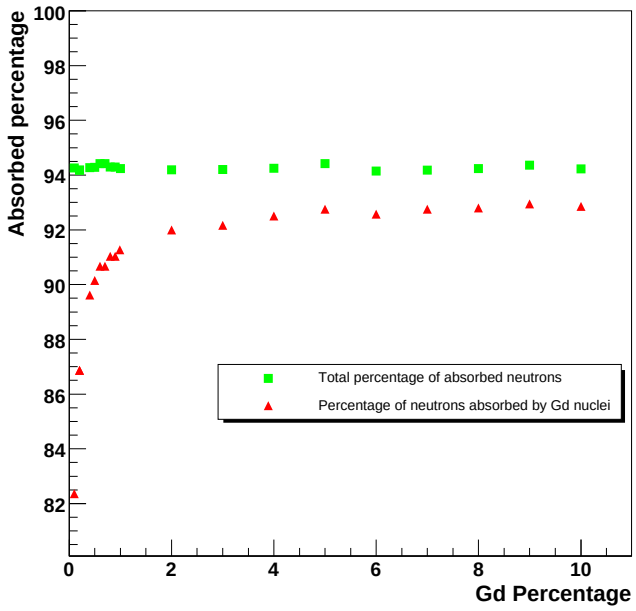

Figure 4.2: Number of absorbed particles as a function of the Gd concentration

4.2 Physics performance

The estimation of the overall background event rate in the fiducial volume must take into account both internal and external sources of gamma rays and neutrons. We conservatively assume that, due to instrumental limitations, we cannot detect signals below 30 (15) keV of true recoil energy in case we use a argon (xenon) target. On the other hand, we will assume a maximum recoil energy for WIMP-like events of 100 (50) keV for the argon (xenon) target. We note that it has been recently suggested that neutrinos can be a source of background for the next generation of direct-search dark matter experiments [96]. In that work, the possibility of observing neutrino nucleus coherent scattering in dark matter detectors is analyzed. They represent an irreducible source of background as they can not be shielded. For recoil energies above 1 keV, the only contribution comes from ^{8}B solar neutrinos, and the rates above 2 keV are of 231 (15) interactions per tonne×year for an argon (xenon) target. The spectrum of the produced nuclear recoils decreases with energy. Hence, as discussed in the paper, the only way to avoid this background is to set a lower limit on the energy of the events such that a negligible number of neutrino events remain. However, for the case of argon (xenon) the previous limit we imposed on the minimum energy, >30keV (>10keV) is already far above the one needed to render negligible the background due to the neutrino events.

4.2.1 Contamination from radioactive nuclei, xenon and argon isotopes

For a detector made of argon, an important source of background comes from the presence of radioactive ^{39}Ar. This is a beta emitter with an activity of about 1 Bq per kg of natural argon [79], which for a single-volume 1 tonne detector translates into a 1 kHz rate. In our case, since the target is divided into hundred independent units, the event rate due to ^{39}Ar decays does not represent an issue for the design of the DAQ system. In addition, the probability to have a ^{39}Ar decay overlapping with a different sort of interaction is smaller than in the case of a single-volume large-size detector due to the smaller drift times involved.

Regarding the possibility of misidentifying ^{39}Ar signals as WIMPs, we should note that β-particles mainly interact with atomic electrons, while nuclear recoils deposit their energy through transfers to screened nuclei (see chapter 3 and [97]). This affects the charge generated by an event (for the same energy is around 3 times bigger for electrons), the charge to light ratio, which is bigger for electrons, and the ratio between the slow and the fast component of the scintillation light of liquid argon (pulse shape discrimination).

According to our simulations, the ratio of measured scintillation light over ionization, together with pulse shape discrimination can reduce the background due to radioactive nuclei to a level well below the one expected from neutrons. The rejection power of these combined techniques agrees with the results quoted in [33] and [98]. A further reduction of this kind of background will come from the use of underground-extracted argon [80]. Its ^{39}Ar activity has been recently measured for the first time and shown to be <5% of the one present in natural argon. These reasons lead us to not consider further this sort of background.

In case the detector is filled with xenon, ^{136}Xe is the most important radioactive isotope. It decays through double beta decay and therefore, given the small probability of the process, the resulting count rate, in the energy band of interest, is negligible compared to other sources of background, even before any rejection cut is applied.

Krypton and radon are two radioactive nuclides present in commercially available noble gasses and therefore a potential source of background as well. The highest contamination comes from ^{85}Kr, which β–decays with an endpoint energy of 678 keV. However, impurities of Kr below 10 ppb can be reached [41], making negligible the contamination produced by those radioactive decays.

4.2.2 Neutrons from detector components

One of the most important sources of background comes from neutrons produced by radioactive contamination of the materials constituting the detector itself. To minimize their rate, the use of copper for all the vessels is likely to be the best possible choice. The radioactive impurities can be reduced below 0.02 ppb in some copper samples which would bring the neutron contamination to below 1 event per year [99]. If we conservatively assume a 0.1 ppb contamination, one obtains a neutron production rate of 4.54×10^{-11} $s^{-1}cm^{-3}$. Being each cylinder 6 mm thick, its total volume amounts to 1539 cm^3. This means a total of nearly one neutron per cylinder per year.

The contamination induced by PMTs must be carefully evaluated as well. Main manufacturers continue to optimize the choice of materials used in PMT construction to reduce their radioactivity levels. Typical contamination values for U and Th range from a few tens to several hundreds parts per billion. Among the wide variety of tubes available in the market, it is possible to find out some models specially designed for low background applications, where the measured uranium and thorium concentrations in quartz and metal components is of the order of tens or a few ppbs [100], giving a yearly production of less than one neutron per PMT. The phototube windows could be coated with Tetra-Phenyl-Butadiene (TPB) to shift the ultra-violet light to the maximum of the phototube spectral response without an increase on contamination. If we assume a rate of 1 neutron per year per PMT and 8 PMTs (6 cm diameter) per cylinder, we expect a total of 8 neutrons per cylinder. In total, PMTs and the copper vessel contribute to 9 neutrons per cylinder per year.

Although they will not be considered in the present study, there are several possibilities to reduce the rate of neutrons coming from PMTs. One is to set acrylic light-guides between photomultipliers and the active volume [100] which can reduce by a factor 2 the rate of neutrons. Another possibility is to substitute the PMTs on the top of the cylinder by charge readout devices, which can be constructed from low radioactivity materials, having a negligible neutron production rate.

We have studied the background rate due to detector components using a simulated sample that amounts to 50 years of data taking. The results shown in tables 4.1 and 4.2 are normalized to one year operation. Table 4.1 corresponds to the configuration where LAr is used. Throughout this chapter, columns labeled as *Total* refer to the total number of neutrons per year, while columns labeled as *Not vetoed* refer to those neutrons not being absorbed in the Gd-doped water tank.

Neutrons	Total	Not vetoed
Produced in 1 year	900	20
30 keV $< E_{visible} <$ 100 keV	56	0.9

Table 4.1: LAr target: Neutron background from detector components normalized to one year of data taking. $E_{visible}$ is the total measured energy in the LAr volume.

After a simple selection cut based on the total measured energy, we find a background of 1 neutron per year for a 1 tonne LAr detector. Considering as signal only those neutrons interacting just once inside the active volume, we cant get rid of some additional background. However given the small dimensions of the targets, we expect a modest reduction factor. It is important to note that when the active Gd-doped veto is used, the amount of background is reduced by roughly a factor fifty. The results using liquid xenon as target are shown in table 4.2. The overall background, after the energy cut, amounts to 3 neutrons per year. The reduction given by the active veto in this case is only a factor ten. Renormalizing to the same active mass, the amount of background for xenon is larger than for argon, the reason being that some xenon isotopes like ^{131}Xe and ^{129}Xe show a very high cross section for neutron absorption. For the case of a xenon-filled detector, the

smaller the dimensions of the target cylinder the better to identify neutrons in the external active veto.

Neutrons	Total	Not vetoed
Produced in 1 year	900	64
15 keV $<$ E$_{visible}$ $<$ 50 keV	34	3

Table 4.2: LXe target: Neutron background from detector components normalized to one year of data taking

4.2.3 Neutrons from surrounding rock

Neutrons coming from the rock have two possible origins: (1) underground production by cosmic muons (called hereafter "muon–induced neutrons") and (2) neutrons induced by spontaneous fission and (α, n) reactions due to uranium and thorium present in the rock (generically called from now on "radioactive"). The latter have a very soft spectrum (typically energies of few MeV). The energy spectrum from muon–induced neutrons is harder. They may come from larger distances and produce recoils with energies well above threshold [100]. The active external water veto will efficiently tag crossing muons by Čerenkov light detection. Neutron signals occurring in the noble liquid target in coincidence with water PMT signals will be rejected. A source of more serious concern are neutrons produced by muon-induced spallation reactions in the walls of the experimental hall, since they will not be efficiently moderated by the water shielding.

Neutrons from radioactivity:

Natural radioactivity can produce neutrons either directly from spontaneous fissions or by means of emitted alphas through (α, n) reactions. To compute the spectrum and the rate of those neutrons, the program SOURCES-4C [101] has been used. The thorium and uranium contamination has been taken as the average of those given in reference [102], namely 18.8 Bq/kg for ^{238}U and 42 Bq/kg for ^{232}Th. Secular equilibrium among them is considered. Accordingly, the computed rates for neutron production amount to 8.44×10^{-8} s^{-1}cm^{-3} from (α, n) reactions and to 7.38×10^{-8} s^{-1}cm^{-3} from spontaneous fission. Neutrons have been generated according to the energy spectrum shown in figure 4.3 and propagated through the rock using the GEANT4 simulation code and the prescriptions given in [100]. As a result we get the neutron spectrum in the walls of the laboratory. To get the final number of neutrons impinging in the detector outer walls and their energy, we have simulated a cavern of $15 \times 12 \times 40$ m^3, similar in dimensions to the experimental main hall at Canfranc underground laboratory [103]. Table 4.3 shows the number of neutrons that reach the liquid argon tanks and those that produce energy deposits in the same range than WIMP interactions. Normalized to one year of data taking, we show the level of expected background for two different distances between the external vessel wall and the first active cylinder a neutron will encounter.

With a 60 cm thick water active veto, the number of interactions inside the liquid argon volume is well below 1 per year. On the other hand, there are $\sim 10^7$ neutron absorptions per year in the water volume. Assuming a 50 μs veto time per interaction, this corresponds to a total of $\sim$ 10 min dead time of the detector per year due to neutron interactions. Since neutrons from rock radioactivity are the most numerous background events in the detector, this value gives an approximation of the total dead time in the experiment. Hence, even in the case that a longer

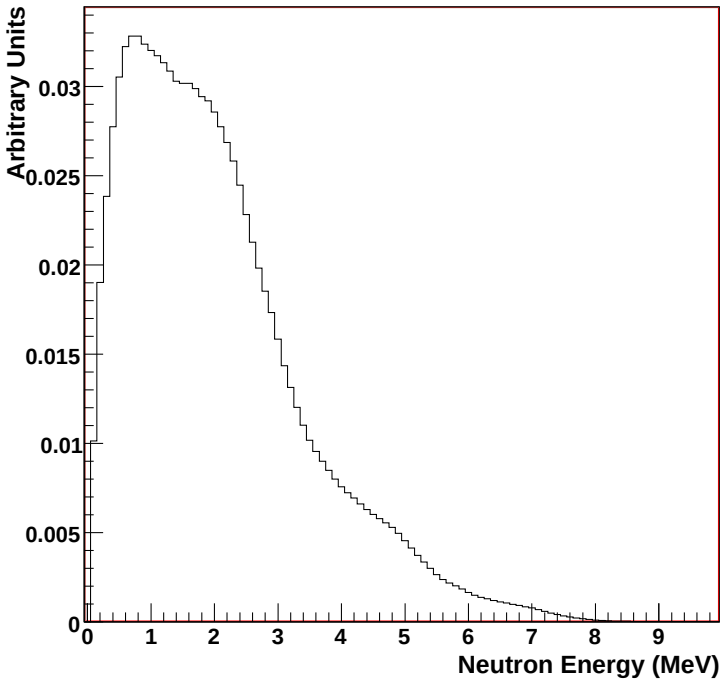

Figure 4.3: Energy spectrum of neutrons produced in the rock by natural radioactivity.

time for coincidence is used, the proposed neutron veto will not limit the acquisition time of the experiment.

The study has been repeated considering a liquid xenon target and 60 cm thick water veto. For this configuration, the expected background from rock radioactivity amounts to two events per year (see table 4.4). In accordance with the results got while studying the contamination due to neutrons from detector components, once more the larger cross section for neutron absorption is responsible for having a bigger expected background when xenon is considered as detector target.

Muon-induced neutrons:

Fast neutrons from cosmic ray muon interactions represent an important background for dark matter searches. Unlike charged particles, they can not be tagged by veto systems, and unlike

Neutrons	40 cm of water		60 cm of water	
	Total	Not vetoed	Total	Not vetoed
Produced in 1 year	3.2×10^7	1.2×10^7	3.2×10^7	1.2×10^7
30 keV$< E_{visible} <$ 100 keV	526	10	26	< 0.1

Table 4.3: Neutron background from rock radioactivity. Results are shown for two different configurations of the active water veto.

Neutrons	Total	Not vetoed
Produced in 1 year	3.2×10^7	1.2×10^7
15 keV$<E_{visible}<$ 50 keV	14	2

Table 4.4: Neutron background from rock radioactivity. A LXe target has been considered together with an active water veto 60 cm thick.

lower energy neutrons from rock radioactivity, they can not be stopped by a passive shielding. However, as proposed in [87], it is possible to place close to the detector some material in which these fast neutrons produce secondary low energy neutrons that can be detected by the proposed veto system when absorbed by Gd.

The total muon-induced neutron flux ϕ_n as a function of the depth for a site with a flat rock overburden can be estimated as [104]:

$$\phi_n = P_0 \left(\frac{P_1}{h}\right) e^{-h/P_1} \tag{4.1}$$

where h is the vertical depth in kilometers water equivalent (km.w.e.), $P_0 = 4.0 \times 10^{-7}$ cm^{-2} s^{-1} and $P_1 = 0.86$ km.w.e.

If we consider a location such as the Canfranc underground laboratory with a depth of ~ 2500 m.w.e. [103], the total neutron flux is 7.52×10^{-9} cm^{-2} s^{-1}. The neutron energy spectrum is given by [105]:

$$\frac{dN}{dE_n} = A \left(\frac{e^{-7E_n}}{E_n} + B(E_\mu) e^{-2E_n}\right) \tag{4.2}$$

and $B(E_\mu) = 0.52 - 0.58e^{-0.0099E_\mu}$, and the muon energy spectrum can be estimated with the following equation [104]:

$$\frac{dN}{dE_\mu} = Ce^{-bh(\gamma_\mu - 1)} \cdot \left(E_\mu + \epsilon_\mu(1 - e^{-bh})\right)^{-\gamma_\mu} \tag{4.3}$$

where A is a normalization constant, E_μ is the muon energy in GeV, $b = 0.4$/km.w.e, $\gamma_\mu = 3.77$ and $\epsilon_\mu = 693$ GeV. The previous equations give rise to the energy spectrum displayed in figure 4.4.

The angular neutron distribution can be expressed as [105]:

$$\frac{dN}{dcos\theta} = \frac{A}{(1 - cos\theta)^{0.6} + B(E_\mu)} \tag{4.4}$$

with $B(E_\mu) = 0.699E_\mu^{-0.136}$.

In order to simulate the fast neutron background, we consider a 10×10 m^2 surface on the detector from which we simulate neutrons with the specified angular and energy distributions. Together with the detector itself, we simulate a lead block in which neutrons will create secondary

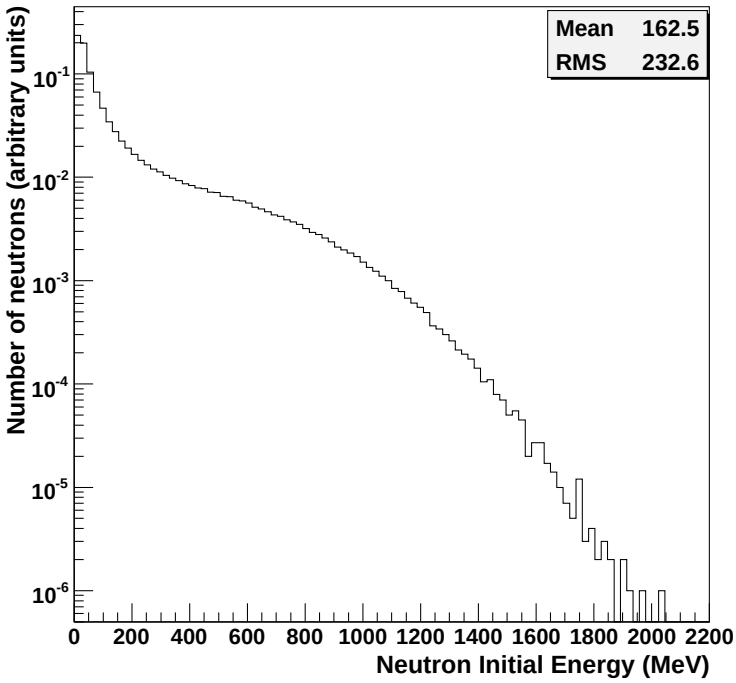

Figure 4.4: Energy spectrum of neutrons produced by muons interacting in the surrounding rock

Neutrons	Total		Not vetoed	
Produced in 1 year	$2.4 \cdot 10^5$		$1.9 \cdot 10^5$	
No lead				
30 keV$<E_{visible}<$ 100 keV	434		66	
Muon veto	43		6	
Lead block (bottom)				
	30 cm	60 cm	30 cm	60 cm
30 keV$<E_{visible}<$ 100 keV	448	448	23	33
Muon veto	45	45	2	3
Lead block (top)				
	30 cm	60 cm	30 cm	60 cm
30 keV$<E_{visible}<$ 100 keV	102	28	12	1
Muon veto	10	3	1	0.1

Table 4.5: Background events coming from cosmic muon-induced neutrons for different LAr detector configuration: a) no additional passive veto; b) an additional passive veto, located either on top or at the bottom of the detector, made of a 30 (60) cm thick lead block.

particles. We have considered two different configurations (lead block on the top or at the bottom of the detector) and two different thicknesses for the passive lead veto.

According to table 4.5, the best configuration corresponds to the case where a 60 cm thick lead block is placed on top of the detector. With this passive veto alone, the background is about thirty events per year, provided the lead block is 60 cm thick. When combined with the Gd-doped water veto, the background drops to one event per year. The simulations have been repeated considering liquid xenon as the target material. Results are shown in table 4.6. Again, the expected background coming from muon-induced neutrons is ∼1 event per year for the whole detector. However, further reduction can be achieved when water itself is considered as an active veto (as shown in tables 4.5 and 4.6, where we refer to it as Muon veto). It has been demonstrated that by rejecting events in coincidence with a muon, the contamination level decreases by a factor 10 [100]. In our case, this means the overall background would be well below 1 event per year per tonne of target material.

Neutrons	Total	Not vetoed
Produced in 1 year	$2.4 \cdot 10^5$	$1.9 \cdot 10^5$
15 keV$<E_{visible}<$ 50 keV	23	2
Muon veto	2	0.2

Table 4.6: Background events coming from cosmic muon-induced neutrons using LXe as target material. We assume that a 60 cm thick lead block is installed on top of the detector.

4.3 Discussion & Summary of the physics performance

Table 4.7 shows that the use of a noble liquid as sensitive target in conjunction with a Gd-doped active water veto efficiently reduces neutron background. According to our simulations, the expected number of neutron-induced contamination is one event per year of data taking for the case of an argon-filled detector and five events for the case of xenon. For an exposure of one tonne×year we can reach sensitivities [106] for the WIMP-nucleon spin-independent cross section close to 10^{-10} pb, as shown in figure 4.5. This represents at least two orders of magnitude improvement with respect to current best limits [41, 107].

	Backgrounds in LAr	Backgrounds in Xe
Detector components	0.9	3.0
Rock radioactivity	<0.1	2
Muon-induced (considering muon-veto)	0.1	0.2
Total in one year	**1.0**	**5.2**

Table 4.7: Expected overall background rate per year in the detector. Note that in the case of LXe the total mass amounts to 2.5 tonnes, while for LAr a 1.2 tonne detector was considered.

The experimental setup we have assessed enhances the probability for neutron capture and its identification, thus providing a much improved rejection tool against this kind of background. Among other virtues, this technique is scalable, therefore allowing the construction of large detectors with fiducial masses in the tonne range or bigger.

We have observed that the use of a Gd-doped veto reduces by about a factor fifty the neutron contamination in case the target is filled with argon and up to a factor ten in case xenon is used.

In case a positive WIMP signal is observed with sufficient statistical power, we can confirm, with a single experiment, that the event rate and the recoil spectral shape follow the expected

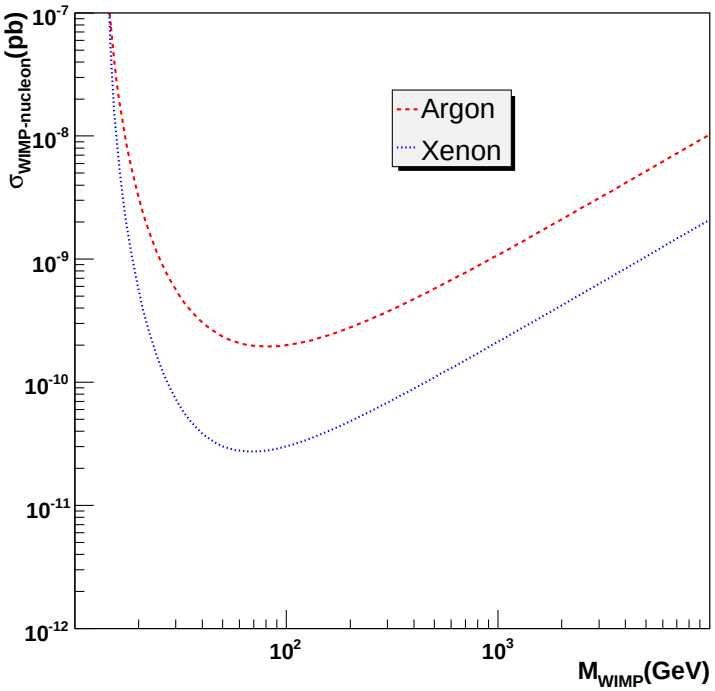

Figure 4.5: Achievable sensitivities for detectors filled with LAr and LXe. The curves have been computed assuming an exposure of one tonne× year in the case of liquid argon and a factor 2.5 bugger in the case of liquid xenon is used. The tool from reference [108] has been used.

dependence on A^2, since the independent target units can be filled with different noble liquids.

A careful simulation of the potential background sources has shown that we expect a contamination of one event per year if liquid argon is used and five events for the liquid xenon configuration. If no WIMP signal is observed, our calculation shows that an exposure of one tonne×year will suffice to exclude spin-independent WIMP-nucleon cross sections in the interval 10^{-10} to 10^{-11} pb.

Chapter 5

Nucleon Decay Searches With Very Massive Underground Liquid Argon TPCs

In previous chapters we have analyzed experiments searching for new physics in which involved energies where in the range of ∼1 keV. This chapter will be devoted to a different physics case, namely the search for nucleon decay. The typical energies for this processes are those of the mass of the nucleon, i.e. ∼1 GeV. During this chapter we will show the versatility of liquid argon TPCs to cover such different ranges of operation and how suitable they are for searches of different sorts of rare events not contemplated within the framework of the Standard Model. We will see how for these events, particle identification based on track topology, dE/dx *versus* range and calorimetry measurements play a much more important role. The ionization charge measurement can be complemented with the recording of scintillation light and with the measurement of Čerenkov light, which is also present for such energetic particles.

Grand Unified Theories require that baryon number is not conserved. The experimental verification of such prediction is one of the most important challenges in Physics today. In the on-going quest for nucleon decay, a new generation of very massive underground detectors has been proposed [109]. Liquid Argon Time Projection Chambers (LAr TPC) appear to be one of the most promising detector options. To assess the potentiality of this detection technology, we take a 100 kton LAr TPC as reference along this chapter. We carry out a detailed simulation of nucleon decays in argon (i.e. including final state nuclear effects). We also simulate and study the contamination due to the two main sources of background: atmospheric neutrinos and cosmic muons. Our study shows that LAr TPC detectors have the potentiality to discover nucleon decay and for some channels in an essentially background-free environment. In this study we also explore a crucial issue for future searches: the possibility to carry out a nucleon decay experiment at shallow depth.

5.1 Introduction

Theories of Grand Unification of fundamental particles and forces predict that protons are unstable [110, 111]. Nucleon decay search is thus an important part of the physics programme of most massive underground detectors, since its discovery would truly have a great impact on our understanding of Nature at higher energy scales than the ones currently reached by accelerators.

Model	Ref.	Modes	τ_N (years)
Minimal $SU(5)$	Georgi, Glashow [111]	$p \to e^+\pi^0$	$10^{30} - 10^{31}$
Minimal SUSY $SU(5)$	Dimopoulos, Georgi [112], Sakai [113] Lifetime Calculations: Hisano, Murayama, Yanagida [114]	$p \to \bar{\nu}K^+$ $n \to \bar{\nu}K^0$	$10^{28} - 10^{34}$
SUGRA $SU(5)$	Nath, Arnowitt [115, 116]	$p \to \bar{\nu}K^+$	$10^{32} - 10^{34}$
SUSY $SO(10)$ with anomalous flavor $U(1)$	Shafi, Tavartkiladze [117]	$p \to \bar{\nu}K^+$ $n \to \bar{\nu}K^0$ $p \to \mu^+K^0$	$10^{32} - 10^{35}$
SUSY $SO(10)$ MSSM (std. $d = 5$)	Lucas, Raby [118], Pati [119]	$p \to \bar{\nu}K^+$	$10^{33} - 10^{34}$
		$n \to \bar{\nu}K^0$	$10^{32} - 10^{33}$
SUSY $SO(10)$ ESSM (std. $d = 5$)	Pati [119]	$p \to \bar{\nu}K^+$	$10^{33} - 10^{34}$ $\lesssim 10^{35}$
SUSY $SO(10)/G(224)$ MSSM or ESSM (new $d = 5$)	Babu, Pati, Wilczek [120, 121, 122], Pati [119]	$p \to \bar{\nu}K^+$	$\lesssim 2 \cdot 10^{34}$
		$p \to \mu^+K^0$	$B \sim (1 - 50)\%$
SUSY $SU(5)$ or $SO(10)$ MSSM ($d = 6$)	Pati [119]	$p \to e^+\pi^0$	$\sim 10^{34.9\pm1}$
Flipped $SU(5)$ in CMSSM	Ellis, Nanopoulos and Wlaker[123]	$p \to e/\mu^+\pi^0$	$10^{35} - 10^{36}$
Split $SU(5)$ SUSY	Arkani-Hamed, *et. al.* [124]	$p \to e^+\pi^0$	$10^{35} - 10^{37}$
Minimal non-SUSY SU(5)	Dorsner, Perez[125]	$p \to \nu + (K^+, \pi^+, \rho^+)$ $n \to \nu + (\pi^0, \rho^0, \eta^0, \omega^0, K^0)$	$10^{31} - 10^{38}$
$SU(5)$ in 5 dimensions	Hebecker, March-Russell[126]	$p \to \mu^+K^0$ $p \to e^+\pi^0$	$10^{34} - 10^{35}$
$SU(5)$ in 5 dimensions option II	Alciati *et.al.*[127]	$p \to \bar{\nu}K^+$	$10^{36} - 10^{39}$
GUT-like models from Type IIA string with D6-branes	Klebanov, Witten[128]	$p \to e^+\pi^0$	$\sim 10^{36}$

Table 5.1: Summary of the expected nucleon lifetime in different theoretical models.

After the first series of experiments (Kolar Gold Mine [129], IMB [130], Kamiokande [131], Soudan [132], etc.), nucleon decay searches are presently in a "second generation" phase. According to the experimental results from Super-Kamiokande [133, 134], the minimal version of SU(5) [111], predicting the decay $p \to e^+\pi^0$ with a lifetime of about 10^{31} years, has been ruled out. The newest result also excluded the minimal SUSY SU(5) [135]. Alternative models, like GUTs with SUSY incorporated, have been proposed offering some hope of observing nucleon decay [136]. These models seem to provide a better unification of the coupling constants, at higher values with respect to minimal SU(5) [137]. The higher unification mass pushes up the proton lifetime in the $p \to e^+\pi^0$ channel up to $10^{36\pm1}$ years, compatible with experimental results and opening, at the same time, alternative decay channels where SUSY intermediate states are concerned and final states involving kaons (like $p \to K^+\bar{\nu}$) are present [121]. Table 5.1 summarizes the main decay modes predicted by different extensions of the Standard Model.

Nucleon decay signals are characterized by (a) their topology and (b) their kinematics. By topology, we mean the presence of an odd number of leptons (electrons, muons or neutrinos) in the final state: in general, few particles (two body decays are believed to be favored) and no other energetic nucleon. The total energy of the event should be close to the nucleon mass. However for nucleon decays occurring in nuclear targets, we expect a smearing from Fermi motion and also other nuclear effects (re-scattering, absorption, etc.).

The search for nucleon decay requires, therefore, (1) excellent tracking and calorimetric resolutions, (2) very massive detectors and (3) an underground location to be shielded against cosmic-ray induced backgrounds. Fine tracking in the low momentum range ($\sim$100 MeV/c) is fundamental for particle identification, (dE/dx) measurement and vertex reconstruction. Concerning the detector mass scale, it is driven by the nucleon lifetime scale. Since there are about 6×10^{32} nucleons per kton of mass, the proton lifetime limit (90% CL) in case of absence of signal and backgrounds is about $\tau_p/\mathrm{B} > \mathrm{M\ (kton)} \times \mathrm{T\ (yr)} \times \epsilon \times 10^{32}$ years, where M is the detector mass, T the exposure, ϵ the signal detection efficiency after cuts, which depends on the considered decay channel, and B is the branching ratio for the considered decay mode. Therefore, the required masses are in the range 100–1000 kton.

In summary, given the variety of predicted decay modes open by the new theories, the ideal detectors should be as versatile as possible, very good in background rejection, and at the same time have the largest possible mass. The relevant factor is in fact $\mathrm{M}\times\epsilon$, hence large masses must be coupled to fine tracking and excellent calorimetry, to suppress backgrounds with a good signal selection efficiency. Furthermore, the detector should be sensitive to several different channels in order to better understand the nucleon decay mechanism.

In this chapter we study the performance of a very massive liquid argon TPC as a nucleon decay detector. In addition, given that the amount of rock overburden and the cost of excavating large deep-underground caverns, able to host such massive detectors, are also crucial issues for next generation experiments, we carefully study the possibility to perform a nucleon decay search at shallow depth.

This chapter is organized as follows: the discussion of the detector configuration assumed and the simulated physics process for signal and background events are described in sections 5.2 and 5.3. The description of the analysis cuts designed to separate, at different underground depths, atmospheric neutrino and muon-induced background events from proton and neutron decay channels are given in section 5.4. Finally, the results obtained in terms of decay limits in case of absence of signal are given in section 5.5.

5.2 A Giant Liquid Argon TPC with charge imaging, scintillation, and Čerenkov light readout

Although the liquid argon TPC technology has been demonstrated to be mature, the possibility to construct a giant argon TPC may not seem possible, at first view, from a technical point of view. In this section we describe some issues that show its feasibility [138].

Up to date, the biggest LAr TPC constructed is the ICARUS T600 detector, with a mass of 600 tons [31]. There are projects for similar modules of up to 5 ktons [139], but however, reaching masses of the order of 100 ktons would require a large number of such supermodules, which would mean a reduced fiducial volume due to modularity and an increase in complexity for the same reason.

A different approach is to build a single giant volume, which would not present the problems pointed above. The maximum possible size would be given by the requirement to locate the

Dewar	$\emptyset \approx$70 m, height$\approx$20 m, passive perlite insulated, heat input$\approx$5 W/m^2
Argon Storage	Boiling argon, low pressure (<100 mb overpressure)
Argon total volume	73118 m^3 (height = 19 m), ratio area/volume $\approx$15%
Argon total mass	102 ktons
Hydrostatic pressure at bottom	$\approx$3 atm
Inner detector dimensions	Disc $\emptyset \approx$70 m located in gas phase above liquid phase
Electron drift in liquid	20 m maximum drift, HV=2 MV for E=1 kV/cm, v_d=2 mm/μs, max drift time $\approx$ 10 ms
Charge readout channels	$\approx$ 10000
Readout electronics	100 racks on top of the dewar (1000 channels per crate)
Scintillation light readout	Yes (also for triggering), 1000 immersed 8" PMT whit wavelength shifter tetraphenyl butadiene (TPB)
Visible light readout	Yes (Čerenkov light), 27000 immersed 8" PMTs or 20% coverage, single photon counting capability

Table 5.2: Summary of parameters of the 100 kton liquid argon detector

detector underground and not by the possibility to build a large cryogenic tanker of the needed size, as such tanks are already present in industry. In this chapter we will explore the potentialities of such a detector installed at different depths.

5.2.1 Overview of the basic design parameter

An artist's view of the detector is shown in figure 5.1. A summary of parameters are listed in table 5.2.

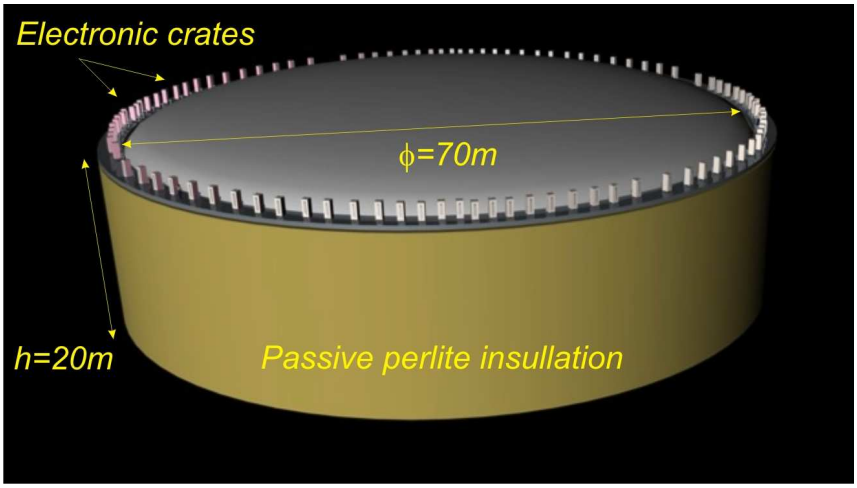

Figure 5.1: Artist's view of a 100 kton single tanker liquid argon detector. The electronic crates are located at the top of the dewar.

The detector can be mechanically subdivided in two parts: the liquid argon tanker and the inner detector instrumentation. We will assume that both parts can be decoupled.

The basic design parameters can be summarized as follows:

1. Single 100 kton "boiling" cryogenic tanker with argon refrigeration.
2. Charge imaging + scintillation + Čerenkov light readout for complete event information.
3. Charge amplification to allow for extremely long drifts: the detector is running in bi-phase mode, i.e., the charge readout is carried out in gaseous argon on top of the detector. In order to allow for long drifts we consider charge attenuation along drift and compensate this effect with charge amplification in the gas phase.
4. Absence of magnetic field.

5.2.2 The 77'000 m^3 liquid argon tanker

To achieve such large volumes of liquid argon, the design is based on the large industrial expertise in the storage of Liquefied Natural Gases (LNG, T$\simeq$110 K at 1 bar). The LNG technology has been developed quite remarkably in the last decades and was driven by the petrochemical and space rocket industries. The technical problems associated to their design, construction and operation have already been addressed and solved by the petrochemical industry. The current state-of-the-art contemplates tankers of 200'000 m^3. Currently there seem to be in the world about 300 giant cryogenic tankers with volumes larger than 30'000 m^3. Large ships transport volumes up to 145'000 m^3 of LNG across the oceans. With all this accumulated experience it does not seem unfeasible the construction of tanker as the proposed one.

5.2.3 The inner detector instrumentation

A schematic layout of the detector is shown in Figure 5.2. The detector is characterized by the extremely large volume of argon. A cathode located near the bottom of the tanker is set at -3 MV, creating a drift electric field of 1kV/cm over a distance of 20 m. In this field configuration ionization electrons are moving upward, while ions are going downward. The electric field is delimited on the sides of the tanker by a series of ring electrodes (race-tracks) put at appropriate voltages. The breakdown voltage of liquid argon is such that a distance of about 50 cm to the ground tanker volume is electrically safe. The high voltage can be obtained through a Cockroft-Walton chain such as that for ArDM discussed in chapter 3.

Regarding charge readout, the tanker will contain both liquid and gas phases. Since purity is a concern for very long drifts of the order of 20 meters, the detector should be operated in bi-phase mode, extracting the electrons from the liquid phase with the help of an electric field of around 3 kV/cm. The extracted charge should be then further amplified, which can be achieved in different ways (e.g., with a LEM). Gains of 100$-$1000 are achievable in this way. If we assume that the reachable electron lifetime is at least $\tau \simeq$2 ms, which has been already obtained by the ICARUS collaboration, then the attenuation factor on 20 m would be of 150, which can hence be compensated at the anode. Also in such long drift distances, it is important to consider the electron cloud diffusion, which would be of approximately 3 mm. Hence, the pitch for readout should not exceed this number.

In addition to charge readout, such a detector will have PMTs around the tanker. Scintillation and Čerenkov light can be read independently. The immersed in liquid argon PMT operation is possible, as has been shown on chapter 2, and any of the models presented there could be used. In order to be sensitive to vacuum ultraviolet scintillation light, some of the PMTs should be coated with TPB.

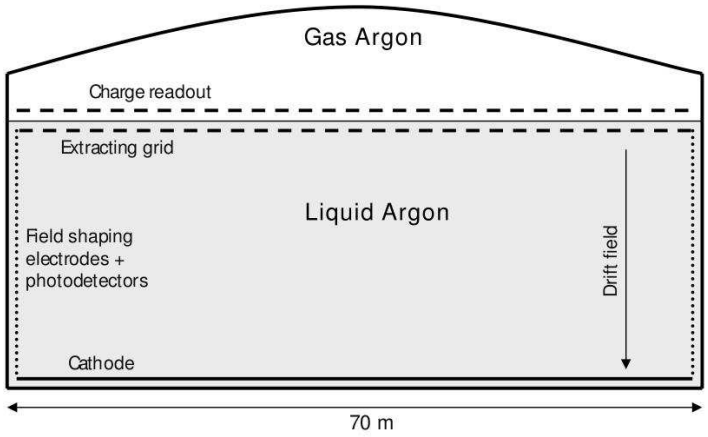

Figure 5.2: Schematic layout of the simulated 100 kton LAr TPC detector (see Ref. [138] for more details).

On the other hand, liquid argon is a great scintillator, but scintillation takes place at 128 nm. Čerenkov light, on the other hand, is much weaker, ∼700 γ/MeV, but is emitted between 160 and 600 nm. It can be separately identified with PMTs without wavelength shifter coating, which would not be sensitive to the scintillation light.

Summarizing, about 1000 phototubes with wavelength shifter would be used to identify the isotropic and bright scintillation light, while about 27000 phototubes without coating would provide a 20% coverage of the surface of the detector. Both of these should have single photon counting capabilities in order to count both the scintillation and Čerenkov photons.

5.3 Physics Simulation

A reliable description of the Physics involved and specially of the expected backgrounds rates is crucial for matter stability studies where a single signal event can evince the presence of nucleon decay. We have performed a detailed simulation of several neutron and proton decay channels. Likewise, the two dominant background sources relevant to our search were simulated: the atmospheric neutrino and the cosmic muon-induced backgrounds.

In what follows, for simplicity, information from Čerenkov and scintillation light will not be considered. However, one should keep in mind that this information will be used in the case of a real experiment.

Background rejection of neutrino events is often based in cuts in energy and momentum of the observed particle. Particles produced in a proton two-body-decay will carry half of the proton energy plus an extra contribution due to the Fermi motion, which can be a total energy of as much as 1 GeV. For a muon, this means a range of ∼5 meters. Their energy and momentum can usually be measured by collecting the total charge deposited in the liquid argon, but this is only possible with events that are fully contained in the instrumented volume. For partially contained events, a precise enough measurement of the track momenta can be obtained by means of the information provided by multiple scattering (see appendix A for further details).

5.3.1 Atmospheric neutrino background

The atmospheric neutrino background is generated using the 3D atmospheric flux obtained with the FLUKA [140] simulation package. The neutrino cross sections and the generation of neutrino interactions is based on the NUX [141] code. This code, benchmarked with the NOMAD [142] experiment data, can be used from kinematical threshold up to neutrino energies in the range of tens of TeV. In order to take into account nuclear effects, a primary nucleon is chosen by FLUKA, a neutrino event is generated on this nucleon, then final state particles are propagated through the nucleus with PEANUT [140]. Table 5.3 reports the total number of generated atmospheric neutrino events per channel. The simulated data sets correspond to a total exposure of 1 megaton×year (10 years of data taking with the detector of section 5.2).

	ν_e **CC**	$\bar{\nu}_e$ **CC**	ν_μ **CC**	$\bar{\nu}_\mu$ **CC**	ν **NC**	$\bar{\nu}$ **NC**
# Events	59861	11707	106884	27273	64705	29612

Table 5.3: Total number of simulated atmospheric neutrino background events in Charged Current (CC) and Neutral Current (NC) channels. They correspond to an exposure of 1 megaton×year.

5.3.2 Cosmic muon-induced background

The second relevant source of background comes from particles produced by cosmic muons interacting on the detector vicinity. We trivially assume that events in which the parent muon enters (before or after the photo-nuclear interaction) the active LAr volume can be discarded thanks to the liquid argon imaging veto. This leads us to restrict the background sources to neutral hadrons and, in particular, to *neutrons*, *neutral kaons* and *lambdas*, produced either directly in muon photo-nuclear interactions or in hadronic showers in the materials surrounding the detector.

The simulation of muon-induced background has been divided into two steps. In the first step we obtained particle fluxes at the detector surface from interactions of cosmic ray muons in the surrounding rock. The cross section of the photo-nuclear interaction of high-energy muons is taken from [143]. The resulting neutron, kaon and lambda spectra have then been used to simulate particle interactions inside the detector. Different detector locations have been considered, since we want to explore the possibility to run an experiment at depths shallower than the ones offered by current underground laboratories. As discussed in section 5.4.3, depths between 0.5 km and 1 km water equivalent (w.e.) (about 200 m and 380 m of standard rock, respectively), provide very competitive experimental sensitivities when compared to other proposed detectors and deeper locations (i.e., 3 km w.e., about 1130 m of standard rock). The option to run at rock overburdens of around 50 to 100 m is disfavoured since the total number of crossing muons is two orders of magnitude bigger than the one expected at 1 km w.e and therefore a large fraction of the argon mass should be wasted in order to have tolerable levels of background.

All simulations are FLUKA based. Validation of the FLUKA models for muon transport and muon photo-nuclear interactions can be found in [144, 105]. It also provides a parameterization of neutron production as a function of the average muon energy and of the average atomic number of materials. We aim here at giving the general trend and the magnitude of the background, while the precise determination of the muon induced background will depend, of course, on many site-specific features like the rock chemical composition, the distribution of rock overburden or the actual material composition/distribution of the LAr container.

The cosmic muon intensity as a function of underground depth is obtained from Crouch's [145] fit to world data. This parameterization agrees to better than 6% with the most recent MACRO

Detector Depth	Neutrons	Kaons
1 km w.e.	$5.5 \cdot 10^5$	$1.3 \cdot 10^3$
3 km w.e.	$1.1 \cdot 10^4$	$2.5 \cdot 10^1$

Table 5.4: Estimated number of neutrons (with kinetic energy above 20 MeV) and neutral kaons entering the detector per year produced in cosmic muon interactions at two depths (hadrons accompanied by a detected muon inside LAr imaging have been vetoed).

measurements [146] at Gran Sasso. Neutral particles have been scored when entering the detector and transported in LAr until they undergo an inelastic interaction. Events in which the parent muon enters the LAr imaging volume are discarded.

Since low energy neutrons are not a background source for nucleon decay searches, we will consider only neutrons with kinetic energy above 20 MeV. The energy-integrated number of particles entering the detector per year of exposure at two particular depths are reported, as an example, in Table 5.4. We simulated $2{\times}10^5$ events for each particle species and used values in the table for normalization. The spatial distribution of photo-nuclear interactions from which at least one neutron enters the detector is plotted in Figure 5.3. Most interactions occur along the detector vertical wall, at an average distance of one meter from it. Among all potential backgrounds, the one of Λs is the rarest in our study. At 3 km w.e. underground it is expected to be around 4% of the corresponding neutral kaon flux. Therefore, no relevant background contribution is expected from it.

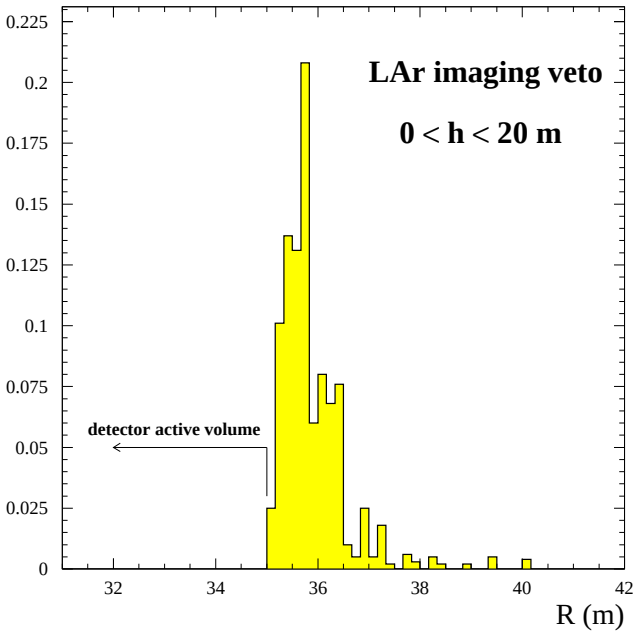

Figure 5.3: Radial distribution of photo-nuclear interaction vertexes producing a neutron that enters the detector at 3 km (w.e.).

5.3.3 Signal simulation

Table 5.4 summarizes the neutron and proton decay channels that have been studied. For each channel, 2000 signal events were generated. An example of a Monte-Carlo generated proton decay event is shown in Figure 5.4. The two photons (from the π^0 decay) and the positron flying on the opposite direction are clearly visible. The event spreads over about 200×70 cm^2. Regardless of the decay mode, the nucleon decay searches largely profit from the clear imaging properties of the LAr TPC technique [31], which allow to unambiguously tag most events. In particular, we will show that low particle detection thresholds are very effective at suppressing atmospheric neutrino events.

Special care has been put on the simulation of *nuclear effects*. Nucleon decay events are characterized by a definite value of the total energy and by the fact that the total momentum of the decay products must be zero. These features, which are true for the decay of a free nucleon, are only approximately verified for a nucleon bound in a nucleus. We have used the FLUKA package to account for nuclear effects. Among those effects, re-interactions in the nuclear medium play an important role. Decay products can lose part of their energy in collisions, or even be absorbed in the same nucleus where they have been created. This is particularly true for pions, that have an important absorption cross section on nucleon pairs (in fact, as we will see later nearly 50% of the $\pi^{+,0}$ are absorbed within the parent argon nucleus). Positive kaons have a very small interaction probability due to the presence of a strange quark.

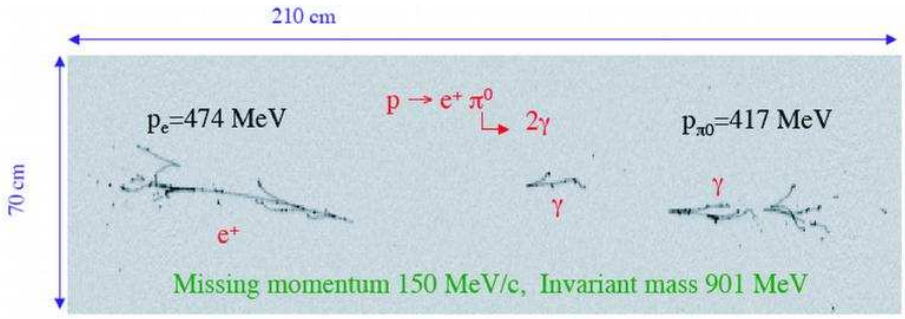

Figure 5.4: Example of a simulated $p \to e^+\pi^0$ event in a LAr TPC.

5.4 Analysis

The approach to discriminate between signal and background is based on a set of sequential selection cuts. Final state topology and event kinematics provide the selection criteria. At first, we ignore the cosmic muon-induced background, and apply cuts until the atmospheric neutrino background can be considered irreducible. The list of studied decay channels in summarized in Table 5.4.

An efficient background reduction demands a good particle identification. Results based on a dedicated analysis show that the tagging efficiency for pions, kaons and protons is above 99% with contamination below 1%. In addition, the muon–pion misidentification is around 40%. The analysis, based on fully-simulated Monte-Carlo events with single particles, combines several variables in a Multi-layer perceptron Neural Network architecture: the χ^2 fit to the particle hypothesis on the $\langle dE/dx\rangle$ vs kinetic energy plane, the fitted particle mass and the energy released after the particle decay. See Figure 1.2 in chapter 1, where it is shown how, thanks to the fine detector granularity,

Decay mode	This analysis(LAr TPC) Efficiency (%)	Atmospheric ν background 100 kton×year	Super-Kamiokande results [133, 135] Efficiency (%)	Atmospheric ν background 92 kton×year	Published limit 90% C.L.
(p1) $p \to e^+ \pi^0$	45.3	0.1	40	0.2	1.6×10^{33}
(p2) $p \to \pi^+ \bar{\nu}$	41.9	78.2			
(p3) $p \to K^+ \bar{\nu}$	96.8	0.1	8.6 (prompt-γ)	0.7	2.3×10^{33}
			6.0 ($K^+ \to \pi^+\pi^0$)	0.6	
(p4) $p \to \mu^+ \pi^0$	44.8	0.8	32	0.2	
(p5) $p \to \mu^+ K^0$	46.7	< 0.2	5.4 ($K^0_S \to \pi^0\pi^0$)	0.4	
			7.0 ($K^0_S \to \pi^+\pi^-$)	3.2	1.3×10^{33}
(p6) $p \to e^+ K^0$	47.0	< 0.2	9.2 ($K^0_S \to \pi^0\pi^0$)	1.1	1.0×10^{33}
			7.9 ($K^0_S \to \pi^+\pi^-$)	3.6	
(p7) $p \to e^+ \gamma$	98.0	< 0.2	73	0.1	
(p8) $p \to \mu^+ \gamma$	98.0	< 0.2	51	0.2	
(p9) $p \to \mu^- \pi^+ K^+$	97.6	0.1			
(p10) $p \to e^+ \pi^+ \pi^-$	18.6	2.5			
(n1) $n \to \pi^0 \bar{\nu}$	45.1	47.4			
(n2) $n \to e^- K^+$	96.0	< 0.2			
(n3) $n \to e^+ \pi^-$	44.4	0.8			
(n4) $n \to \mu^- \pi^+$	44.8	2.6			

Table 5.5: Summary of studied decay modes: signal detection efficiency and expected atmospheric neutrino background (normalized to 100 kton×year exposure) after selection cuts. Where available, the efficiencies and background results of Super-Kamiokande are given for comparison. The published results obtained by Super-Kamiokande are shown for completeness [133, 135].

particles of different species get clearly separated. Electron and photon identification is based on an algorithm that distinguishes single m.i.p. signals versus double m.i.p. signals by using the first hits of each identified electromagnetic track (see figure 5.5).

The list of selection cuts to reduce the atmospheric neutrino contamination, final efficiencies and background estimations for proton and neutron channels are described in sections 5.4.1 and 5.4.2, respectively.

We then evaluate the backgrounds due to cosmogenic events. Our strategy is to reduce the contribution from this background at the level of the irreducible atmospheric neutrino background. The amount of cosmogenic background is strongly correlated with the travel path inside the detector. Thus we will cut on the detector fiducial volume, while keeping the same topology and kinematics criteria used for the neutrino-induced background (in this way, signal selection efficiencies are unaltered). The details on the cosmic muon-induced background estimation are given in Section 5.4.3.

5.4.1 Proton decay channels

The sequential cuts applied for each channel are briefly described in the following paragraphs. The detailed list of cuts for the considered proton decay channels are listed in Table 5.6. Survival

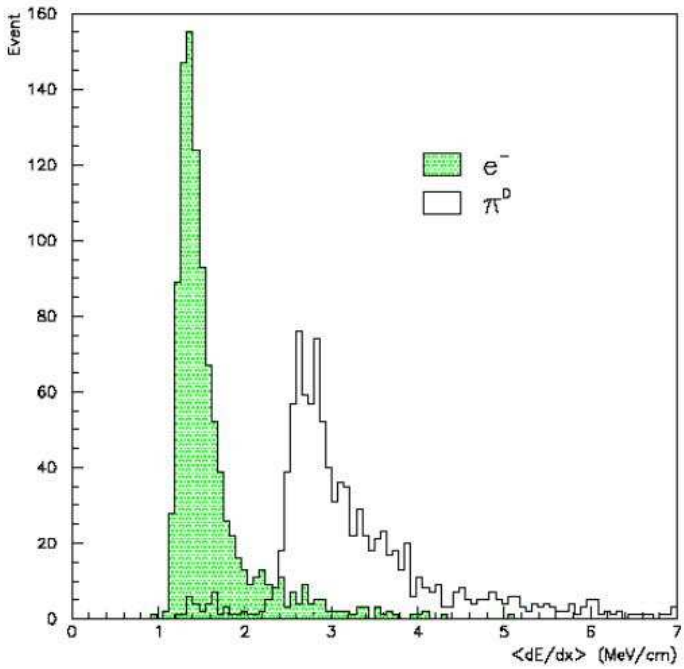

Figure 5.5: dE/dx distribution for photon (from a π^0) and electron events. The highest energy deposition of photons allows for precise identification. Figure taken from [147].

fraction of signal (first column) and background events from the different atmospheric neutrino interactions after selection cuts are applied in succession are also listed. Backgrounds are normalized to an exposure of 1 Mton×year. The final efficiencies and expected background events after cuts are reported in Table 5.4. The published efficiencies, backgrounds and results obtained by Super-Kamiokande are also shown for comparison.

- $p \rightarrow e^+ \pi^0$ channel: A simulated decay event is shown in Figure 5.4. The two photons (from the π^0 decay) and the positron flying in the opposite direction are clearly visible. In the chosen readout view, the event spreads over about 200×70 cm^2. Figure 5.6 shows the distributions of the following reconstructed kinematical quantities: the electron momentum, the total momentum imbalance, the invariant mass and the total energy. The distributions are split into the case where the pion leaves the nucleus (full histograms) and the case where it is absorbed (empty histograms). The electron momentum histogram has an arrow placed at 460 MeV/c, the expected value without Fermi motion and detector effects. It seems clear that two different set of cuts could be implemented to optimize the signal over background ratio in both cases. However, an attempt to look for "inclusive" decays $p \rightarrow e^+(\pi^0)$ without condition on the π^0, yields order of magnitudes worse background conditions, and was not considered further.

  The list of cuts is presented in Table 5.6. The idea is to have a balanced event, with all particles identified as such, and with a total visible energy close to the proton mass (see figure 5.7). Only one background event for 1 Mton×year exposure survives the cuts, for a signal efficiency of about 45%.

	Efficiency (%)	**Atmospheric neutrino sources**					
Cuts	**(p1)** $p \to e^+ \pi^0$	ν_e **CC**	$\bar{\nu}_e$ **CC**	ν_μ **CC**	$\bar{\nu}_\mu$ **CC**	ν **NC**	$\bar{\nu}$ **NC**
One π^0	54.0%	6604	2135	15259	5794	8095	3103
One e-shower + no other charged tracks	50.9%	1188	656	1	0	0	0
$p_{tot} < 0.4$ GeV	46.7%	454	127	0	0	0	0
0.86 GeV $< E_{vis} <$ 0.95 GeV	45.3%	1	0	0	0	0	0
Cuts	**(p2)** $p \to \pi^+ \bar{\nu}$	ν_e **CC**	$\bar{\nu}_e$ **CC**	ν_μ **CC**	$\bar{\nu}_\mu$ **CC**	ν **NC**	$\bar{\nu}$ **NC**
No e-shower, no muons, no π^0	92.6%	0	0	34	0	56515	26482
One charged pion	55.7%	0	0	8	0	5632	2027
No protons	50.0%	0	0	4	0	2930	1136
0.35 GeV $<$ Total E $<$ 0.65 GeV	41.9%	0	0	2	0	605	175
Cuts	**(p3)** $p \to K^+ \bar{\nu}$	ν_e **CC**	$\bar{\nu}_e$ **CC**	ν_μ **CC**	$\bar{\nu}_\mu$ **CC**	ν **NC**	$\bar{\nu}$ **NC**
One kaon	96.8%	308	36	871	146	282	77
No other charged tracks, no π^0	96.8%	0	0	0	0	57	9
$E_{vis} < 0.8$ GeV	96.8%	0	0	0	0	1	0
Cuts	**(p4)** $p \to \mu^+ \pi^0$	ν_e **CC**	$\bar{\nu}_e$ **CC**	ν_μ **CC**	$\bar{\nu}_\mu$ **CC**	ν **NC**	$\bar{\nu}$ **NC**
One muon, one π^0	52.8%	0	0	11334	4452	0	0
No protons, no charged pions	50.0%	0	0	1754	1369	0	0
0.86 GeV $<$ Total E $<$ 0.93 GeV	45.3%	0	0	64	41	0	0
Total Momentum $<$ 0.5 GeV	44.8%	0	0	5	3	0	0
Cuts	**(p5)** $p \to \mu^+ K^0_S$	ν_e **CC**	$\bar{\nu}_e$ **CC**	ν_μ **CC**	$\bar{\nu}_\mu$ **CC**	ν **NC**	$\bar{\nu}$ **NC**
One muon + 2 charged or 2 neutral pions	100%	8178	2771	106861	27274	7099	2540
0.4 $<$ Invariant mass of pions $<$ 0.6 GeV	97%	0	0	5	8	6	2
$p_{tot} < 0.6$ GeV	93.4%	0	0	0	0	0	0
Cuts	**(p6)** $p \to e^+ K^0_S$	ν_e **CC**	$\bar{\nu}_e$ **CC**	ν_μ **CC**	$\bar{\nu}_\mu$ **CC**	ν **NC**	$\bar{\nu}$ **NC**
One e-shower + 2 charged or 2 neutral pions	100%	59759	11673	31	0	2	1
0.4 $<$ Invariant mass of pions $<$ 0.6 GeV	97.0%	2	2	0	0	0	0
$p_{tot} < 0.6$ GeV	94.0%	0	0	0	0	0	0

	Efficiency (%)	**Atmospheric neutrino sources**					
Cuts	**(p7)** $p \to e^+ \gamma$	ν_e **CC**	$\bar{\nu}_e$ **CC**	ν_μ **CC**	$\bar{\nu}_\mu$ **CC**	ν **NC**	$\bar{\nu}$ **NC**
One e-shower + no other charged track	100%	32434	6837	0	0	0	0
Only one photon	99.0%	110	11	0	0	0	0
$p_\gamma > 0.2$ GeV	98.0%	0	0	0	0	0	0
Cuts	**(p8)** $p \to \mu^+ \gamma$	ν_e **CC**	$\bar{\nu}_e$ **CC**	ν_μ **CC**	$\bar{\nu}_\mu$ **CC**	ν **NC**	$\bar{\nu}$ **NC**
One muon + no other charged track	100%	5302	1878	54889	15872	4680	1764
Only one photon	99.0%	7	4	164	13	9	7
$p_\gamma > 0.2$ GeV	98.0%	0	0	0	0	0	0
Cuts	**(p9)** $p \to \mu^- \pi^+ K^+$	ν_e **CC**	$\bar{\nu}_e$ **CC**	ν_μ **CC**	$\bar{\nu}_\mu$ **CC**	ν **NC**	$\bar{\nu}$ **NC**
One Kaon	98.8%	308	36	871	146	282	77
One muon	98.2%	1	0	867	146	0	0
No e-showers	98.2%	0	0	844	145	0	0
0.6 GeV < Total E < 1 GeV	97.6%	0	0	1	0	0	0
Cuts	**(p10)** $p \to e^+ \pi^+ \pi^-$	ν_e **CC**	$\bar{\nu}_e$ **CC**	ν_μ **CC**	$\bar{\nu}_\mu$ **CC**	ν **NC**	$\bar{\nu}$ **NC**
One e-shower, no muons	100%	59755	11673	0	0	0	0
Two charged pions, no protons	19.4%	714	302	0	0	0	0
0.65 GeV < Total E < 1 GeV	19.0%	33	8	0	0	0	0
Total Momentum < 0.57 GeV	18.6%	21	4	0	0	0	0

Table 5.6: Detailed list of cuts for the considered proton decay channels. Survival fraction of signal (first column) and background events through event selections applied in succession. Backgrounds are normalized to an exposure of 1 Mton×year.

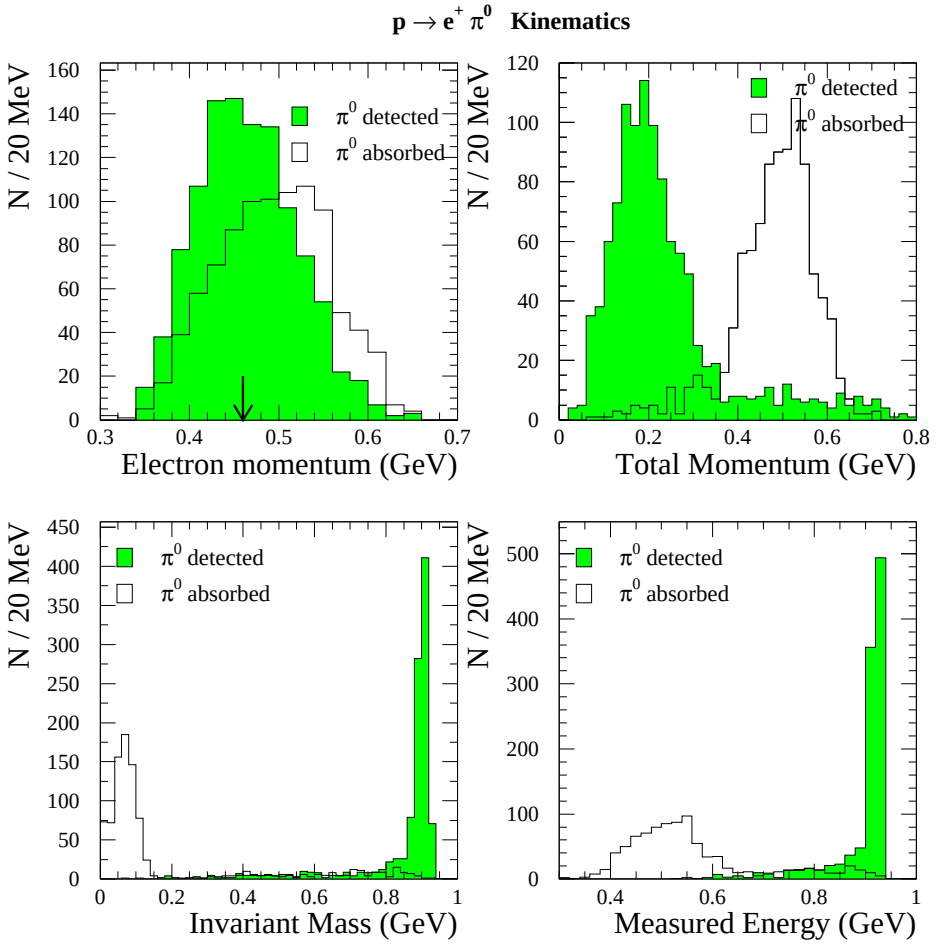

Figure 5.6: $p \to e^+\pi^0$ channel: Distributions of some kinematic variables for the exclusive (full histograms) and the inclusive (empty histograms) scenarios. The arrow in the first plot indicates the value that would have the positron momentum if no Fermi motion and no detector effects were present.

- $p \to \pi^+ \bar{\nu}$ channel: Almost 45% of the events that belong to this channel can not be detected since the π^+ gets absorbed by the nucleus. The cuts are based on the requirement of absence of charged leptons, protons, neutral pions, the presence of one charged pion and a total energy between 350 and 650 MeV. The result is that, for a ∼42% efficiency, the expected background at 1 Mton×year exposure is ∼800 events.

- $p \to K^+ \bar{\nu}$ channel: this is a quite clean channel due to the presence of a strange meson and no other particle in the final state (see Figure 5.8). The kaon particle identification is performed and applying the cuts listed in Table 5.6 yields an efficiency ∼97% for a negligible background. The correlation of the reconstructed invariant mass and total momentum is shown in Figure 5.9.

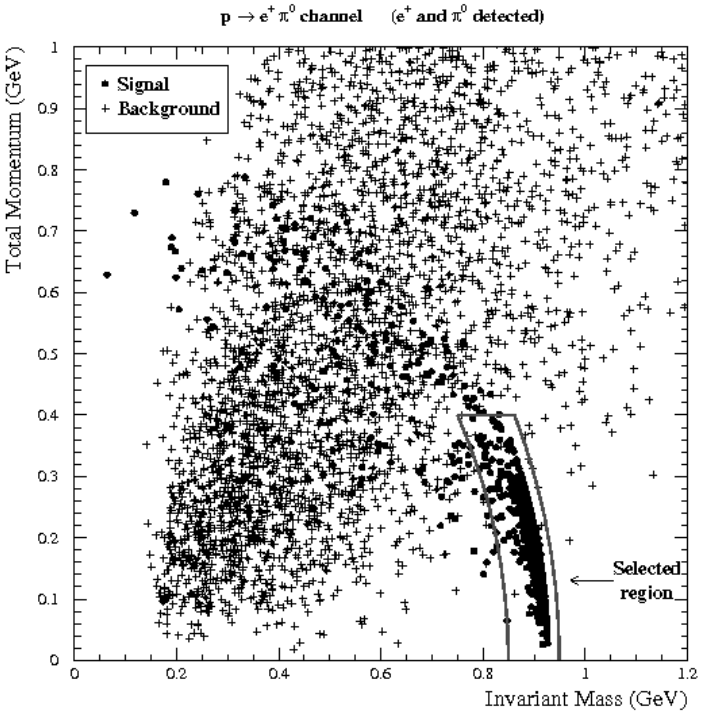

Figure 5.7: Kinematic cut in the $p \to e^+\pi^0$ channel: in the plane defined by the invariant mass and the total momentum, crosses represent background and spots signal events. The band indicates the cut region (0.86 GeV < Total Energy < 0.95 GeV), i.e. all events inside the band are accepted.

- $p \to \mu^+ \pi^0$ channel: Almost 53% of the times the π^0 is detected. In this case, cuts are similar to the $e^+\pi^0$ channel. The efficiency remains high (∼45%), while the background is $\simeq 8$ events for 1 Mton×year.

- $p \to e^+ K^0$ and $p \to \mu^+ K^0$ channels: we concentrate on final states having a K^0_S, since a large fraction of the K^0_L will leave the detector without decaying or will suffer hadronic interactions. In Figure 5.10 simulated events of $p \to e^+ + K^0_S$ and $p \to \mu^+ + K^0_S$ decays are shown, where the K^0_S decays into charged pions. A $p \to \mu^+ + K^0$ decay where K^0 decays into neutral pions is shown in Figure 5.11. A sophisticated treatment to recover K^0_L events has been neglected at this stage. K^0_S's mainly decay to two pions (either charged or neutral). Simple requirements (an identified lepton in the final state accompanied by two charged (neutral) pions, invariant mass of the pion system consistent with the K^0 mass and total momentum below 0.6 GeV) result in a negligible background contamination for signal selection efficiencies above 90% (see Table 5.6). The overall efficiency for the $p \to \mu^+(e^+)\, K^0$ channel is therefore 46.7% (47%).

- $p \to e^+\gamma$ and $p \to \mu^+\gamma$ channels: these channels provide a very clean signal thanks to efficient electron and photon separation (see Ref. [148] for a discussion in the context of e/π^0 separation). The simple final event topology (a single charged lepton accompanied by an energetic photon) allows to reduce the expected background to a negligible level while keeping a signal selection efficiency close to 100% (see Table 5.6). Simulated events of $p \to e^+ + \gamma$

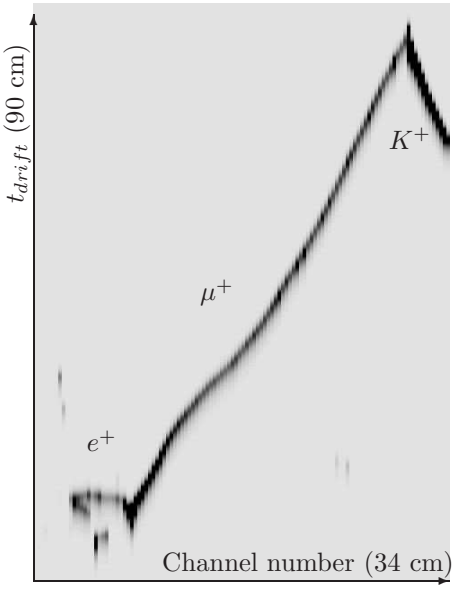

Figure 5.8: Simulated $p \to K^+ \bar{\nu}$ event. The displayed area covers 34×90 cm^2.

decay and $p \to \mu^+ + \gamma$ are shown in Figure 5.12.

- $p \to \mu^- \pi^+ K^+$ channel: by tagging the presence of a K^+ and a μ^-, the background is reduced at the level of ∼1 event for 1 Mton×year exposure. A final cut on the total visible energy removes any background for a signal of $\simeq$ 97%.
- $p \to e^+ \pi^+ \pi^-$ channel: the most favorable scenario occurs when the three particles are detected. A tight cut on the total visible energy ($0.65 < E_{vis} < 1$ GeV) complemented with a cut on the total momentum ($p_{tot} < 570$ MeV/c) are sufficient to reduce the contamination of 25 events for a 1 Mton ×year exposure. On the other hand, the cuts remove less than 1% of the signal events.

5.4.2 Neutron decay channels

The sequential cuts applied for each channel are briefly described in the following paragraphs. The detailed list of cuts for the considered neutron decay channels are listed in Table 5.7. Survival fraction of signal (first column) and background events from the different atmospheric neutrino interactions after selection cuts are applied in succession are also listed. Backgrounds are normalized to an exposure of 1 Mton×year. The final efficiencies and expected background events after cuts are reported in Table 5.4.

- $n \to \pi^0 \bar{\nu}$ channel: about ∼45% of the signal events are "invisible" because the π^0 is absorbed in the nucleus. The rest can be disentangled from the background by cutting on the total visible energy and on the total momentum (>0.35 GeV). The final efficiency is ∼45% for ∼500 background events at 1 Mton×year exposure.
- $n \to e^- K^+$ channel: we profit here from the presence of one kaon, one electron and the absence of muons and pions in the final state. These requirements, together with a loose cut

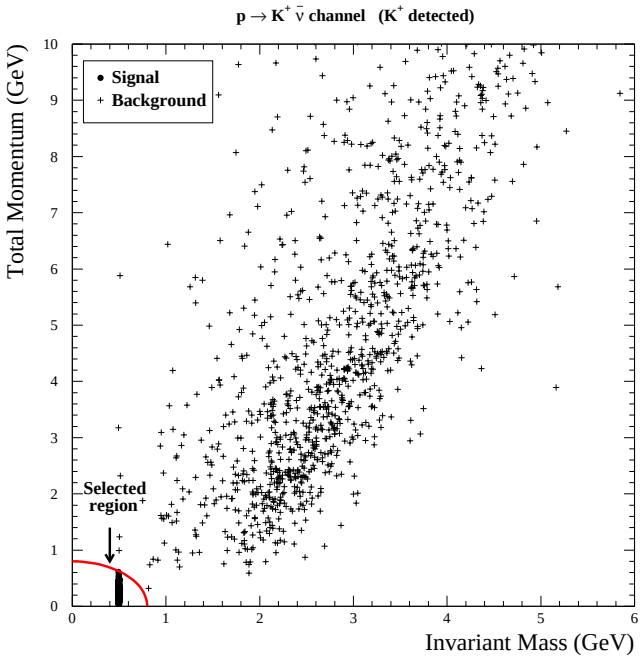

Figure 5.9: Kinematic cut in the $p \to K^+\bar{\nu}$ channel: in the plane defined by the invariant mass and the total momentum, crosses represent background and spots signal events. The band indicates the cut region (Total Energy < 0.8 GeV), i.e. all events in the band are accepted.

on the visible energy ($0.75<E_{vis}<0.95$ GeV), eliminates the background for an almost full detector efficiency.

- $n \to e^+ \pi^-$ channel: this channel is similar to the $p \to e^+ \pi^0$ previously reported. When the π^- is detected, a good efficiency can be reached for a very low background level (8 events in 1 Mton×year) by applying cuts to bound the total energy ($0.75<E_{vis}<1$ GeV), positron momentum ($0.35<p_e<0.6$ GeV) and total momentum ($p_{total} < 0.35$ GeV).

- $n \to \mu^- \pi^+$ channel: this channel is treated in a similar way to the $n \to e^+ \pi^-$. The distribution of the total momentum for signal and background events is shown in Figure 5.13 and the cuts in Table 5.7. We require the presence of a pion on the final state and a cut on the total energy. The plot shows the position of the last cut on total momentum. The final efficiency is ∼45% for the exclusive channel and ∼25 background events for an exposure of 1 Mton×year.

5.4.3 Cosmic muon-induced background estimation

The second source of background we must deal with is the one due to the interactions of cosmic muons inside or around the argon detector. Muons produce secondaries that interact with the argon nuclei or decay in such a way that they mimic a nucleon decay. We study background

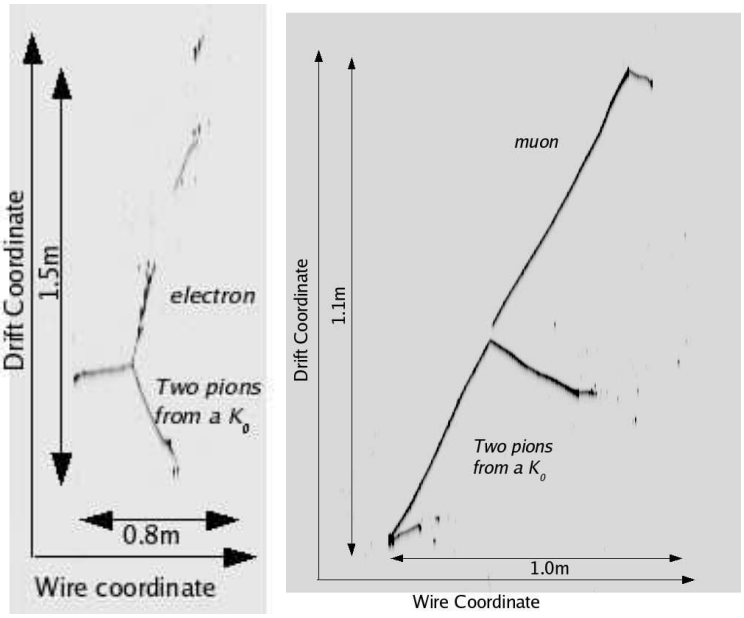

Figure 5.10: Simulated $p \to e^+ + K^0$ (left) and $p \to \mu^+ + K^0$ (right) decays. The neutral kaons decay into two charged pions.

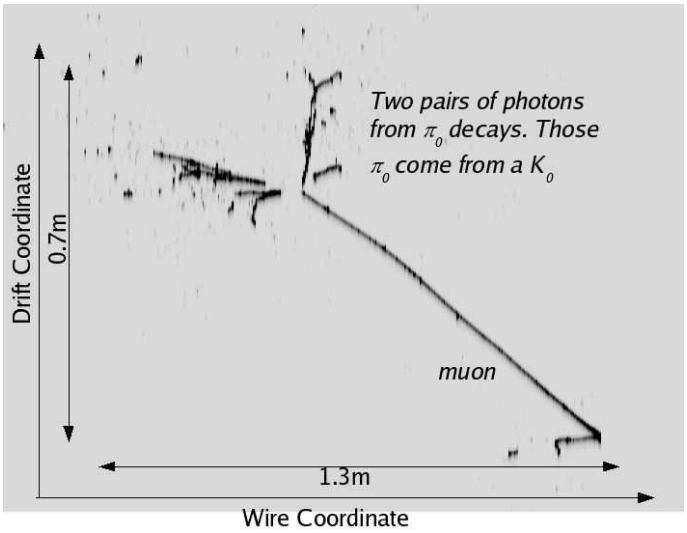

Figure 5.11: Simulated $p \to \mu^+ + K^0$ decay. The neutral kaon decays into two neutral pions.

Cuts	Efficiency (%)	**Atmospheric neutrino sources**					
	(n1) $n \to \pi^0\ \bar{\nu}$	ν_e **CC**	$\bar{\nu}_e$ **CC**	ν_μ **CC**	$\bar{\nu}_\mu$ **CC**	ν **NC**	$\bar{\nu}$ **NC**
One π^0	56.2%	6604	2135	15259	5794	8095	3103
No muons, no electrons, no charged pions	56.1%	0	0	2	0	4722	1840
No protons	52.6%	0	0	0	0	2964	1184
0.35 GeV < Total E < 0.55 GeV	45.4%	0	0	0	0	469	181
$p_{tot} > 0.35$ GeV	45.1%	0	0	0	0	362	112
Cuts	**(n2)** $n \to e^-\ K^+$	ν_e **CC**	$\bar{\nu}_e$ **CC**	ν_μ **CC**	$\bar{\nu}_\mu$ **CC**	ν **NC**	$\bar{\nu}$ **NC**
One e-shower, one kaon	97.0%	299	36	11	0	0	0
No π^0 , no muons	97.0%	138	14	0	0	0	0
No charged pions	97.0%	80	5	0	0	0	0
0.75 GeV < Total E < 0.95 GeV	96.0%	0	0	0	0	0	0
Cuts	**(n3)** $n \to e^+\ \pi^-$	ν_e **CC**	$\bar{\nu}_e$ **CC**	ν_μ **CC**	$\bar{\nu}_\mu$ **CC**	ν **NC**	$\bar{\nu}$ **NC**
One e-shower, one charged pion	59.6%	8137	2755	6	0	0	0
No π^0 , no muons, no protons	57.4%	3855	1282	0	0	0	0
0.75 GeV < Total E < 1 GeV	52.4%	499	187	0	0	0	0
0.35 GeV < $P_{positron}$ < 0.6 GeV	51.3%	216	73	0	0	0	0
$p_{tot} < 0.35$ GeV	44.4%	7	1	0	0	0	0
Cuts	**(n4)** $n \to \mu^-\ \pi^+$	ν_e **CC**	$\bar{\nu}_e$ **CC**	ν_μ **CC**	$\bar{\nu}_\mu$ **CC**	ν **NC**	$\bar{\nu}$ **NC**
One muon, one charged pion	59.4%	1559	454	15931	6569	2291	1055
No π^0, no e-shower, No protons	53.6%	0	0	7830	2924	824	444
0.8 GeV < E_{vis} < 1.05 GeV	49.8%	0	0	1064	408	137	56
$p_{tot} < 0.35$ GeV	44.8%	0	0	18	2	5	1

Table 5.7: Detailed list of cuts for the considered neutron decay channels. Survival fraction of signal (first column) and background events through event selections applied in succession. Backgrounds are normalized to an exposure of 1 Mton×year.

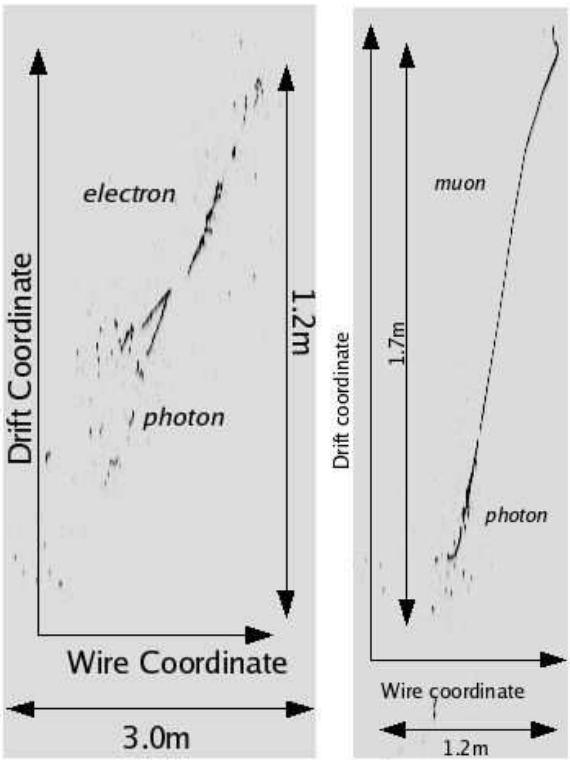

Figure 5.12: Simulated $p \to e^+ + \gamma$ and $p \to \mu^+ + \gamma$ decays.

rates as a function of the detector underground depth from *surface* (50 m of rock overburden) to 3 km w.e., since one of our goals is to study the feasibility of performing a nucleon decay search at shallow depth. The dominant background source corresponds to neutral particles produced by muon photo-nuclear reactions in the material surrounding the sensitive detector volume. The largest flux of neutral particles corresponds to neutrons. Its rate is two orders of magnitude bigger than the one expected from neutral kaons (see Table 5.4). The simulations show that an experiment is not feasible at *surface* and hence, we will not detail the results obtained for this case.

In our analysis, we start applying some kinematic cuts that reject events clearly incompatible with nucleon decay signals. For instance, for the channel $p \to \pi^+ \bar{\nu}$, the expected pion energy in an ideal detector would be 0.48 GeV. We accept charged pions (coming from neutrals produced in muon interactions) with energy in the range 0.35–0.65 GeV, since the measured energy is smeared by Fermi motion and detector effects. In the case of strange mesons, we also require an identified kaon in the final state and a total energy below 0.8 GeV. Table 5.8 summarizes the remaining muon-induced background level after this selection. We find that the $\pi^\pm$ and π^0 backgrounds are predominantly produced by neutrons, and the $K^\pm$ background is dominated by the K^0 entering into the LAr TPC. For some channels we obtain zero events after the final cut, hence an upper limit for these events occurring in the detector is given. The Λ induced background events appeared to be negligible in comparison to the rest and will be ignored hereafter.

As already discussed in section 5.3.2, the photo-nuclear interactions, from which at least one neutral particle enters the detector, occurs mostly at an average distance of one meter from the

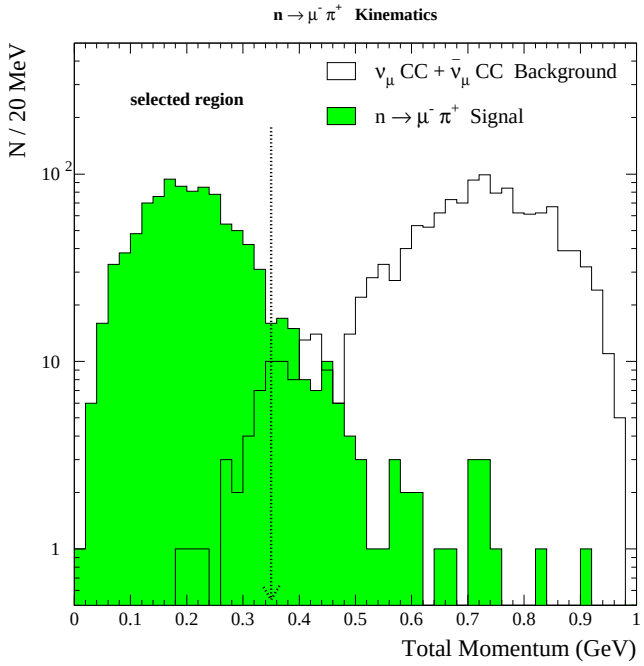

Figure 5.13: $n \to \mu^-\ \pi^+$ channel: distribution of total momentum for events surviving the sixth cut of Table 5.7.

		Background source		
		Neutron	K^0	Λ
1 km w.e.	$\pi^\pm$	$2.0 \cdot 10^2$	$1.3 \cdot 10^{-2}$	$4.7 \cdot 10^{-2}$
	π^0	$1.3 \cdot 10^2$	$< 1.3 \cdot 10^{-2}$	2.3
	$K^\pm$	$< 2.2 \cdot 10^{-3}$	39	$3.6 \cdot 10^{-3}$
3 km w.e.	$\pi^\pm$	4.0	$< 2.5 \cdot 10^{-4}$	$9.0 \cdot 10^{-4}$
	π^0	2.6	$< 2.5 \cdot 10^{-4}$	$4.5 \cdot 10^{-2}$
	$K^\pm$	$< 6.5 \cdot 10^{-5}$	0.74	$7.0 \cdot 10^{-5}$

Table 5.8: Estimated number of background events per year that survive a kinematic selection. We show the contamination due to charged pion, neutral pion and charged kaons coming from neutrons, kaons and lambdas at two different detector depths.

detector walls (see Figure 5.3). Moreover, the number of background events reduces itself exponentially along their path inside the detector. Therefore, an obvious action to reduce background consists on cutting on the sides of the detector, excluding events produced at a distance smaller than d from the wall (see bottom Figure 5.2). The fiducial volume is reduced accordingly. The value for the cut distance d for each detector depth is chosen in such a way that the remaining muon-induced background is of the same order than the expected atmospheric neutrino background. To exemplify the adopted approach, we have chosen two proton decay channels ($p \to K^+\ \bar{\nu}$ and $p \to \pi^+\ \bar{\nu}$) and one neutron decay ($n \to \pi^0\ \bar{\nu}$). Table 5.9 summarizes, for each of the considered

site depths and for the referred channels, the distance cuts applied together with the remaining fiducial weight.

We observe that the background due to charged and neutral pions can be reduced to the same level of expected neutrino-induced backgrounds without a big loss of the detector fiducial mass, even at shallow depth (1 km w.e. or equivalently 380 m of ordinary rock). The rejection of strange mesons requires harder cuts. For a 1 km w.e. depth, a reduction of 30% of the mass is expected. However the prospects for a shallow depth experiment are promising and good sensitivities for most of the analyzed channels are expected for an underground location of 1 km w.e. (see Table 5.10). Similar conclusions hold when a 0.5 km w.e. depth (about 200 m of ordinary rock) is considered. Clearly the situation worsens very much if we consider an experiment running at *surface*. For a 50 m rock depth, the reduction of the pion background requires a waste of more than 30% of the usable argon. The reduction of the kaon background implies that half of the available argon should be wasted. The cosmic muon flux at 50 m depth, and therefore the expected background are so high that an experiment is not feasible at this depth.

Depth	Channel	Background source (particles/year)			Cosmogenic background reduction		
		Neutron	K^0	Λ	Distance cut d (m)	Fiducial mass (kton)	Background (events/year)
$\simeq$0.5 km w.e.	$p \to \pi^+\bar{\nu}$	570	–	–	1.5	92	76
(188 m rock)	$n \to \pi^0\bar{\nu}$	450	–	8	1.7	91	46
	$p \to K^+\bar{\nu}$	–	135	–	6.6	66	0.1
$\simeq$ 1 km w.e.	$p \to \pi^+\bar{\nu}$	200	–	–	0.7	96	77
(377 m rock)	$n \to \pi^0\bar{\nu}$	130	–	2.3	0.75	96	47
	$p \to K^+\bar{\nu}$	–	39	–	5.45	71	0.1
$\simeq$ 3 km w.e.	$p \to \pi^+\bar{\nu}$	4.0	–	–	0	100	4.0
(1.13 km rock)	$n \to \pi^0\bar{\nu}$	2.6	–	–	0	100	2.6
	$p \to K^+\bar{\nu}$	–	0.74	–	1.8	90	0.1

Table 5.9: Cosmogenic background for three selected channels: estimated number of background events per year that survive a kinematic selection. The contamination coming from neutrons, kaons and lambdas interactions at different detector depths are shown. For each detector depth, the radial cut distance and the final fiducial volume to reduce cosmogenic background to the level of the irreducible atmospheric background (resp. 78.2 for $p \to \pi^+\bar{\nu}$, 47.4 for $n \to \pi^0\bar{\nu}$ and 0.1 for $p \to K^+\bar{\nu}$ for an exposure of 100 kton×year) is listed.

5.5 Sensitivity to nucleon decay

In case no signal is observed, limits to proton and neutron partial lifetimes will be obtained using:

$$(\tau/B)_{proton} > \frac{2.69}{S} \times Expo \times \epsilon \times 10^{32} \quad \text{(years)} \tag{5.1}$$

$$(\tau/B)_{neutron} > \frac{3.29}{S} \times Expo \times \epsilon \times 10^{32} \quad \text{(years)} \tag{5.2}$$

Expo is the detector exposure in kilotons per year, ϵ the signal selection efficiency, S the constrained 90% CL upper limit on the number of observed signal events and and B is the branching ratio for

Channel	Efficiency (%)	Total Background	τ/B Limit $\times 10^{34}$ years (90% CL)
$p \to \pi^+ \bar{\nu}$	41.8	(3 km w.e.) 82.2	0.070
		(1 km w.e.) 150.2	0.052
$p \to K^+ \bar{\nu}$	96.7	(3 km w.e.) 0.18	1.017
		(1 km w.e.) 0.14	0.802
$p \to e^+ \pi^0$	45.3	0.1	0.529
$p \to \mu^- \pi^+ K^+$	97.5	0.1	1.140
$p \to e^+ \pi^+ \pi^-$	18.6	1.5	0.108
$p \to \mu^+ \pi^0$	44.8	0.8	0.359
$p \to \mu^+ \gamma$	98.0	0.0	1.146
$p \to e^+ \gamma$	98.0	0.0	1.146
$n \to \pi^0 \bar{\nu}$	45.1	(3 km w.e.) 50.0	0.120
		(1 km w.e.) 91.0	0.086
$n \to e^- K^+$	96.0	0.0	1.370
$n \to e^+ \pi^-$	44.3	0.8	0.435
$n \to \mu^- \pi^+$	44.7	2.4	0.396

Table 5.10: Summary table of the main nucleon decay search results. Figures are given for a total exposure of 100 ktons×year. For each channel, the signal detection efficiency and the total expected background are given together with the limit/Branching Ratio at 90% CL.

the considered decay mode. The numbers 2.69 and 3.29 come from the fact that in 1 kton of argon there are about 2.69 $\times 10^{32}$ protons and 3.29 $\times 10^{32}$ neutrons. S is found by solving the equation:

$$\frac{\sum_{n=0}^{n_0} P(n, b+S)}{\sum_{n=0}^{n_0} P(n, b)} = \alpha \tag{5.3}$$

$P(n, \mu)$ is the Poisson function, b the estimated background, $\alpha = 0.1$ for a 90% CL, and, n_0 is equal to the closest integer number to b when computing the "detector sensitivity".

For each nucleon decay channel we have computed the (τ/B) limits as a function of the exposure. This is done by re-scaling the number of expected background events at each exposure, and computing the corresponding upper limit (S). The result, together with the detection signal efficiency (ϵ), the total expected background and the final detector mass (after fiducial cuts) are reported in Table 5.10. In some instances, the results at two different detector depths are given separately to illustrate the possibility of carrying out a nucleon decay search at shallow depth.

The limits on (τ/B) for proton and neutrons, as a function of the exposure are illustrated on Figure 5.14. We have considered the case where the detector is at a depth of 3000 m water equivalent. The best limits correspond to the exclusive channels. The tag based on the presence of a kaon or a pion accompanied by a charged lepton, with total measured energy around the proton mass is powerful enough to suppress largely the background, while keeping a high signal selection efficiency.

In one year of data taking, a 100 kton LAr TPC would provide limits of the order of 10^{34} years for several proton ($K^+ \bar{\nu}$, $\mu^- \pi^+ K^+$, $e^+ \pi^0$) and neutron ($e^- K^+$, $e^- \pi^0$, $\mu^- \pi^+$) decay modes.

The numbers quoted above are competitive with the results expected for the next generation of Water Čerenkov detectors. For instance, assuming 10 years of data taking, the UNO detector (650 ktons of total mass) would reach a limit of $\sim 10^{35}$ years in the $p \to e^+ \pi^0$ channel ($\epsilon \sim 17\%$) [149], to be compared with 0.5×10^{35} years expected with a 100 kton LAr detector

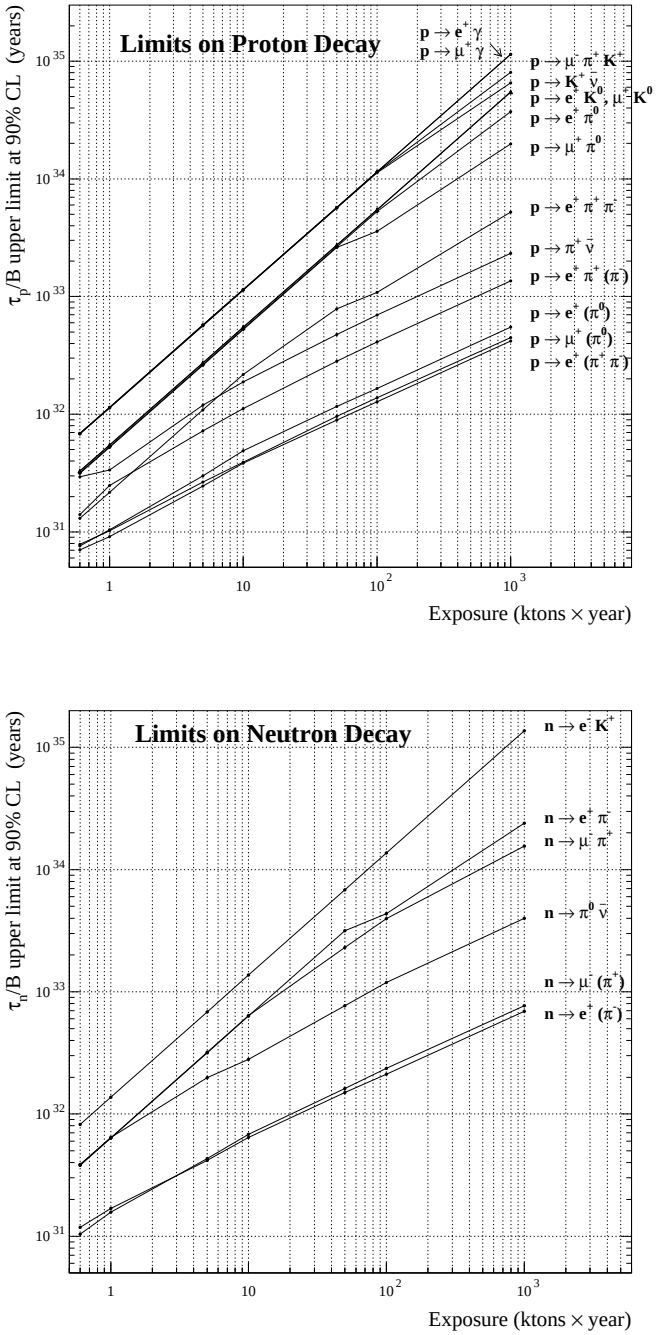

Figure 5.14: Top: Running of the proton decay lifetime limits (τ/B at 90% C.L.) with exposure. Bottom: Running of the neutron decay lifetime limits (τ/B at 90% C.L.) with exposure

($\epsilon\sim$45%). The situation becomes more favorable to the LAr option when analyzing the channels involving more than two particles on the final state ($p \to \mu\pi K$, for instance, where no limits are quoted on UNO) or with the presence of kaons. The expected limits on the $p \to K\nu$ channels are 0.2×10^{35} years for UNO ($\epsilon\sim$9%) and 0.8×10^{35} years for LAr ($\epsilon\sim$97%).

5.6 Conclusions

The question of whether ordinary matter is stable remains unanswered and therefore it stands as one of the most fundamental puzzles in our understanding of Nature. The experimental verification that baryon number conservation is violated at unification scales requires the operation of very massive underground detectors. Large masses must be coupled to fine tracking and excellent calorimetry, to suppress backgrounds with a good signal selection efficiency. Furthermore, the detector should be sensitive to several different channels in order to better understand the nucleon decay mechanism.

In this chapter we have evaluated the discovery potential of a 100 kton liquid argon TPC detector. We have analyzed many possible neutron and proton decay channels. The two main sources of background contamination come from atmospheric neutrinos and cosmic muon-induced particles. The atmospheric neutrino background can be kept under control (below one event per year) in the exclusive analyses whereas it is a non-negligible irreducible contribution in the inclusive channels. The cosmic muon-induced background has been studied at different detector depths and reduced up to the atmospheric ν contribution with fiducial cuts. We have shown that for $\pi^{\pm}$ and π^0 background events, neutrons are the dominant source, whereas the K^0 is the dominant one for $K^{\pm}$ background events. The Λ contribution is found to be negligible. At 50 m overburden of ordinary rock, very tight fiducial cuts are needed in order to reduce the muon-induced background to the level of the one induced by atmospheric neutrinos. Hence most of the argon is not usable and an experiment at this depth is unviable. However at depths of 0.5 km w.e. (about 200 m of ordinary rock) or 1 km.w.e (about 380 m of ordinary rock), we expect good experimental sensitivities after applying loose fiducial cuts to reduce the muon-induced background. Our results show that a nucleon decay search with a LAr TPC at shallow-depth seems feasible.

Table 5.10 summarizes our predictions. Thanks to the good spatial and energy resolution capabilities of the detector, these channels offer the possibility to discover nucleon decay at the one-event level, even at shallow depth (0.5 km.w.e). In case of non observation of a signal, limits close to 10^{35} years for several proton ($K^+\ \bar{\nu}$, $\mu^-\ \pi^+\ K^+$, $e^+\ \pi^0$) and neutron ($e^-\ K^+$) decay channels could be obtained after one year of data taking.

Another advantage with respect to water Čerenkov detectors is that there are channels in which they do not have sensitivity while LAr TPCs do.

In conclusion a 100 kton liquid argon TPC has the potential to discover nucleon decay and provide valuable information about the mechanisms that govern this process, even if the experiment is conducted at shallow depth.

Conclusions

Last generation experiments, in the field of particle and astroparticle physics, have shown overwhelming evidence for the existence of new phenomena not contemplated within the Standard Model. Hence, the search for rare events in new underground experiments is a flourishing activity. These searches cover an energy range spanning from few keVs to several GeVs. As shown in this thesis, liquid argon TPCs have an enormous potential and versatility to make outstanding contributions in these searches for new physics. These innovative detectors are evolved bubble chambers that electronically collect the signals with great spatial resolution, self-triggering capabilities and a very good calorimetric reconstruction.

We have concentrated on the study of the performance of liquid argon TPCs in two different physics scenarios: i) the understanding of the ultimate nature of dark matter; ii) the discovery of whether protons are stable particles or not, as predicted by Grand Unified Theories. The main results of this thesis can be summarized as follows:

- **Dark Matter Searches**
  - The characterization of a series of PMTs immersed in liquid argon has been shown and we have measured the most relevant aspects of their performance. In particular, **a measurement of the quantum efficiency in liquid argon has been done, showing a maximum of ≈20%** [1].
  - In the quest to understand the nature of dark matter, detectors with masses of the order of 1 tonne are needed. In that framework, the ArDM experiment has been constructed and is currently being tested to show its performance. It uses as target medium a liquefied element: argon. **We have shown the first operation of the light acquisition system for the 1 tonne prototype. Light yields of $\sim$ 0.2 pe/keV are achievable in gaseous argon**, which implies for liquid 0.8 pe/keV.
  - An analysis of the neutron backgrounds for dark matter searches has been carried out. We have shown that if a modular detector is combined with an active neutron veto, made of a gadolinium water solution, background rates close to 1 (2) events per year per tonne can be reached in liquid argon (xenon).This means that **after one year of operation, if no WIMP signal is found, we can exclude spin-independent WIMP-nucleon cross sections in the interval** $10^{-10} - 10^{-11}$ [2].
- **Proton decay Searches**
  - We have systematically studied the nucleon decay discovery potential of a 100 kton detector. We have shown that for several proton and neutron decay channels, we can reach, in the absence of a positive signal, **limits on the lifetimes of the lightest barions close to 10^{35} years after one year of data taking** [3].

– **It is possible to conduct a proton decay search experiment at shallow depth**, i.e., underground labs with a rock overburden of 380 m (1 km.w.e.) are adequate locations for such an experiment, since muon-induced and atmospheric neutrino backgrounds can be kept below tolerable levels without sensible loss of detection efficiency and detector fiducial mass.

Appendix A

Momentum measurement via multiple scattering

Liquid argon detectors offer the possibility to measure the momentum of a particle through the charge deposited in the sensitive volume. However, this is not possible for particles that are not fully contained in this volume. An alternative method for momentum measurement comes from the measurement of the deviation angles due to multiple scattering [4]. The central part of the angle distribution can be approximated by a gaussian function, and its RMS is connected with the particle momentum through the equation [150]:

$$\theta_0^{rms} = \frac{13.6\ MeV}{\beta c\, p}\, z \sqrt{\frac{l}{X_0}} \left[1 + 0.038 \cdot ln\left(\frac{l}{X_0}\right)\right] \tag{A.1}$$

where θ_0^{rms} is the width of the Gaussian approximation used for the central 98% of the projected angular distribution. p, β and z are the momentum, velocity and charge of the incident particle. X_0 is the radiation length and l the considered segment length.

Two problems arise when trying to apply this formula:

- A segment length has to be defined. If too long, given the finite track length, the number of entries in the angle distribution will not be enough to get a good estimate of the momentum. On the other hand, if too short, multiple scattering will be completely mimicked by the resolution of the detector.
- The measured angles are the convolution of the multiple scattering and the effect of the detector noise[1], which must be disentangled from the former one to obtain the momentum.

Both problems can be addressed if the momentum is measured using the angle distribution obtained with different segment lengths and fitting these to a function of the momentum and the detector resolution. We will refer to this method as the *classical method*:

$$\theta_{meas}^{rms} = \sqrt{(\theta_0^{rms})^2 \ + \ (\theta_{noise}^{rms})^2} = \sqrt{\left(\frac{13.6\ MeV}{\beta c\, p}\, z \sqrt{\frac{l}{X_0}} \cdot \left[1 + 0.038 \cdot ln\left(\frac{l}{X_0}\right)\right]\right)^2 \ + \ \left(C \cdot l^{-3/2}\right)^2} \tag{A.2}$$

[1]The deviations produced by the detector resolution are inversely proportional to the segment length and to the square root of the number of points and do not depend on the particle momentum: $\theta^{RMS} \propto l^{-1} \times n^{-1/2} \propto l^{-3/2}$

where C is just a proportionality constant for the noise.

We have considered a detector similar to the T600 TPC from the ICARUS collaboration, using wires with 3 mm pitch as charge readout devices. A dedicated MonteCarlo full simulation (including electron diffusion in LAr, signal digitization in the wire planes, etc.) has been used to compute the optimal set of segment lengths for momenta between 250 MeV and 6 GeV, which has been shown to include lengths in the interval [5 cm, 35 cm].

A problem with this technique, is that it includes segments that correspond to different particle momenta, as it loses energy while propagating. The obtained result will be an average of the momentum of the particle along its track.

A.1 The Kalman Filter

There is an alternative approach to the determination of the multiple scattering momentum based on Kalman filter algorithm [151], which is used to deduce an optimum estimate of the past, present or future state of a dynamic system. It uses a time sequence of measurements of the system behaviour, information about its initial condition plus a statistical model that characterizes the system and the measurement errors. It provides a tool to separate random noises from signals in statistical processes.

This algorithm has been used extensively in particle physics since it was first proposed as an alternative solution for track and vertex fitting and to estimate momenta [152]. Typically this technique has been used in association with data provided by magnetized detectors. We now explore the possibility to apply the Kalman Filter algorithm in an homogeneous, non-magnetized environment (the one offered by a LAr TPC) in order to get a measurement of the momentum of charged particles. The particle momentum is extracted from the information provided by the distribution of angles arising from multiple Coulomb scattering process. The Kalman Filter helps to disentangle the noise introduced by the detector resolution. In parallel, it takes into account the energy loss along the track, thus improving the determination of its momentum.

The power of the method lies on the fact that all previous measurements are taken into account to predict the future dynamical behaviour of the system. Therefore, unlike the case of what we called the *classical* approach, where the set of reconstructed track segments is just a collection of unrelated measurements, the Kalman Filter does take correlations into account (in particular, energy losses are automatically included) and therefore we expect, a priori, an improved estimate of both the momentum and its resolution.

A.1.1 The Kalman Filter parameters

The application of the Kalman Filter technique requires the definition of a certain set of vectors and matrices (see [152] for a detailed description of the algorithm concept and the relevant equations). The chosen values throughout our calculation are as follows:

1.- **State Vector:** To make the analysis, the track is split in segments of a certain length, and in each intersection we consider several magnitudes that will conform our state vector. In each of those segments the hits are fitted to a straight line. The parameters of the fit will define the state vector.

In the following, we will consider a three coordinate system, with our particle traveling in the z direction, and being x and y perpendicular to this direction. The state vector will be made of five variables:

- The inverse of the momentum of the particle. This magnitude is related with the angle between the current segment and the next one through the multiple scattering formula (see equation A.1).
- The position of the particle in the plane (two components: x, y).
- The slope of the track in the plane (two components: $\frac{dx}{dz}, \frac{dy}{dz}$).

Hence,

$$\mathbf{x}_k = \begin{pmatrix} \frac{1}{p} \\ x \\ y \\ \frac{dx}{dz} \\ \frac{dy}{dz} \end{pmatrix} \tag{A.3}$$

2.- **Transportation Matrix:** The propagation matrix performs a straight line extrapolation and does not change the slopes, that is, assumes no interaction. The inverse of the momentum is propagated by subtracting from the momentum the energy lost along the segment length E_{lost}. This energy loss can be directly computed from the charge deposited in the wires by the particle along its path.

$$\mathbf{F}_k = \begin{pmatrix} \frac{1}{1-\frac{E_{lost}}{p}} & 0 & 0 & 0 & 0 \\ 0 & 1 & 0 & \Delta z & 0 \\ 0 & 0 & 1 & 0 & \Delta z \\ 0 & 0 & 0 & 1 & 0 \\ 0 & 0 & 0 & 0 & 1 \end{pmatrix} \tag{A.4}$$

3.- **Measurement Vector and Matrix:** The measurement vector is similar to the state vector. The only difference is in the first row, as momentum can not be measured directly. The measured magnitude is instead the angle difference between the incoming and outgoing trajectories, that is related with the momentum through equation A.1. This difference is taken into account in the measurement matrix, and hence, measurement vector and measurement matrix are given by:

$$\mathbf{m}_k = \begin{pmatrix} \theta_0 \\ x \\ y \\ \frac{dx}{dz} \\ \frac{dy}{dz} \end{pmatrix}, \quad \mathbf{H}_k = \begin{pmatrix} K & & & & \\ & 1 & & & \\ & & 1 & & \\ & & & 1 & \\ & & & & 1 \end{pmatrix} \tag{A.5}$$

Where K is the multiple scattering constant factor that multiplies $\frac{1}{p}$ in equation A.1.

4.- **Covariance Matrices:** The last ingredient for the method is the choice of the covariance matrices. The covariance matrix for the system noise has been taken from reference [153]

where the authors derive, in a simple and intuitive way, the track parameter covariance matrix due to multiple scattering. They obtain all the matrix elements for two experimentally relevant track parameterizations, being the first of them the one we are using: x and y slopes and intercepts.

In the covariance matrix for the detector noise, we have considered no correlations between the components of the state vector, and hence the matrix is diagonal. The value for each point is just the measurement error.

An initial state must be supplied for the method to work. It can be thought, a priori, that the input guess for the initial momentum is an important choice that may influence the final value of the momentum measurement. In practice this is avoided by giving a big enough error to the momentum in the first plane, such that its value becomes irrelevant. This has been tested by carrying out a Kalman Filter with a random initial state as input. The obtained momentum, close to the real one, was used as input for a second Kalman Filter. The final momentum does not differ significantly from the value used as input.

The only important choice for the method is the segment length to be used in the analysis. This must be as short as possible in order to guarantee a large enough number of points, but at the same time segments must be long enough in order to allow multiple scattering effects to emerge over the detector noise. Hence a compromise must be reached.

A priori, the most ambitious idea would be to consider just single hits, as in this way all the information is taken into account and no average is done. But when the segment length is too short, the noise in the measurements is too high, hiding multiple scattering effects. Therefore the momentum can not be properly estimated. We have seen that to optimize our results it is advisable to use three different segment lengths for each track. For particles in the studied energy range, between 0.25 and 3 GeV, we have considered segment lengths of 10, 12.5 and 15 cm. The final momentum value is obtained by averaging the momentum computed for each of the selected segment lengths.

A.2 Comparison between the *classical* method and the Kalman Filter

Both algorithms have been programed and tested in a dedicated MonteCarlo simulation using muons generated with the FLUKA package with energies in the range from 250 MeV up to 3 GeV. Figure A.1 shows the results for momentum measurement and momentum resolution obtained with the *classical* method and the Kalman filter.

On the left part of the figure, where a straight line indicates the ideal $p_{meas} = p_{MC}$ scenario, we see that the points from the *classical* analysis are clearly below the line because of the energy lost by the muon along its path. The Kalman Filter gives a much better estimation, since it takes into account energy losses.

The right part of the figure shows the momentum resolution. For the *classical* approach it is on the range 25–20 %. There is an increase of the resolution at the edges: for small momenta, where the range of lengths and the number of segments is small, and for high momenta, where the effect of the multiple scattering decreases. With the Kalman Filter technique, the resolutions are around 15% for the whole range of studied momenta, except at 250 MeV where the resolution is close to 25%, due to the short track lengths involved[2].

[2] A 250 MeV muon has a typical length of less than 1 meter in liquid argon.

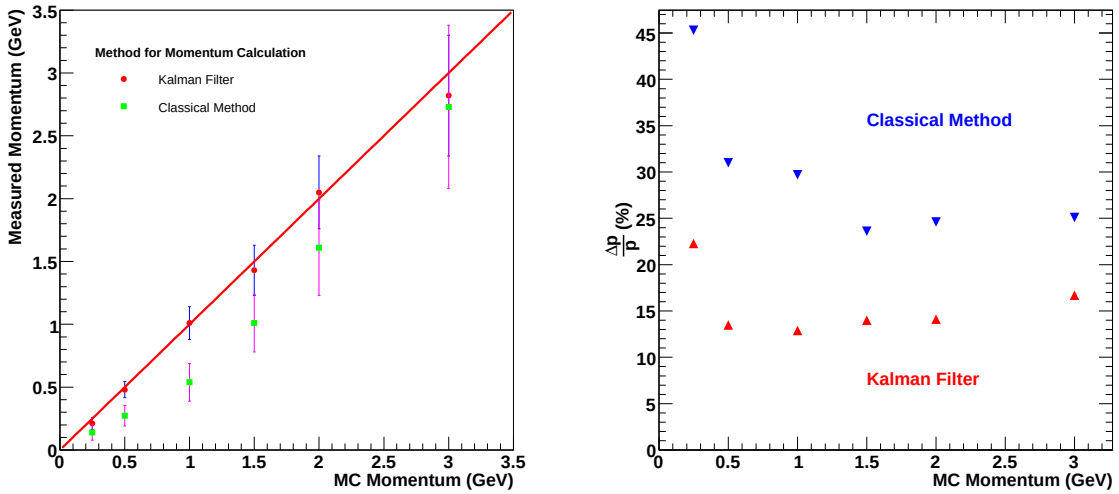

Figure A.1: Left: Comparison between the calibration curves for *classical* and Kalman Filter methods. The solid line shows the case where $P_{measured} = P_{MonteCarlo}$. Right: Comparison between the resolutions for *classical* and Kalman Filter methods.

A.3 Kalman Filter application to a set of stopping atmospheric muons

An extra confirmation of the good performance of the Kalman filter algorithm for momentum measurement can be obtained through its application to a real set of data. The sample we take as reference corresponds to a set of stopping atmospheric muons collected on the summer of 2001 during a technical run on surface of the T600 detector from the ICARUS experiment [31]. The initial set, the 2690 events used in [154], is reduced to a sample of 1009 muons when a minimal length and a minimal number of charge depositions in the detector TPC are imposed. Given the characteristics of the selected muons, the range of considered momenta spans from about 200 MeV up to 800 MeV (being the mean value 400 MeV). For higher momenta, the sample of recorded muons is not statistically significant. The MonteCarlo tells us that the Kalman Filter performance for the lower momentum range is not as good as the one expected for muons above 1 GeV. However a demonstration that the method performs reasonably well in the low momentum range, will give us confidence on the fact that the algorithm can be also applied at higher momenta.

Being fully contained, the momentum of those muons can be very accurately measured using a calorimetric approach. When computing momentum by means of calorimetry, recombination effects should be taken into account. Equation A.6 relates measured and deposited charges:

$$Q_{meas} = R \cdot Q_{dep} \cdot e^{\frac{t-t_0}{\tau}} \tag{A.6}$$

R is the recombination factor and we use the value $R = 0.71$ [155]. τ stands for the drift mean life of the electrons and and its value is taken from [9] for each of the selected events. The error associated to τ is propagated to the momentum measured by calorimetry. It amounts to less than five per cent.

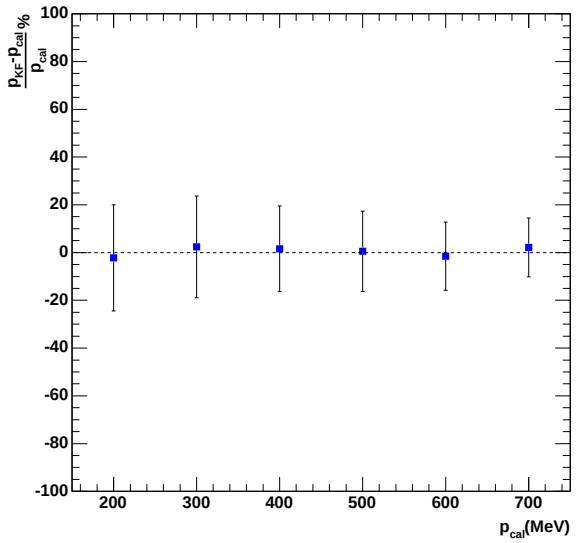

Figure A.2: Dispersion of the Kalman Filter measurements (p_{KF}) with respect to the momentum measured by calorimetry, (p_{cal}). The filled squares represent the mean value of the dispersion distribution. The error bars correspond to the RMS.

In our study we consider the momentum measured by calorimetry, p_{cal}, as the *true* momentum value. On a track by track basis, we compare the momentum obtained with the Kalman Filter, p_{KF}, to p_{cal}. The results, plotted in figure A.2, show that for each of the six momentum bins into which we group the data, the mean dispersion is close to zero. The error bars correspond to the RMS of each individual distribution. For the lowest momenta, the error is around 20%. As the momentum increases, the error bar diminishes reaching a minimum value of about 12%. These results are in very good agreement with the resolutions obtained, for the low momentum range, in our MonteCarlo simulation (see figure A.1). In view of these results, we conclude that real data confirm the fact that the Kalman Filter algorithm, when combined with multiple Coulomb scattering information, is an optimal method to obtain an accurate measurement of partially contained track momenta.

List of Figures

List of Tables

Bibliography

[1] Bueno, A., Melgarejo, A. J., Navas, S *et al.*, *Characterization of large area photomultipliers and its application to dark matter search with noble liquid detectors*, *JINST* **3** (2008) P01006, [physics.ins-det/0711.3592].

[2] Bueno, A., Carmona, M. C. and Melgarejo, A. J., *Direct dark matter identification with a hybrid detection technique*, astro-ph/0805.0694.

[3] Bueno, A., Melgarejo, A. J., Navas, S *et al.*, *Nucleon decay searches with large liquid argon TPC detectors at shallow depths: Atmospheric neutrinos and cosmogenic backgrounds*, *JHEP* **04** (2007) 041, [hep-ph/0701101].

[4] **ICARUS** Collaboration, Ankowski, A., Melgarejo, A. J. *et al.*, *Measurement of through-going particle momentum by means of multiple scattering with the ICARUS T600 TPC*, *Eur. Phys. J.* **C48** (2006) 667, [hep-ex/0606006].

[5] **Liquid Argon Back End Electronics** Collaboration, Bazan, A. *et al.*, *ATLAS liquid argon calorimeter back end electronics*, *JINST* **2** (2007) P06002.

[6] Alon, R. *et al.*, *Operation of a thick gas electron multiplier (THGEM) in Ar, Xe and Ar-Xe*, *JINST* **3** (2008) P01005.

[7] Walkowiak, W., *Drift velocity of free electrons in liquid argon*, *Nucl. Instrum. Meth.* **A449** (2000) 288.

[8] Navas, S. *et al.*, *A measurement of the drift velocity in the T600 data*, *ICARUS-TM/02-01* (2002).

[9] **ICARUS** Collaboration, Amoruso, S. *et al.*, *Analysis of the liquid argon purity in the ICARUS T600 TPC*, *Nucl. Instrum. Meth.* **A516** (2004) 68.

[10] Doke, T., *Fundamental properties of liquid argon, krypton and xenon as radiation detector media*, *Portgal. Phys.* **12** (1981) 9.

[11] Antonello, M. *et al.*, *Analysis of Liquid Argon Scintillation Light signals with the ICARUS T600 detector*, *ICARUS-TM/06-03* (2006).

[12] Miyajima, M. *et al.*, *Average energy expended per ion pair in liquid argon*, *Phys. Rev. A* **9** (1974), no. 3 1438.

[13] Cennini, P. *et al.*, *Detection of scintillation light in coincidence with ionizing tracks in a liquid argon time projection chamber*, *Nucl. Instr. Meth.* **A432** (1999) 240.

[14] Grosjean, D. E. *et al.*, *Absolute luminescence efficiency of ion-bombarded solid argon*, *Phys. Rev. B* **56** (1997) 6975.

[15] Doke, T. *et al.*, *LET dependence of scintillation yields in liquid argon*, *Nucl. Instrum. Meth.* **A269** (1988) 291.

[16] Kubota, S. *et al.*, *Recombination luminescence in liquid argon and in liquid xenon*, *Phys. Rev. B* **17** (1978), no. 6 2762.

[17] Hitachi, A. *et al.*, *Effect of ionization density on the time dependence of luminescence from liquid argon and xenon*, *Phys. Rev. B* **27** (1983), no. 9 5279.

[18] **WARP** Collaboration, Brunetti, R. *et al.*, *WARP liquid Argon detector for dark matter survey*, *New Astron. Review* **49** (2005) 265.

[19] Ishida, N. *et al.*, *Attenuation length measurements of scintillation light in liquid rare gases and their mixtures using an improved reflection suppresser*, *Nucl. Instrum. Meth.* **A384** (1997) 380.

[20] Landau, L.D. and Lifshitz, E.M., *Electrodynamics of contiuous media*. Pergamon Press, 2rd ed., 1984.

[21] Geidel, G. M. and Lanou, R. E. and Yao, W., *Rayleigh scattering in rare-gas liquids*, *Nucl. Instrum. Meth.* **A489** (2002) 189, [hep-ex/0111054].

[22] Bueno, A. and Navas, S., *Random Forest And Neural Network Classification Algorithms Applied To Particle Identification*, *ICARUS-TM/05-01* (2005).

[23] Glaser, D. A., *Some Effects of Ionizing Radiation on the Formation of Bubbles in Liquids*, *Phys. Rev.* **87** (1952) 665.

[24] Glaser, D. A., *Bubble Chamber Tracks of Penetrating Cosmic-Ray Particles*, *Phys. Rev.* **91** (1953) 762.

[25] Bunemann, O., Cranshaw T. E. and Harvey J. A., *Design of Grid Ionization Chambers*, *Can. J. Res.* **27** (1949) 191.

[26] **ArDM** Collaboration, Laffranchi, M. and Rubbia, A., *The ArDM project: A liquid argon TPC for dark matter detection*, hep-ph/0702080.

[27] Rubbia, C., *The Liquid-Argon Time Projection Chamber: A New Concept For Neutrino Detector*, *CERN-EP/77-08* (1977).

[28] **ICARUS** Collaboration, Cennini, P. *et al.*, *Performance of a 3-ton liquid argon time projection chamber*, *Nucl. Instr. Meth.* **A345** (1994) 230.

[29] **ICARUS-Milano** Collaboration, Arneodo, F. *et al.*, *Performance of a liquid argon time projection chamber exposed to the WANF neutrino beam*, *Phys. Rev.* **D74** (2006) 112001, [physics/0609205].

[30] Martínez de la Ossa, A., *Study of Accelerator Neutrino Interactions in a Liquid Argon TPC*, *PhD. Thesis* (2007) [hep-ex/0703026].

[31] **ICARUS** Collaboration, Amerio, S. *et al.*, *Design, construction and tests of the ICARUS T600 detector*, *Nucl. Instr. Meth.* **A527** (2004) 329.

[32] Marchionni, A., *Challenge to Realize Huge Underground Detector -Liquid Ar TPC Case-*, *talk at The 4th International Workshop on Nuclear and Particle Physics at J-PARC (NP08)* (March 2008, Mito, Ibaraki, Japan.).

[33] Benetti, P. *et al.*, *First results from a dark matter search with liquid argon at 87-K in the Gran Sasso underground laboratory*, *Astropart. Phys.* **28** (2008) 495, [astro-ph/0701286].

[34] Bennetti, P. *et al.*, *The ICARUS R&D program and results*, *Nucl. Instr. Meth.* **A327** (1993) 173.

[35] Bennetti, P. *et al.*, *A 3 ton liquid argon time projection chamber*, *Nucl. Instr. Meth.* **A332** (1993) 395.

[36] **ICARUS** Collaboration, Cennini, P. *et al.*, *A 3-D image chamber for the liquid argon TPC based on multi-layer printed circuit board*, *Nucl. Instr. Meth.* **A346** (1994) 550.

[37] Buckley, E. *et al.*, *A study of ionization electrons drifting over large distances in liquid argon*, *Nucl. Instr. Meth. Phys. Res.* **A275** (1989) 364.

[38] Bettini, E. *et al.*, *A Study of the factors affecting the electron lifetime in ultrapure liquid argon*, *Nucl. Instr. Meth.* **A305** (1991) 177.

[39] Acciarri, R. *et al.*, *Oxygen contamination in liquid Argon: combined effects on ionization electron charge and scintillation light*, nucl-ex/0804.1222.

[40] Hitachi, A. *et al.*, *Scintillation and ionization yield for α particles and fission fragments in liquid argon*, *Phys. Rev. A* **35** (1987) 3956.

[41] **XENON** Collaboration, Angle, J. *et al.*, *First Results from the XENON10 Dark Matter Experiment at the Gran Sasso National Laboratory*, *Phys. Rev. Lett.* **100** (2008) 021303, [arXiv/0706.0039].

[42] Kubota, S., Hishida, M. and Raun, J., *Evidence for a triplet state of the self-trapped exciton states in liquid argon, krypton and xenon*, *J. Phys. C* **11** (1978) 2645.

[43] Rubbia, A., *ArDM: A ton-scale liquid argon experiment for direct detection of dark matter in the universe*, *J. Phys. Conf. Ser.* **39** (2006) 129, [hep-ph/0510320].

[44] *Photomultiplier Tubes: Basics and Application.* Hamamatsu Photonics K.K., 3rd ed., 2007.

[45] Ostankov, A. *et al.*, *A study of the new hemispherical 6-dynodes PMT from electron tubes*, *Nucl. Instrum. Meth. A* **442** (2000) 117.

[46] Spicer, W. E. and Wooten, F., *Photoemission and photomultipliers*, *Proceedings of the IEEE* **51** (1963), no. 8 1119.

[47] Ankowski, A. *et al.*, *Characterization Of Etl 9357FLA Photomultiplier Tubes For Cryogenic Temperature Applications*, *Nucl. Instrum. Meth. A* **556** (2006) 146.

[48] "Electron tubes enterprises limited, http://www.electrontubes.com."

[49] "Hamamatsu photonics k.k., http://www.hamamatsu.com."

[50] "Cryocircuits, http://www.cryocircuits.com/."

[51] "Newport oriel instruments, http://www.newport.com/oriel."

[52] "Spectral products, http://www.spectralproducts.com."

[53] "Edmund optics, http://www.edmundoptics.com."

[54] "Keithley, http://www.keithley.com."

[55] "Labview, http://www.ni.com/labview/."

[56] "Ocean optics, http://www.oceanoptics.com."

[57] Araujo, H. M. *et al.*, *Study of bialkali photocathodes below room temperature in the UV/VUV region*, *IEEE Trans. Nucl. Sci.* **NS-45** (1998), no. 3 542.

[58] Singh, A. S. and Wright, A. G., *The determination of photomultiplier temperature coefficients for gain and spectral sensitivity using the photon counting technique*, *IEEE Trans. Nucl. Sci.* **NS-34** (1987) 434.

[59] "Caen, http://www.caen.it."

[60] Dossi, R. *et al.*, *Methods for precise photoelectron counting with photomultipliers*, *Nucl. Instrum. Meth. A* **451** (2000) 623.

[61] Gaitskell, R. J., *Direct detection of dark matter*, *Ann. Rev. Nucl. Part. Sci.* **54** (2004) 315.

[62] Battaner, E. and Florido, E., *The rotation curve of spiral galaxies and its cosmological implications*, *Fund. Cosmic Phys.* **21** (2000) 1, [astro-ph/0010475].

[63] Tegmark, M. *et al.*, *Cosmological Constraints from the SDSS Luminous Red Galaxies*, *Phys. Rev. D* **74** (2006) 123507.

[64] **WMAP** Collaboration, E. Komatsu *et al.*, *Five-Year Wilkinson Microwave Anisotropy Probe WMAP Observations:Cosmological Interpretation*, astro-ph/0803.0547.

[65] Clowe, D. *et al.*, *A direct empirical proof of the existence of dark matter*, *Astrophys. J.* **648** (2006) L109.

[66] Bradac, M. *et al.*, *Strong and weak lensing united. 3. Measuring the mass distribution of the merging galaxy cluster 1E0657-56*, *Astrophys. J.* **652** (2006) 937.

[67] Sanders, R. H. and McGaugh, S. S., *Modified Newtonian dynamics as an alternative to dark matter*, *Ann. Rev. Astron. Astrophys.* **40** (2002) 263.

[68] Bertone, G., Hooper, D. and Silk, J., *Particle dark matter: Evidence, candidates and constraints*, *Phys. Rept.* **405** (2005) 279.

[69] **Particle Data Group** Collaboration, Yao, W. M. *et al.*, *Review of particle physics*, *J. Phys.* **G33** (2006) 1. Available on the PDG WWW pages http://pdg.lbl.gov/2007/reviews/darkmatrpp.pdf.

[70] Lewin, J. D. and Smith, P. F., *Review of mathematics, numerical factors, and corrections for dark matter experiments based on elastic nuclear recoil*, *Astropart. Phys.* **6** (1996) 87.

[71] Bernabei, R. *et al.*, *Search for WIMP annual modulation signature: Results from DAMA / NaI-3 and DAMA / NaI-4 and the global combined analysis.*, *Phys. Lett. B* **480** (2000) 23.

[72] **CDMS** Collaboration, Akerib, D. S. *et al.*, *First results from the cryogenic dark matter search in the Soudan Underground Lab*, *Phys. Rev. Lett.* **93** (2004) 211301, [astro-ph/0405033].

[73] **EDELWEISS** Collaboration, Chardin, G. *et al.*, *Latest results from the EDELWEISS WIMP search*, *Nucl. Instrum. Meth.* **A520** (2004) 101.

[74] Ahmed, B. *et al.*, *The NAIAD experiment for WIMP searches at Boulby mine and recent results*, *Astropart. Phys.* **19** (2003) 691, [hep-ex/0301039].

[75] Griest, K. and Kamionkowski, M., *Supersymmetric dark matter*, *Phys. Rept.* **333** (2000) 167.

[76] R.J. Gaitskell, *Noble Travails: Noble Liquid Dark Matter Detectors*, *Talk given at Aspen winter school* (2006).

[77] D. McKinsey, *Mini-CLEAN and DEAP/CLEAN Detectors*, *Talk given at University of Minnesota* (2007).

[78] **ArDM** Collaboration, Messina, M. and Rubbia, A., *Status report of ArDM project: A new direct detection experiment, based on liquid argon, for the search of dark matter*, *Prepared for 9th ICATPP Conference on Astroparticle, Particle, Space Physics, Detectors and Medical Physics Applications, Villa Erba, Como, Italy, 17-21 Oct 2005.*

[79] **WARP** Collaboration, Benetti, P. *et al.*, *Measurement of the specific activity of Ar-39 in natural argon*, *Nucl. Instrum. Meth.* **A574** (2007) 83, [astro-ph/0603131].

[80] Galbiati, C. and Purtschert, R., *Discovery of underground argon with low level of radioactive ^{39}Ar and possible applications to WIMP dark matter detectors*, astro-ph/0712.0381.

[81] **ICARUS** Collaboration, Arneodo, F. *et al.*, *The ICARUS experiment, a second-generation proton decay experiment and neutrino observatory at the Gran Sasso Laboratory*, *LNGS-EXP 13/89 add.2/01, ICARUS-TM/2001-09* (2001).

[82] Carmona, M. C., *Light simulations for the ArDM experiment*, *PhD. Thesis.*

[83] **MACRO** Collaboration, Ambrosio, M. *et al.*, *Limits on dark matter WIMPs using upward-going muons in the MACRO detector*, *Phys. Rev.* **D60** (1999) 082002, [hep-ex/9812020].

[84] **Super-Kamiokande** Collaboration, Desai, S. *et al.*, *Search for dark matter WIMPs using upward through-going muons in Super-Kamiokande*, *Phys. Rev.* **D70** (2004) 083523, [hep-ex/0404025].

[85] Bueno, A. *et al.*, *Observation of coherent neutrino-nucleus elastic scattering at a beta beam*, *Phys. Rev.* **D74** (2006) 033010.

[86] Bungau, C. *et al.*, *Monte Carlo studies of combined shielding and veto techniques for neutron background reduction in underground dark matter experiments based on liquid noble gas targets*, *Astropart. Phys.* **23** (2005) 97.

[87] Hennings-Yeomans, R. and Akerib, D. S., *A Neutron Multiplicity Meter for Deep Underground Muon- Induced High Energy Neutron Measurements*, *Nucl. Instrum. Meth.* **A574** (2007) 89, [astro-ph/0611371].

[88] Beacom, J. F. and Vagins, M. R., *GADZOOKS! Antineutrino spectroscopy with large water Cherenkov detectors*, *Phys. Rev. Lett.* **93** (2004) 171101, [hep-ph/0309300].

[89] Allison, J. *et al.*, *Geant4 developments and applications*, *IEEE Trans. Nucl. Sci.* **53** (2006) 270.

[90] Sauli, F., *GEM: A new concept for electron amplification in gas detectors*, *Nucl. Instrum. Meth.* **A386** (1997) 531.

[91] Jeanneret, P. *et al.*, *Performance of a new Micromegas detector, with woven wire mesh, in CF-4*, *Nucl. Instrum. Meth.* **A500** (2003) 133.

[92] Giomataris, Y. *et al.*, *MICROMEGAS: A high-granularity position-sensitive gaseous detector for high particle-flux environments*, *Nucl. Instrum. Meth.* **A376** (1996) 29.

[93] **Pierre Auger** Collaboration, Abraham, J. *et al.*, *Properties and performance of the prototype instrument for the Pierre Auger Observatory*, *Nucl. Instrum. Meth.* **A523** (2004) 50.

[94] Gichaba, J. O., *Measurement of Tyvek Reflectivity for the Pierre Auger Project*, *Master's Thesis* (1998).

[95] Hargrove, C. K. *et al.*, *Use of Gd in gas counters as neutron detectors in SNO*, *Nucl. Instrum. Meth.* **A357** (1995) 157.

[96] Monroe, J. and Fisher, P., *Neutrino Backgrounds to Dark Matter Searches*, *Phys. Rev.* **D76** (2007) 033007, [astro-ph/0706.3019].

[97] Lindhard, J. *et al. Mat. Fys. Medd. Dan. Vid. Selsk* **33** (1963) 10.

[98] Lippincott, W. H. *et al.*, *Scintillation time dependence and pulse shape discrimination in liquid argon*, nucl-ex/0801.1531.

[99] ILIAS database on radiopurity materials, "http://radiopurity.in2p3.fr/."

[100] Carson, M. J. *et al.*, *Neutron background in large-scale xenon detectors for dark matter searches*, *Astropart. Phys.* **21** (2004) 667, [hep-ex/0404042].

[101] Wilson, W. B. *et al.*, *SOURCES-4A*, *Technical Report LA-13639-MS, Los Alamos* (1999).

[102] Amare, J. *et al.*, *Neutrons from rock radioactivity in the new Canfranc underground laboratory*, *J. Phys. Conf. Ser.* **39** (2006) 151.

[103] Canfranc Underground Laboratory site, "http://ezpc00.unizar.es/lsc/index2.html."

[104] Mei, D. and Hime, A., *Muon-induced background study for underground laboratories*, *Phys. Rev.* **D73** (2006) 053004, [astro-ph/0512125].

[105] Wang, Y. F. *et al.*, *Predicting neutron production from cosmic-ray muons*, *Phys. Rev.* **D64** (2001) 013012, [hep-ex/0101049].

[106] Feldman, G. J. and Cousins, R. D., *A Unified approach to the classical statistical analysis of small signals*, *Phys. Rev.* **D57** (1998) 3873, [physics/9711021].

[107] **CDMS** Collaboration, Ahmed, Z. *et al.*, *A Search for WIMPs with the First Five-Tower Data from CDMS*, astro-ph/0802.3530.

[108] "http://pisrv0.pit.physik.uni-tuebingen.de/darkmatter/limits/index.php."

[109] Autiero, D. *et al.*, *Large underground, liquid based detectors for astro- particle physics in Europe: scientific case and prospects*, *JCAP* **0711** (2007) 011, [hep-ph/0705.0116].

[110] Pati, J. C. and Salam, A., *Unified Lepton-Hadron Symmetry and a Gauge Theory of the Basic Interactions*, *Phys. Rev.* **D8** (1973) 1240.

[111] Georgi, H. and Glashow, S. L., *Unity of All Elementary Particle Forces*, *Phys. Rev. Lett.* **32** (1974) 438.

[112] Dimopoulos, S. and Georgi, H., *Softly Broken Supersymmetry and SU(5)*, *Nucl. Phys.* **B193** (1981) 150.

[113] Sakai, N. and Yanagida, T., *Proton Decay in a Class of Supersymmetric Grand Unified Models*, *Nucl. Phys.* **B197** (1982) 533.

[114] Hisano, J. and Murayama, H. and Yanagida, T., *Nucleon decay in the minimal supersymmetric SU(5) grand unification*, *Nucl. Phys.* **B402** (1993) 46, [hep-ph/9207279].

[115] Nath, P. and Chamseddine, A. H. and Arnowitt, R., *Nucleon Decay in Supergravity Unified Theories*, *Phys. Rev.* **D32** (1985) 2348.

[116] Nath, P. and Arnowitt, R., *Grand unification and B and L conservation*, hep-ph/9808465.

[117] Shafi, Q. and Tavartkiladze, Z., *Flavor problem, proton decay and neutrino oscillations in SUSY models with anomalous U(1)*, *Phys. Lett.* **B473** (2000) 272, [hep-ph/9911264].

[118] Lucas, V. and Raby, S., *Nucleon decay in a realistic SO(10) SUSY GUT*, *Phys. Rev.* **D55** (1997) 6986, [hep-ph/9610293].

[119] Pati, J. C., *Probing grand unification through neutrino oscillations, leptogenesis, and proton decay*, *Int. J. Mod. Phys.* **A18** (2003) 4135, [hep-ph/0305221].

[120] Babu, K. S. and Pati, J. C. and Wilczek, F., *Suggested new modes in supersymmetric proton decay*, *Phys. Lett.* **B423** (1998) 337, [hep-ph/9712307].

[121] Babu, K. S. and Pati, J. C. and Wilczek, F., *Fermion masses, neutrino oscillations, and proton decay in the light of SuperKamiokande*, *Nucl. Phys.* **B566** (2000) 33, [hep-ph/9812538].

[122] Pati, J. C., *Discovery of proton decay: A must for theory, a challenge for experiment*, hep-ph/0005095.

[123] Ellis, J. R. and Nanopoulos, D. V. and Walker, J., *Flipping SU(5) out of trouble*, *Phys. Lett.* **B550** (2002) 99, [hep-ph/0205336].

[124] Arkani-Hamed *et al.*, *Aspects of split supersymmetry*, *Nucl. Phys.* **B709** (2005) 3, [hep-ph/0409232].

[125] Dorsner, I. and Fileviez Perez, P., *Unification without supersymmetry: Neutrino mass, proton decay and light leptoquarks*, *Nucl. Phys.* **B723** (2005) 53, [hep-ph/0504276].

[126] Hebecker, A. and March-Russell, J., *Proton decay signatures of orbifold GUTs*, *Phys. Lett.* **B539** (2002) 119, [hep-ph/0204037].

[127] Alciati, M. L. *et al.*, *Proton lifetime from SU(5) unification in extra dimensions*, *JHEP* **03** (2005) 054, [hep-ph/0501086].

[128] Klebanov, I. R. and Witten, E., *Proton decay in intersecting D-brane models*, *Nucl. Phys.* **B664** (2003) 3, [hep-th/0304079].

[129] Krishnaswamy, M. R. *et al.*, *Results from the KGF proton decay experiments*, *Nuovo Cim.* **C9** (1986) 167.

[130] **IMB** Collaboration, Matthews, J. *et al.*, *Recent results on nucleon decay from IMB*, *In LES ARCS 1987, Proceedings, New and Exotic Phenomena pag. 29.*

[131] Suzuki, A., *Solar neutrinos, atmospheric neutrinos and proton decays in Kamiokande*, *Talk at the ICEPP Symposium 'From LEP to the Plank World', University of Tokyo, 17 - 18 Dec, 1992.*

[132] Price, L. E., *The Soudan nucleon decay experiments*, *In Los Alamos 1982, Proceedings, Science Underground, pag. 161.*

[133] **Super-Kamiokande** Collaboration, Shiozawa, M. *et al.*, *Search for proton decay via* $p \to e^+ \pi^0$ *in a large water Cherenkov detector*, *Phys. Rev. Lett.* **81** (1998) 3319, [hep-ex/9806014].

[134] **Super-Kamiokande** Collaboration, Hayato, Y. *et al.*, *Search for proton decay through* $p \to \bar{\nu} K^+$ *in a large water Cherenkov detector*, *Phys. Rev. Lett.* **83** (1999) 1529, [hep-ex/9904020].

[135] **Super-Kamiokande** Collaboration, Kobayashi, K. *et al.*, *Search for nucleon decay via modes favored by supersymmetric grand unification models in Super- Kamiokande-I*, *Phys. Rev.* **D72** (2005) 052007, [hep-ex/0502026].

[136] Nath, P. and Fileviez Perez, P., *Proton stability in grand unified theories, in strings, and in branes*, *Phys. Rept.* **441** (2007) 191, [hep-ph/0601023].

[137] Amaldi, U., de Boer, W. and Furstenau, H., *Comparison of grand unified theories with electroweak and strong coupling constants measured at LEP*, *Phys. Lett.* **B260** (1991) 447.

[138] Rubbia, A., *Experiments for CP-violation: A giant liquid argon scintillation, Cerenkov and charge imaging experiment*, hep-ph/0402110.

[139] Baibussinov, B. *et al.*, *A new, very massive modular Liquid Argon Imaging Chamber to detect low energy off-axis neutrinos from the CNGS beam. (Project MODULAr)*, *Astropart. Phys.* **29** (2008) 174, [hep-ph/0704.1422].

[140] Fasso, A. *et al.*, *The physics models of FLUKA: Status and recent development*, hep-ph/0306267.

[141] Rubbia, A. *talk at the First International Workshop on Neutrino-Nucleus Interactions in the Few GeV Region (Nuint 01)* (December 2001, KEK, Tsukuba, Japan.).

[142] **NOMAD** Collaboration, Altegoer, J. *et al.*, *The NOMAD experiment at the CERN SPS*, *Nucl. Instrum. Meth.* **A404** (1998) 96.

[143] Bezrukov, L. B. and Bugaev, E. V., *Nucleon shadowing effects in photon nucleus interaction (in russian)*, *Yad. Fiz.* **33** (1981) 1195.

[144] Kudryavtsev, V. A. and Spooner, N. J. C. and McMillan, J. E., *Simulations of muon-induced neutron flux at large depths underground*, *Nucl. Instrum. Meth.* **A505** (2003) 688, [hep-ex/0303007].

[145] M. Crouch *In *Kyoto 1979, Proceedings, 20th International Cosmic Ray Conference, Vol. 6*, pag. 165.*

[146] **MACRO.** Collaboration, Ambrosio, M. *et al.*, *Vertical muon intensity measured with MACRO at the Gran Sasso Laboratory*, *Phys. Rev.* **D52** (1995) 3793.

[147] Ge, Y., Sala, P. and Rubbia, A., *e/π^0 separation in ICARUS LAr TPC*, *ICARUS-TM/03-05* (2003).

[148] Meregaglia, A. and Rubbia, A., *Neutrino oscillation physics at an upgraded CNGS with large next generation liquid argon TPC detectors*, *JHEP* **11** (2006) 032, [hep-ph/0609106].

[149] Wilkes, R. J., *UNO*, hep-ex/0507097.

[150] **Particle Data Group** Collaboration, Yao, W. M. *et al.*, *Review of particle physics*, *J. Phys.* **G33** (2006) 1.

[151] Kalman, R. E., *A new approach to linear filtering and prediction problems*, *Trans. ASME, J. Bas. Eng.* **82D** (1960) 35.

[152] Fruhwirth, R., *Application of Kalman filtering to track and vertex fitting*, *Nucl. Instrum. Meth.* **A262** (1987) 444.

[153] Wolin, E. J. and Ho, L. L., *Covariance matrices for track fitting with the Kalman filter*, *Nucl. Instrum. Meth.* **A329** (1993) 493.

[154] **ICARUS** Collaboration, Amoruso, S *et al.*, *Measurement of the mu decay spectrum with the ICARUS liquid Argon TPC*, *Eur. Phys. J.* **C33** (2004) 233, [hep-ex/0311040].

[155] **ICARUS** Collaboration, Amoruso, S. *et al.*, *Study of electron recombination in liquid argon with the ICARUS TPC*, *Nucl. Instrum. Meth.* **A523** (2004) 275.